Solar Wind-Magnetosphere-Ionosphere Coupling: Multiscale Study with Computational Models

Dong Lin

Dissertation submitted to the Faculty of the
Virginia Polytechnic Institute and State University
in partial fulfillment of the requirements for the degree of

Doctor of Philosophy
in
Electrical Engineering

Wayne A. Scales, Chair
C. Robert Clauer
J. Michael Ruohoniemi
Joseph B. H. Baker
Bhuvana Srinivasan
Yizheng Zhu

April 12, 2019
Blacksburg, Virginia

Keywords: SW-M-I coupling, Particle-in-cell model, Global MHD model, LTR model

Solar Wind-Magnetosphere-Ionosphere Coupling: Multiscale Study with Computational Models

Dong Lin

(ABSTRACT)

Solar wind-magnetosphere-ionosphere (SW-M-I) coupling is investigated with three different computational models that characterize space plasma dynamics on distinct spatial/temporal scales. These models are used to explore three important aspects of SW-M-I coupling. A particle-in-cell (PIC) model has been developed to explore the kinetic scale dynamics associated with the magnetotail dipolarization front (DF), which is generated as a result of magnetotail reconnection. The PIC study demonstrates that the electron-ion hybrid (EIH) instability could relax the velocity shear within the DF via emitting lower hybrid waves. The velocity inhomogeneity driven instability is highlighted as an important mechanism for energy conversion and wave emission during the solar wind-magnetosphere coupling, which has been long neglected before. The Lyon-Fedder-Mobbary (LFM) global magnetohydrodynamic (MHD) model is used to explore the fluid scale electrodynamic response of the magnetosphere-ionosphere to the interplanetary electric field (IEF). It is found that the cross polar cap potential (CPCP) varies linearly with very large IEF if the solar wind density is high enough. With controlled experiments of global MHD modeling driven by observed parameters, the linearity was interpreted as a result of the magnetosheath force balance theory. This study highlights the role of solar wind density in the electrodynamic SW-M-I coupling under extreme driving conditions. The LFM-TIEGCM-RCM (LTR) model, which is the Coupled-Magnetosphere-Ionosphere-Thermosphere (CMIT) model with Ring Current extension, is used to explore the integrated SW-M-I system. The LTR simulation study focuses on the subauroral polarization streams (SAPS), which involve both MHD and non-MHD processes and three-way coupling in the SW-M-I system. The global structure and dynamic evolution of SAPS are illustrated with state-of-the-art first-principle models for the first time. This study has successfully utilized multiscale models to characterize the forefront issues in the space plasma dynamics, which is required by the facts that plasmas have both particle and fluid featured properties and those properties are vastly different across geospace regions. It is highlighted that SW-M-I coupling could be significantly influenced by both microscopic and macroscopic processes. In order for a comprehensive understanding of the SW-M-I coupling, multiscale models and integrated framework of their combinations are critical.

Solar Wind-Magnetosphere-Ionosphere Coupling: Multiscale Study with Computational Models

Dong Lin

(GENERAL AUDIENCE ABSTRACT)

Three numerical models are used to explore the processes occurring in the Earth's space environment from an altitude of $\sim$ 100 km to 10s Earth radii (R_E). This environment is mainly filled with plasma, the gaseous state of charged particles that collectively behave like a fluid and are also subject to complex electromagnetic interactions. The intrinsic features of plasma determine that the physics on the scale of charged particles and that on the scale of fluids are both very important. On the other hand, considering the vast differences in the plasma properties throughout space, different regions need to be represented by different physically-based models. This dissertation study addresses the processes on three distinct spatial/temporal scales with different models. A particle model that treats plasma as a group of charged particles is used to explore wave generation in the magnetotail (10s R_E in the nightside). It is found that inhomogeneous plasma flow in the sharp boundary layer at the magnetotail (called "dipolarization front") can excite plasma waves to dissipate the energy originating from the solar wind (high speed plasma ejected from the sun). A magnetohydrodynamic (MHD) model that treats the plasma as a magnetized fluid is used to explore the efficiency of electric field mapping from the solar wind (10s R_E) to the ionosphere ($\sim$ 100 km altitude). The electric field in the ionosphere usually linearly increases with solar wind electric field until it is too strong. An observational event showed that their relationship remains linear for very large driving field. MHD modeling experiments demonstrate that the linearity at large driving field is due to the high solar wind density, which is explained with force balance theory. An integrated model framework is used to explore the system level response of geospace by investigating the enhanced plasma flow in the subauroral ionosphere (called the subauroral polarization streams, SAPS). The generation of SAPS involves driving and feedback processes in different regions (magnetosphere, ring current, ionosphere) that can not be simulated with any individual model. The global structures and dynamic evolution of SAPS have never been explored before with first-principle characterization of the effects from the solar wind to geospace. This integrated modeling represents a state-of-the-art model framework to explore processes in coupled geospace. These studies illustrate that different models are necessary to explore fundamental physics on small and large scales and the coupling processes between different space regions. It is also suggested that incorporating the different models into an integrated framework is necessary to get a comprehensive understanding of the dynamics in geospace.

Dedication

Dedicated to my family, especially Simai, my baby to be born.

Acknowledgments

I foremost would like to express my sincere gratitude to my advisor, Professor Wayne A. Scales, who has supported and guided me throughout my PhD study. Professor Scales has always been so helpful whenever I need his assistance no matter whether scientifically or technically. Professor Scales has also brought me to many different collaborators and plenty of travel opportunities to reach out by myself. I am especially grateful for those visits to the National Center for Atmospheric Research (NCAR), Naval Research Lab (NRL) and Johns Hopkins University Applied Physics Laboratory (JHU/APL) when he spared the whole week and days with me to focus on the research problems I was working on. Not to mention the interesting and thoughtful chats we had on the way, which has made him more like a senior friend than an advisor.

I also would like to thank my coauthors and their support beyond collaborations. I would like to thank Dr. Zhonghua Xu for his generous support for a few times during my study, which is far more than financially helpful. I also appreciate him for the opportunity to get involved in the data analysis for the ground magnetometer measurements. I would like to thank Dr. Michael Wiltberger, Dr. Binzheng Zhang, and Dr. Wenbin Wang of the High Altitude Observatory (HAO) for hosting my visits at NCAR and their mentorship. I would like to thank Dr. Misa Cowee and Dr. Dan Winske for hosting my visit at Los Alamos National Laboratory (LANL) and their mentorship. I would like to thank Professor C. Robert Clauer of Virginia Tech (VT) and Dr. Gurudas Ganguli of NRL for their insightful guidance during our collaborations and passionate reference supports during my postdoc application. I would like to thank Dr. Xiangrong Fu of the New Mexico Consortium, Dr. Yuxi Chen of the University of Michigan, Dr. Kevin Pham and Dr. Jing Liu of HAO, and

Dr. Viacheslav Merkin of JHU/APL for their patient assistance during my development and testing of the computational models that I have used in my PhD study. I also would like to thank all my coauthors, including the above mentioned and Dr. Chris Crabtree, Dr. Erik Tejero, and Dr. Alex Fletcher of NRL, Dr. Bharat Kunduri, and Mr. Maimaitirebike Maimaiti of VT for the constructive discussions and encouragements.

I would like to thank my colleagues at Space@VT. I would like to thank the Space Simulation Group, including Professor Bhuvana Srinivasan, Dr. Suleiman Baraka, Mr. Chirag Rathod, and Mr. Augustine Yellu, for their frank and open-minded suggestions during our discussions. I would like to thank Professor J. Michael Ruohoniemi and Professor Joseph B. H. Baker for their help since before I was officially admitted to the PhD Program of VT. I would like to thank our Center Administrator, Ms. Debbie Collins for her countless help with office affairs and family-like caring about me and my wife. I would like to thank Mr. John Harris for his always timely and exhaustive technical support for using the high performance computing resources. The ARC team of VT has also been a lot of help during my using the ARC platforms. I also would like to thank Dr. Michael Hartinger for hosting the office hours when we update research progress and exchange ideas, and for his sharing of academic and professional experience. My friends in the lab including Thomas Edwards, Shibaji Chakraborty, Yuxiang Peng, Shane Coyle, and Karthik Venkataramani have also given me a lot of inspirations.

I would like to thank all my family members for their accompanying, trusting, sharing, and listening, which is the solid foundation for all those I have experienced and achieved.

Contents

List of Figures

List of Tables

Chapter 1

Introduction

1.1 Fundamental Plasma Physics

1.1.1 Plasma Definition

The space environment of the Earth, i.e. geospace, is mostly filled by plasma. Plasma is defined as "a quasineutral gas of charged and neutral particles which exhibits collective behavior" [Chen, 1984]. It is also called the "fourth state of matter" beyond the commonly known states of solids, liquids, and gases. Plasma is formed at high temperatures when neutral atoms are ionized into freely moving ions and electrons. Almost all of the observable matter in the universe is in the plasma state. The collection of charged particles make plasma electrically conductive and able to respond to electromagnetic force in a collective manner. On the other hand, the gaseous status implies that plasma can flow like fluid due to the weak constraints between particles. It should be noted that plasma could also contain neutral components such as dust and grains. Basically, plasma is supposed to have properties featured by both charged particles and fluids.

1.1.2 Plasma Parameters

Plasma parameters can span a broad range of orders of magnitude throughout the solar-terrestrial space. Figure 1.1 shows the characteristic number densities and temperatures of different plasma contexts, which are generally more tenuous and hotter than solids, liquids, and gases. The auroral temperature is lower than the temperature in interstellar space, the solar wind, and nebula by 3-4 orders of magnitude. Both the number density and temperature of auroral plasma are smaller by several orders of magnitudes than the laboratory experimental plasma for magnetic and inertial confinement fusion.

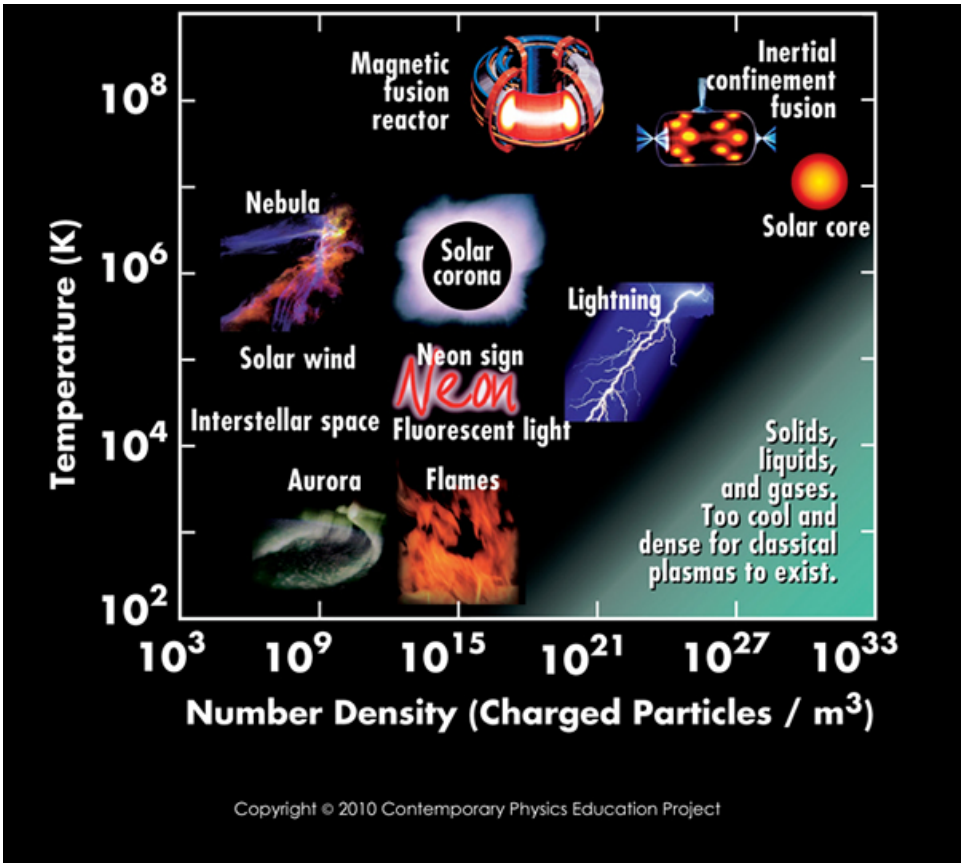

Figure 1.1: Characteristics of typical plasmas. Source: Contemporary Physics Education Project.

Besides the density and temperature, plasmas also have a lot more parameters that can

be used to describe their properties. Among those parameters, a few characteristic time, velocity, and length parameters are especially more commonly used. Plasma frequency ω_{ps} describes the time scales of plasma oscillation, which can be calculated with

$$\omega_{ps} = \sqrt{\frac{n_s q_s^2}{\epsilon_0 m_s}} \tag{1.1}$$

Here the subscript "s" means species, which could be "i" or "e" standing for ion and electron, respectively. n_s is the number density of the particle species, and $\epsilon_0 = 8.85 \times 10^{-12}$ F/m is the permittivity of free space. Here m_s is the mass of a charged particle and q_s is the amount of charges carried by that particle. The expression of ω_{ps} can be derived by solving the motion equation of charged particles due to the restoring force of charge separation. For a specific species of charged particles in a plasma, its oscillation frequency is uniquely determined by the number density. For a tenuous plasma with a number density of 5 cm^{-3}, which can be found in the solar wind and outer magnetosphere, the plasma frequency is $\sim$ 126 kHz for electrons and $\sim$ 3 kHz for ions. In the ionosphere where plasma density is $\sim 10^6$ cm^{-3}, the plasma frequency is typically higher by three orders of magnitude up to MHz.

Plasma gyrofrequency ω_{cs} describes the frequency of charged particle gyration around a magnetic field of magnitude B:

$$\omega_{cs} = \frac{q_s B}{m_s} \tag{1.2}$$

The gyrofrequency is determined by the magnetic field and charge-mass ratio. Due to the vast difference between ion and electron mass, the electron gyrofrequency is typically three orders of magnitude higher than the ion gyrofrequency. When considering a time scale that is much longer than the gyroperiod, a charged particle species can fulfill multiple gyro cycles, and can be regarded as "magnetized". For example in a magnetic field of 10 nT, which can be

found in the Earth's magnetosphere, the gyrofrequency is ~ 1.8 kHz for electrons and ~ 1 Hz for protons. On time scales above minutes, both ions and electrons in this environment can be regarded as magnetized. While on time scales below a millisecond, both species should be considered unmagnetized. Plasma species are generally more magnetized in a stronger magnetic field due to the higher gyrofrequency.

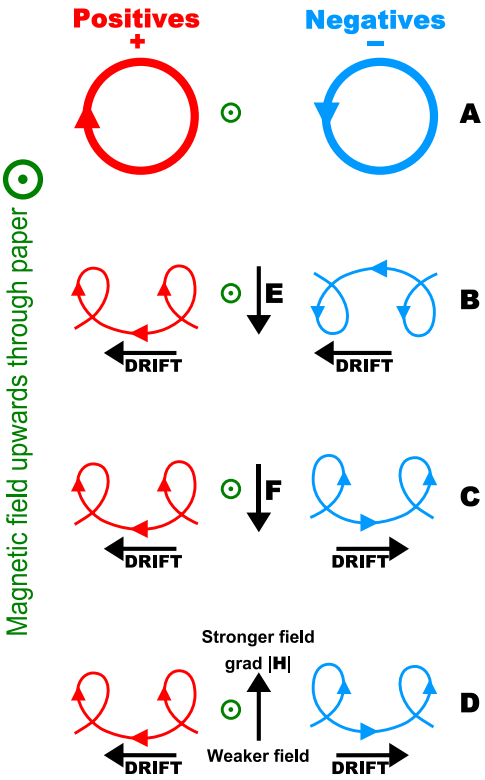

Figure 1.2: Gyro and drift motions of charged particles in a magnetic field. Source: Wikipedia page of "guiding center".

Thermal velocity is equivalent to the standard deviation of a Maxwellian velocity distribution, which is defined as:

$$V_{th,s} = \sqrt{\frac{k_B T_s}{m_s}} \tag{1.3}$$

Here $k_B = 1.38 \times 10^{-23}$ m^{2}kgs^{-2}K^{-1} is the Boltzmann constant and T_s is the temperature

of species s. Considering the vast range of plasma temperature as shown in Figure 1.1, the plasma thermal velocity can also be different by several orders of magnitude across the solar-terrestrial space.

Another characteristic velocity of plasma is the Alfvén velocity, which is calculated as:

$$V_{A,s} = \frac{B}{\sqrt{\mu_0 n_s m_s}} \tag{1.4}$$

Here $\mu_0 = 4\pi \times 10^{-7}$ H/m is the permeability constant of free space. The Alfvén velocity is the phase velocity of the Alfvén wave, which is a low-frequency (compared to the ion gyrofrequency) traveling oscillation of the ions and the magnetic field in a plasma. The ion mass density provides the inertia and the magnetic field line tension provides the restoring force. The proton Alfvén velocity with a density of 5 cm^{-3} in a magnetic field of 10 nT is $\sim$ 100 km/s.

The first row of Figure 1.2 illustrates the gyration of charged particles in a magnetic field. Note the directions of the gyrations of ions and electrons are opposite. The gyroradius describes the size of the loops that electrons and ions make around magnetic field lines, which is defined as the ratio between the transverse velocity to the magnetic field and gyrofrequency of charged particles:

$$\rho_s = \frac{V_{\perp,s}}{\omega_{cs}} \tag{1.5}$$

Thermal gyroradius is typically used to characterize the gyroradius of plasma species with temperature T_s: $\rho_s = \frac{\sqrt{k_B T_s / m_s}}{\omega_{cs}}$. The electron gyroradius is only a few centimeters in solar corona while it can be 1-20 km in the magnetosphere depending on the location. Ions with temperature of 4 keV in a magnetic field of 10 nT have a gyroradius of $\sim$ 1000 km. Hotter

and heavier species in a weaker magnetic field have a larger gyroradius.

Inertial length is defined as the ratio between light speed and species plasma frequency:

$$\lambda_s = \frac{c}{\omega_{ps}} \tag{1.6}$$

The electron inertial length is also called plasma skin depth, which is the depth in a plasma to which electromagnetic radiation can penetrate. The ion inertial length is the scale at which ions decouple from electrons and the magnetic field becomes frozen into the electron fluid rather than the bulk plasma. For plasmas with a density of 5 cm^{-3} and temperature of 10 keV, the ion and electron inertial lengths are λ_i=100 km and λ_e=2.4 km, respectively. The inertial length is determined by the plasma frequency. It is proportional to the square root of particle mass and inversely proportional to the square root of species density, which means heavier and more tenuous plasma have larger inertial lengths. Structures in the space environment are said to be kinetic when their scale length is comparable to the gyroradius or inertial length, e.g. the magnetotail dipolarization front.

There are also some dimensionless parameters characterizing plasma properties. The ratio between plasma frequency and gyrofrequency, $\frac{\omega_{ps}}{\omega_{cs}}$, describes the relative importance of plasma density and magnetic field. This ratio is usually very large for weakly magnetized or very dense species. It can be expressed as the ratio between light speed and the species Alfvén speed:

$$\begin{aligned} \frac{\omega_{ps}}{\omega_{cs}} &= \sqrt{\frac{n_s m_s}{\epsilon_0 B^2}} \\ &= \frac{c}{V_{A,s}} \end{aligned} \tag{1.7}$$

Plasma β is defined as the ratio between the thermal pressure and magnetic pressure. In

strong magnetic field plasmas such as the solar corona, plasma β is as low as 1%. High β up to 100 has been reported in laboratory experiments where the density is extremely large. Higher β implies that the plasma is more dominated by the thermal pressure than by the magnetic pressure. Plasma β can be also transformed into a form with thermal velocity and Alfvén velocity:

$$\begin{aligned}\beta &= \frac{n_s k_B T_s}{B^2/2\mu_0} \\ &= 2\frac{V_{th,s}^2}{V_{A,s}^2}\end{aligned} \tag{1.8}$$

Basically, these parameters can be used to describe specific aspects of plasma status and responses to the electromagnetic environment. The range of these parameters spans multiple orders of magnitude in different regions, which implies that the plasma properties are quite variable throughout the space plasma environment.

1.1.3 Plasma Descriptions

Since plasma consists of charged particles and behaves collectively, it is natural that plasma processes and phenomena exhibit both particle and fluid features. Therefore approaches based on particle dynamics and fluid dynamics have both been used to describe plasma systems.

Single Particle

From the perspective of single particles, particle motion in an electromagnetic field can be characterized by the Lorentz force based on Newton's second Law:

$$\frac{d\vec{V}}{dt} = \frac{q}{m}(\vec{E} + \vec{V} \times \vec{B}) \tag{1.9}$$

where $\vec{E}$ is the electric field, $\vec{B}$ is the magnetic field, and $\vec{V}$ the velocity of a charged particle. Typically, electric field tends to accelerate positively charged particles in the direction parallel to the electric field and negatively charged particles in the direction anti-parallel to the electric field. Magnetic field tends to make charged particles gyrate around the magnetic field lines if they have a nonzero velocity component in the transverse direction. Magnetic field does not directly affect charged particle motion in the field-aligned direction. When there is an additional force field $\vec{F}$ transverse to the magnetic field $\vec{B}$, the guiding center of the gyro motion gains a velocity in the direction transverse to both $\vec{F}$ and $\vec{B}$, which is called the plasma drift.

$$\vec{V}_d = \frac{\vec{F} \times \vec{B}}{qB^2} \tag{1.10}$$

Typical plasma drifts include the electric drift $\vec{V}_E$ (also called $\vec{E} \times \vec{B}$ drift) caused by the electric force, gravity drift $\vec{V}_g$ caused by the gravity $\vec{g}$, diamagnetic drift $\vec{V}_{DM}$ caused by pressure gradient force $-\nabla P$, and gradient drift $\vec{V}_{\nabla B}$ and curvature drift $\vec{V}_R$ due to nonuniform magnetic field. Figure 1.2 (B-D) shows the orbit of ion and electron drifts driven by these different forces.

$$\vec{V}_E = \frac{\vec{E} \times \vec{B}}{B^2} \tag{1.11}$$

$$\vec{V}_g = \frac{m\vec{g} \times \vec{B}}{qB^2} \tag{1.12}$$

$$\vec{V}_{DM} = \frac{-\nabla P \times \vec{B}}{nqB^2} \tag{1.13}$$

$$\vec{V}_{\nabla B} = \frac{mv_\perp^2}{2qB}\left(\frac{\vec{B} \times \nabla|\vec{B}|}{B^2}\right) \tag{1.14}$$

$$\vec{V}_R = \frac{mv_z^2}{qBR_C}\left(\frac{\vec{R}_C \times \vec{B}}{R_C B}\right) \tag{1.15}$$

It should be pointed out the drift velocity is derived from the gyro motion of charged particles.

It is assumed that the transverse force field is slow-varying on the scale of gyroradius so that the charged particles can undergo full gyro cycles. Also note that $\vec{V}_E$ is independent of the sign of charge and therefore does not cause a net current density when both ions and electrons undergo $\vec{E} \times \vec{B}$ drift. But the directions of all the others are dependent on the sign of charge, implying that gravity force, pressure gradient force, and magnetic gradient/curvature can all generate a net current density via plasma drift. The derivation of the curvature drift velocity ($\vec{V}_R$) is based on the assumption that the curvature radius R_C of the magnetic field is much larger than the gyroradius of charged particles.

While the motion of a single particle is determined by the electromagnetic field, the redistribution of all charged particles in a plasma could also alter the electromagnetic field. The variations of charge density $\rho_q = \sum_s n_s q_s$ and current density $\vec{J} = \sum n_s q_s \vec{V}_s$ change the source distribution of the electromagnetic field as shown in the Maxwell's Equations.

$$\nabla \times \vec{E} = -\frac{\partial \vec{B}}{\partial t} \tag{1.16}$$

$$\nabla \times \vec{B} = \mu_0 \vec{J} + \epsilon_0 \mu_0 \frac{\partial \vec{E}}{\partial t} \tag{1.17}$$

$$\nabla \cdot \vec{E} = \frac{\rho_q}{\epsilon_0} \tag{1.18}$$

$$\nabla \cdot \vec{B} = 0 \tag{1.19}$$

Magnetohydrodynamics

Plasma can be also described with the fluid approach when the length scale of interest is much longer than the ion skin depth and gyroradius, and the time scale is much longer than the ion gyro period. In the ideal situation, plasma fluid has negligible resistivity so that it can be treated as a perfect conductor. It is assumed that the plasma is strongly collisional, so that the time scale of collisions is shorter than the other characteristic times in the system,

and the particle distributions are close to Maxwellian.

Ideal Magnetohydrodynamic (MHD) equations consist of the mass continuity equation, momentum equation, energy equation, and variations of Maxwell's equations:

$$\frac{\partial \rho}{\partial t} + \nabla \cdot (\rho \vec{V}) = 0 \tag{1.20}$$

$$\rho(\frac{\partial \vec{V}}{\partial t} + \vec{V} \cdot \nabla \vec{V}) = -\nabla P + \vec{J} \times \vec{B} \tag{1.21}$$

$$\frac{d}{dt}(\frac{P}{\rho^{\gamma}}) = 0 \tag{1.22}$$

Here ρ is the mass density and P is the plasma pressure. The first two equations here are the continuity equation and momentum equation. The third equation is the adiabatic equation of state. The energy density can defined as $\epsilon = \frac{P}{\gamma - 1} + \frac{1}{2}\rho V^2 + \frac{B^2}{2\mu_0}$, which consists of the internal energy, kinetic energy, and magnetic field energy. Note $\gamma = 5/3$ is the ratio of specific heats for an adiabatic equation of state.

The electric field is derived from the Ohm's Law:

$$\vec{E} = -\vec{V} \times \vec{B} + \eta \vec{J} \tag{1.23}$$

where η is the resistivity. In ideal MHD, $\eta = 0$ and the electric field can be simplified as:

$$\vec{E} = -\vec{V} \times \vec{B} \tag{1.24}$$

The variation of electric field is assumed to be very slow in MHD thus the displacement current in Ampere's Law is neglected:

$$\vec{J} = \frac{1}{\mu_0} \nabla \times \vec{B} \tag{1.25}$$

When there are finite collisions in the plasma, the conductivity is no longer infinite and η is no longer 0. A dissipation term containing the resistivity appears in the induction equation:

$$\begin{aligned}\frac{\partial \vec{B}}{\partial t} &= -\nabla \times \vec{E} \\ &= \nabla \times (\vec{V} \times \vec{B}) + \frac{\eta}{\mu_0}\nabla^2 \vec{B}\end{aligned} \tag{1.26}$$

where we have used Equation (1.23) and (1.25).

The temporal partial differential equations in ideal MHD equation set can be transformed into the conservative form in terms of flow and flux parameters, which can be implemented in numerical models with those quantities conserved. The electric field equation (1.23, 1.24) and Ampere's Law (1.25) are not affected by the conservative form.

$$0 = \frac{\partial \rho}{\partial t} + \nabla \cdot (\rho \vec{V}) \tag{1.27}$$

$$0 = \frac{\partial (\rho \vec{V})}{\partial t} + \nabla \cdot (\rho \vec{V}\vec{V} + P_t \overleftrightarrow{I} - \frac{\vec{B}\vec{B}}{\mu_0}) \tag{1.28}$$

$$0 = \frac{\partial \epsilon}{\partial t} + \nabla \cdot [(\epsilon + P_t)\vec{V} - \vec{V} \cdot \frac{\vec{B}\vec{B}}{\mu_0}] \tag{1.29}$$

$$0 = \frac{\partial \vec{B}}{\partial t} + \nabla \cdot (\vec{V}\vec{B} - \vec{B}\vec{V}) \tag{1.30}$$

Here $P_t = P + \frac{B^2}{2\mu_0}$ is the total pressure consisting of plasma pressure and magnetic pressure.

Other Descriptions

The particle description and MHD description are two common examples of plasma descriptions. There have been approaches to characterize plasma dynamics that are intermediate between the particle and MHD scales, or combinations of the fundamental descriptions.

For example, considering the contrast in mass ratio between ions and electrons, the scales on which ions and electrons are magnetized are different by a few orders of magnitude. For

problems that focus on ion scale dynamics, electrons can be assumed to be fully magnetized. The electron gyro motion is not resolved but only the motion of electron guiding center is considered. This is the so-called gyro-kinetic method. On intermediate scales, electrons can be also treated as massless fluids, which is adopted in the hybrid description.

Plasma is essentially characterized by both microscopic and macroscopic parameters and processes. Both particle and fluid approaches have been successful in describing the kinetics and MHD dynamics of plasma, respectively, depending on the scale size in a specific plasma system. In the geospace plasma environment where the plasma parameters and characteristic scales are vastly different throughout, various plasma descriptions and their combinations are necessary in order to fully understand the behaviors and effects of space plasma.

1.2 Geospace Environments

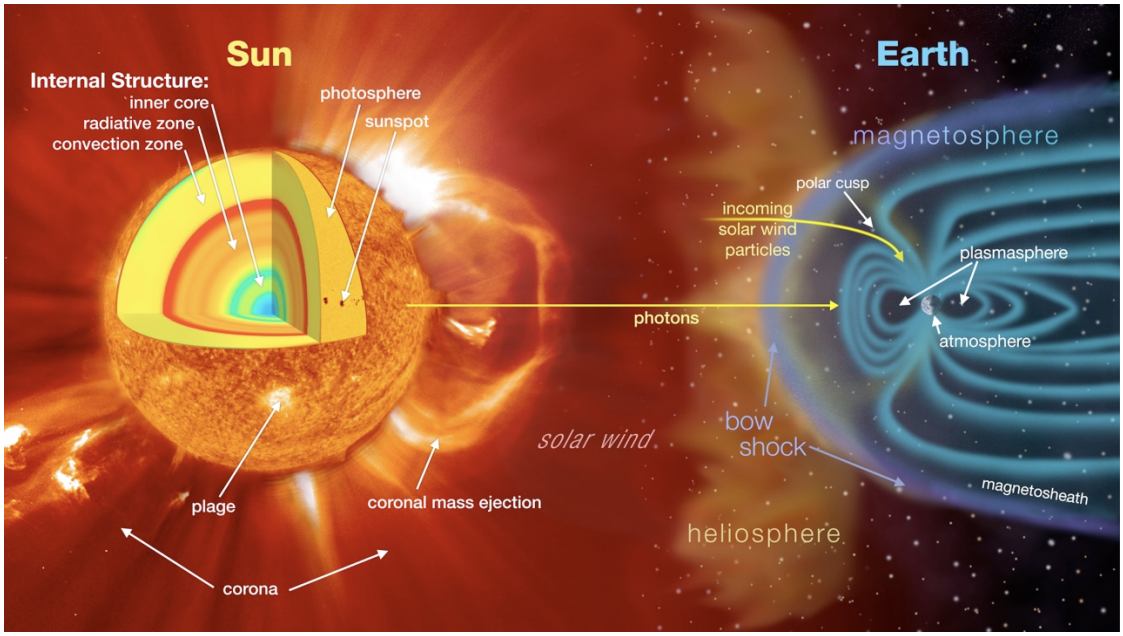

Figure 1.3: Overview of the solar-terrestrial space. Source: https://svs.gsfc.nasa.gov/30481

Geospace is constantly under the influence of our star, the Sun, which is about 1.5×10^8 km away (1 Astronomy Unit, AU). Although the radius of the Sun is only $\sim 7.0 \times 10^5$ km, 1/220 of 1 AU, the Sun can impact the Earth and other planets in the solar system via electromagnetic radiation, energetic particles, and continuously ejected solar wind plasmas. This entire space region influenced by the Sun is called the heliosphere.

Figure 1.3 shows an overview of solar-terrestrial space. Note this figure is not drawn to scale. While the electromagnetic radiation and energetic particles can directly penetrate to very low altitudes down to the ground, the solar wind interactions with Earth's environment occur at a much higher altitude, typically tens of Earth radii (R_E) due to the shielding effects of the Earth's magnetic field, the geomagnetic field. The effects occurring at the solar wind-magnetosphere interface can propagate along the geomagnetic field lines down to the bottom of geospace, and get coupled with the ionosphere-atmosphere. The solar wind-magnetosphere-ionosphere coupling determines the amount and efficiency of the transport of mass, momentum, and energy from the Sun into the geospace environment, which fundamentally affects space weather and human activity and assets.

1.2.1 Solar Wind

The solar wind is a stream of plasma released from the upper atmosphere of the Sun, namely the solar corona. The solar wind plasma mainly consists of protons and electrons, but also has a few percent of alpha particles and other heavier ions. Solar wind carries a magnetic field as it propagates in the heliosphere, which is called the interplanetary magnetic field (IMF) and can interact with the geomagnetic field. Two dominant mechanisms have been found for the enhancement of the solar wind: co-rotating interaction regions (CIRs) and coronal mass ejections (CMEs), which are more likely to occur at the solar activity minimum

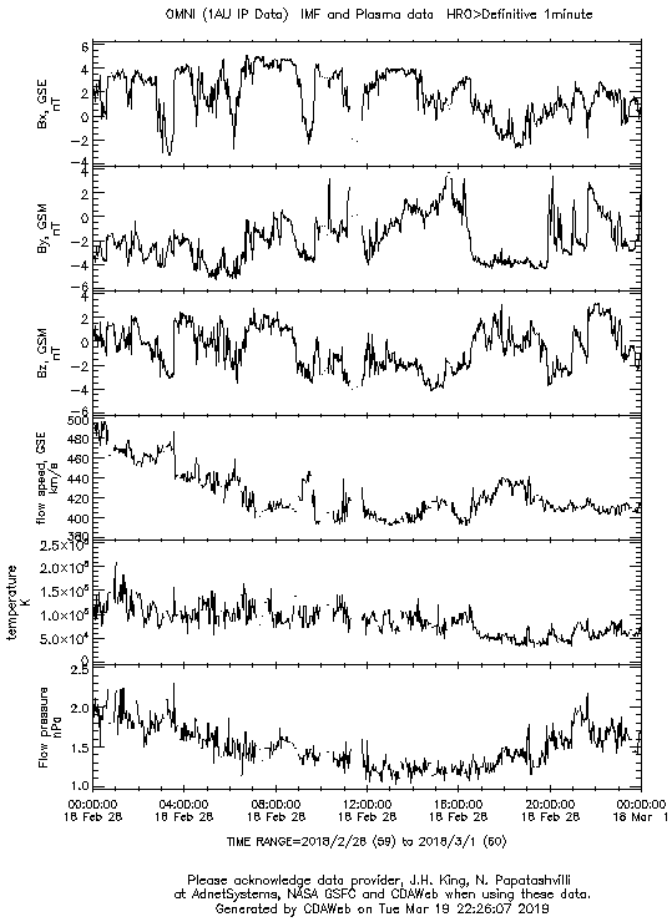

Figure 1.4: Solar wind and IMF conditions on February 28, 2018 obtained from the CDAWeb OMNI data set. From top to bottom: IMF B_X, B_Y, and B_Z in GSM coordinates, solar wind flow speed, temperature, and flow pressure.

and maximum, respectively. The solar wind velocity at 1 AU from the Sun right before it approaches the Earth is typically a few hundred km/s while the number density is a few to a few tens of particles per cubic centimeter (cm^{-3}). The IMF is typically a few to tens of nT while the electric field due to solar wind motion is typically a few mV/m. It is usually a good assumption to treat the solar wind plasma as ideal MHD on the large scale although kinetic scale structures and non-Maxwellian distributions are also observable.

Solar wind conditions can be monitored with satellites orbiting near the L_1 Lagrangian point, which lies at the gravitational balance location between the Sun and the Earth at a distance of

about 1.5×10^6 km from the Earth. For example the NASA Advanced Composition Explorer (ACE) is such a mission to make real-time measurements of the solar wind components and IMF, which provides important information about the input solar wind conditions driving the consequent space weather effects. The solar wind and IMF measurements can be obtained from the NASA CDAWeb OMNI data set. An example of the OMNI data set for February 28, 2018 is shown in Figure 1.4, including the three IMF components, solar wind flow speed, temperature, and flow pressure.

1.2.2 Magnetosphere

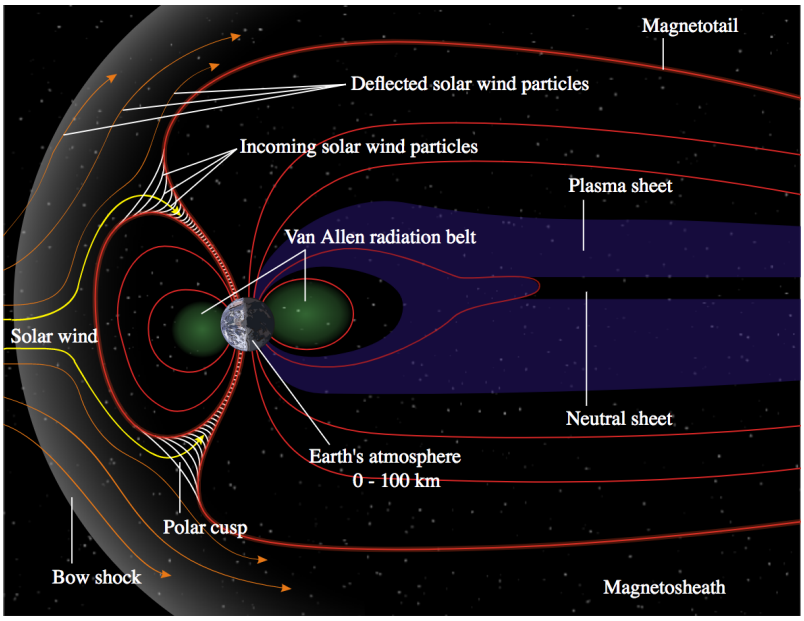

Figure 1.5: Diagram of Earth's magnetosphere. Source: NASA.

Figure 1.5 shows a diagram of the Earth's magnetosphere. Since the solar wind flow speed is usually larger than the sound speed of the solar wind plasma, a bow shock structure is formed in front of the magnetosphere when it is encountered by the supersonic plasma flow. The formation of the bow shock is representative of the large scale fluid dynamics during the interactions between the solar wind and the magnetosphere.

The geomagnetic field has a dipole configuration near the Earth. At the distance of several R_E from the Earth, it becomes compressed in the dayside and stretched in the nightside. Basically, the range with direct geomagnetic field influence is defined as the magnetosphere. The tear drop shaped cavity covers $\sim 10\ R_E$ on the dayside and up to a few hundred R_E on the nightside. The global scale structure of the magnetosphere can be investigated with the MHD description, which is a valid assumption for the plasma in the outer magnetosphere.

The outer boundary of the magnetosphere is called the magnetopause, which is formed as a result of pressure equilibrium between the solar wind dynamic pressure and the magnetic pressure of the Earth. The magnetopause thickness is typically around 800 km but generally broadens toward the nightside, varying between 100 km and 2000 km. The magnetopause has a scale size comparable to the ion gyroradius, implying that kinetic plasma physics may play an important role in the transport of the solar wind mass, momentum, and energy into the magnetosphere.

The space between the bow shock and the magnetopause is called the magnetosheath, where the solar wind flow has been decelerated to subsonic speeds. The magnetosheath plasma flow and magnetic field can directly couple to the magnetosphere.

The elongated magnetic field in the nightside is called the magnetotail. It contains two lobe regions where the plasma density is extremely low. The two lobes are separated by a plasma sheet where the magnetic field is weak but the plasma density is higher than in the lobes.

1.2.3 Ring Current

Although the solar wind and outer magnetospheric plasma can be well approximated as ideal MHD, it is no longer a good assumption when it comes closer to the Earth as the characteristic length and time scales are approaching the kinetic scale. Energetic ions and

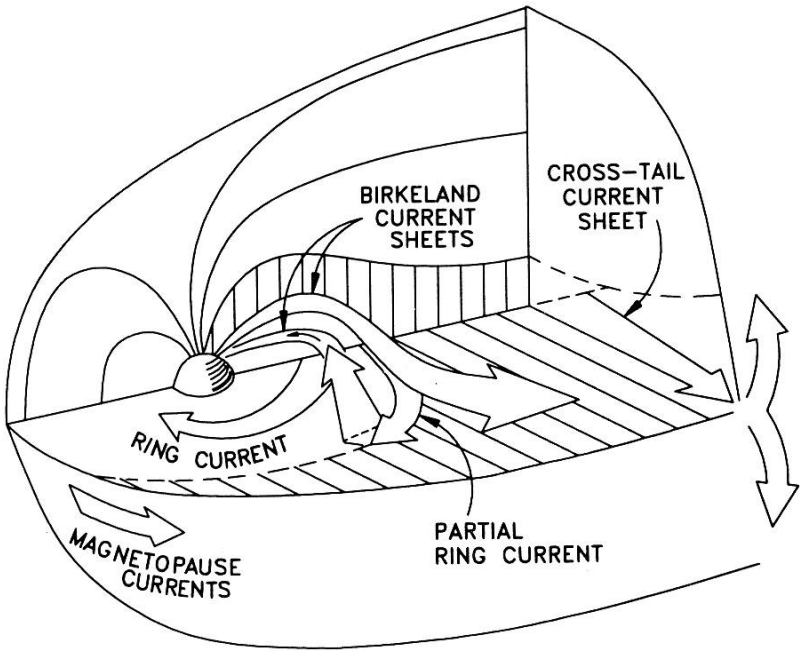

Figure 1.6: Schematic view of the different current systems which shape the Earth's magnetosphere. Source: Wikipedia "Ring current".

electrons are injected from the magnetotail into the inner magnetosphere where they are trapped to drift longitudinally. Since ions and electrons are drifting in opposite directions, a net current density is formed, namely the ring current. It should be pointed out that ring currents also exist in other planetary magnetospheres such as Jupiter.

The ring current is typically located at a distance of 3 to 8 R_E in the equatorial plane. A schematic view of the ring current and other current systems in the Earth's magnetosphere is shown in Figure 1.6. The main carriers of storm-time ring current are positive ions with energies from $\sim$ 1 keV to 100s keV and the carriers at quiet times are mainly protons. Electron contribute little to the ring current considering their negligible energy density. The most prominent effect of ring current enhancement is a decrease of northward component of the magnetic field on the ground, which is caused by the reduction of magnetic flux as the westward current density surrounding the Earth increases. The negative deflection of the northward magnetic field can be measured by the Disturbance Storm Time (Dst) index.

The motion of charged particles comprising the ring current is mainly energy-dependent gradient-curvature drift. The description of ring current particles requires specification of their energy and pitch angle, which is defined as the angle between the particle velocity and the magnetic field line [Daglis et al., 1999].

1.2.4 Radiation Belt

Another important plasma population in the magnetosphere are the radiation belts, which are also known as the Van Allen radiation belt. The radiation belt is a zone of energetic charged particles with energies of hundreds of keV to MeV. Most energetic particles have solar origins, including those locally accelerated after direct injection from the plasma sheet and solar energetic particles (SEP). The radiation belt population mainly consists of electrons and protons. There are two dominant belts known as the inner belt and outer belt, respectively. The inner belt is located at around 0.2 to 2 R_E from the Earth and the outer belt is at around 3 to 10 R_E. A schematic view of the cross section of the Earth's radiation belts is shown in Figure 1.7. Radiation belts have also been found in other planets such as the Jupiter.

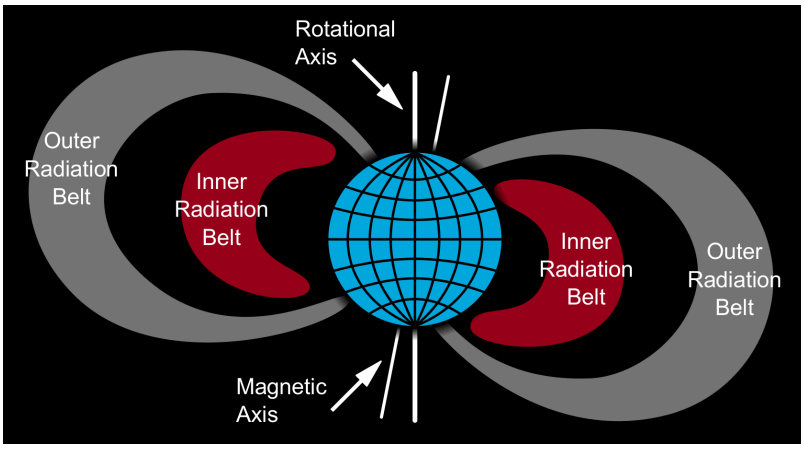

Figure 1.7: A cross section of the radiation belt. Source: Wikipedia page for "Van Allen Radiation Belt".

The radiation belts are essentially collisionless. The generation, loss, and transport of energetic particles in the radiation belts involve complicated interactions with magnetospheric plasma waves. The radiation belts have significant space weather effects. The relativistic electrons, namely the electrons with energies of MeV, can damage satellites by charging/discharging and penetration effects. The energetic particles can be lost to the atmosphere via wave-particle interactions, which change the conductance in the ionosphere and composition and dynamics in the atmosphere at lower altitudes.

1.2.5 Ionosphere

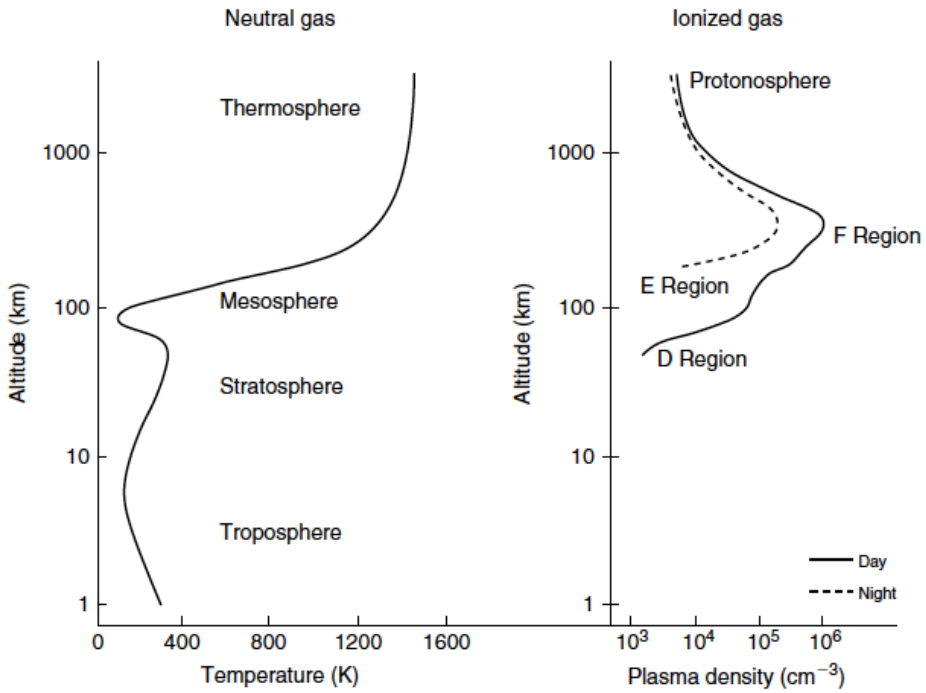

Figure 1.8: Typical altitude profiles of neutral atmospheric temperature and ionospheric plasma density. Source: Figure 1.1 of Kelley [2009].

The ionosphere is the ionized upper layers of the atmosphere which is typically at the altitude from 60 km to 1000 km. The ionosphere is formed primarily as a result of ionization of the neutral atmospheric molecules by solar radiation. Different radiations out of the solar

spectrum can penetrate into different heights in the atmosphere, ionize different species of the atmospheric molecules thus generate different ion species, and form the different ionospheric regions. The X-rays and cosmic ray particles can penetrate below 90 km and mainly generate NO^+ and O_2^{2+}, forming the D region. The long-wavelength Ultra-violet (UV) radiation and soft X-rays can ionize the atmosphere at 90-150 km where the major ion species are O_2^+ and NO^+, forming the E region. At the altitude of 130-500 km, the extreme UV (EUV) radiation is the dominant energy source that ionizes oxygen and form the F region, which is the top most layer of the ionosphere. The typical altitude profile of neutral atmospheric temperature and ionospheric plasma density is shown in Figure 1.8 Kelley [2009]. Since the solar radiation attenuates as it penetrates deeper into the atmosphere while the neutral density decreases as the altitude increases, the electron density has a peak structure in the F region where the energy source and neutral molecule source collectively optimize. Note the plasma density profile is also dependent on the local time and has diurnal, seasonal, annual, and solar cycle variations.

The ionosphere is a key element in the solar wind-magnetosphere-ionosphere coupling and plays important roles in space weather effects. Ionospheric electrodynamics have a strong dependence on the driving conditions arising from solar wind-magnetosphere interactions. The electrical potential, current, and conductance in the ionosphere have feedback effects to magnetospheric dynamics. Ionospheric convection and heating may greatly affect the thermospheric winds and processes in the middle and lower atmosphere. The ionosphere contains electrons, various ion species, and a number of neutral species. In order to characterize the dynamics in the ionosphere, it is necessary to solve the fluid equations for the neutral components, ionized species, and the Maxwell's electrodynamic equations.

1.3 Solar Wind-Magnetosphere-Ionosphere Coupling

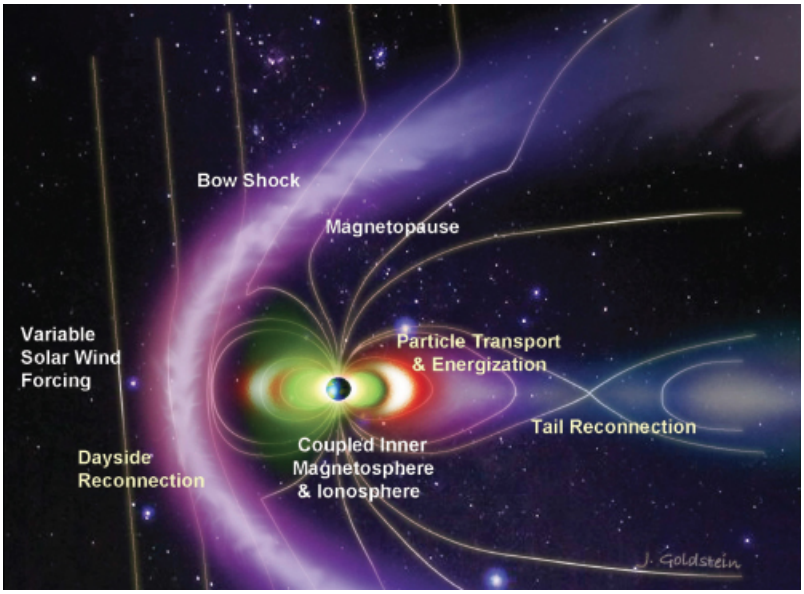

Figure 1.9: Illustration of the critical processes and structures during the solar wind-magnetosphere coupling. Source: Figure 9.9 of [National Research Council, 2013]. Courtesy of Jerry Goldstein, Southwest Research Institute.

Despite the distinct plasma properties in the different geospace environments, the solar wind, magnetosphere, and ionosphere are closely connected to each other. Figure 1.9 and Figure 1.10 show the critical processes and structures during the coupling between the solar wind, magnetosphere, and ionosphere. Basically, the solar wind-magnetosphere-ionosphere (SW-M-I) coupling consists of electromagnetic conversion, fluid dynamics, and particle energization and transport throughout the geospace environment.

1.3.1 Dungey Cycle

Among the solar wind-magnetosphere coupling mechanisms, the most significant process is generally considered to be the magnetic reconnection, which is the breaking and rejoining of magnetic field lines when anti-parallel magnetic fields approach each other [Dungey, 1961].

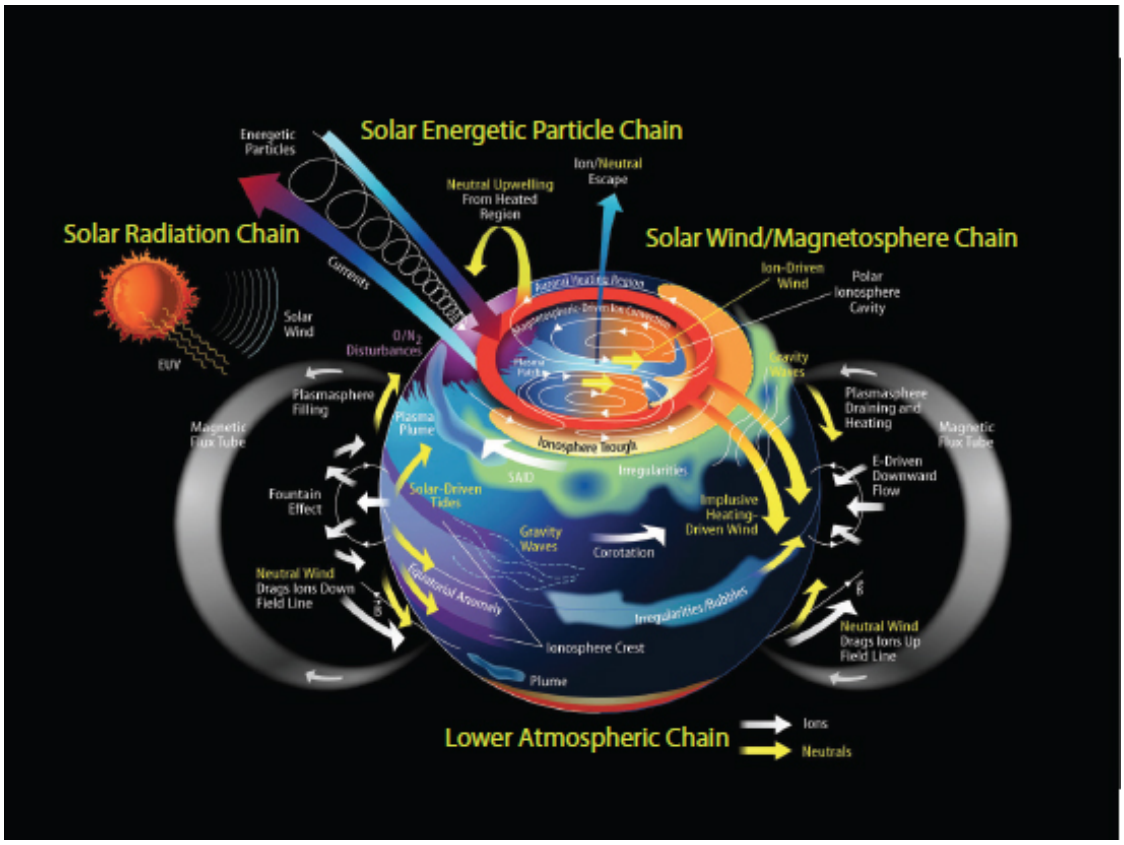

Figure 1.10: Illustration of the critical processes in the ionosphere-atmosphere and its connection to the magnetosphere. Source: Figure 8.1 of [National Research Council, 2013]. Courtesy of Joe Grebowsky, NASA Goddard Space Flight Center.

Significant magnetic flux transport and energization of plasma particles are associated with reconnection.

Specifically, when the IMF is southward, the anti-parallel IMF and geomagnetic field lines merge to form new field lines near the dayside subsolar magnetopause (Figure 1.11 top row). The newly formed open magnetic field lines are convected to the nightside as the solar wind passes by the Earth, resulting in the accumulation of magnetic flux in the region tailward of the Earth. The dipole-like geomagnetic field becomes elongated on the nightside where the magnetic field lines tend to be anti-parallel near the equatorial plane. Another magnetic reconnection occurs in the tail to revert the open magnetic flux back to be closed. Significant

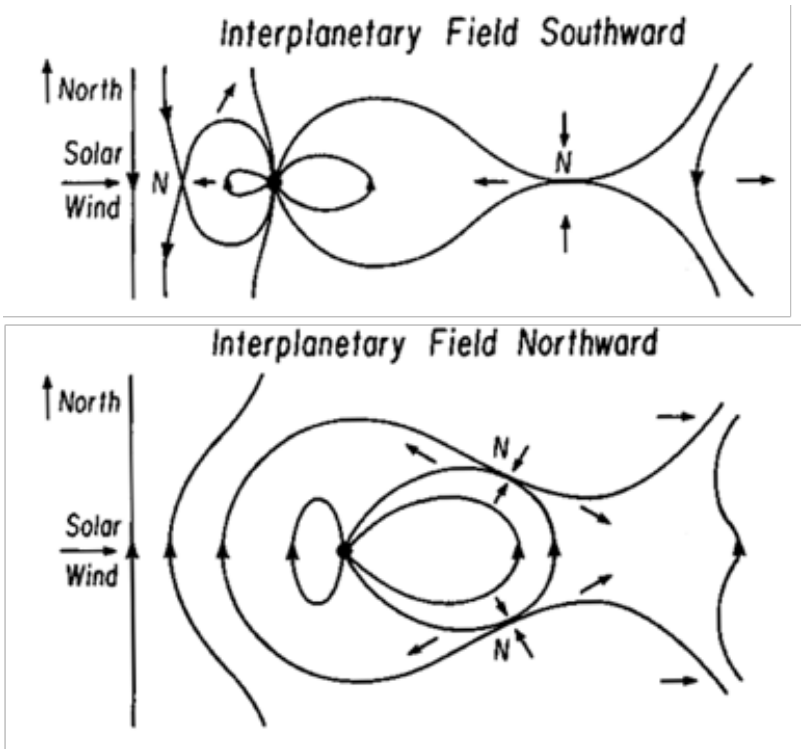

Figure 1.11: Illustration of the Dungey cycle [Dungey, 1961].

energy release is associated with the tail reconnection, which is generally believed to be the trigger of the geomagnetic storm/substorm activity that drives the auroral activity in the ionosphere.

When the IMF is northward, the IMF and geomagnetic field lines are parallel near the subsolar magnetopause. However, reconnection can still occur at a higher latitude where the geomagnetic field line is bending to be anti-parallel to the IMF, as shown in the bottom diagram of Figure 1.11.

In either case of IMF orientation, magnetic flux is exchanged between the solar wind and the magnetosphere, which is known as the "Dungey cycle" [Dungey, 1961]. Associated with the Dungey cycle is the convection of open magnetic field lines between the dayside and the nightside over the polar cap and at a lower latitude.

1.3.2 Ionospheric Convection

As the magnetospheric convection is driven by the Dungey cycle, the ionospheric footprints of the magnetic field lines also undergo a similar convection process. This is interpreted as the convection electric field in the magnetosphere mapped down to the ionosphere, which then drives the $\vec{E} \times \vec{B}$ drift of ionospheric plasma.

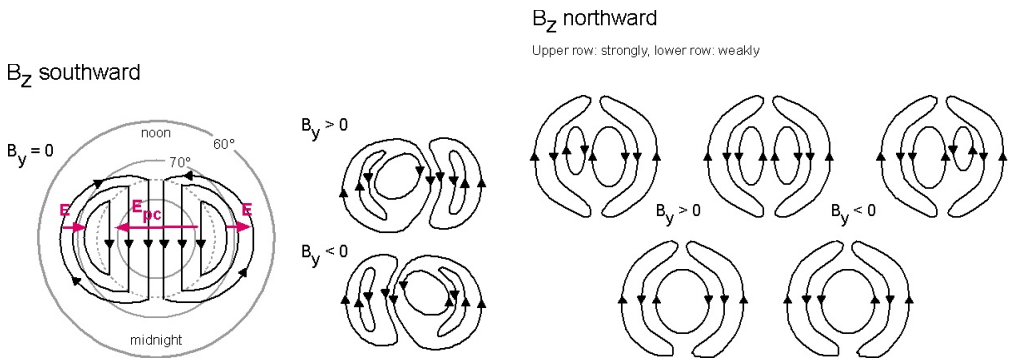

Figure 1.12: Ionospheric convection pattern under southward (left) and northward (right) IMF. Source: https://wiki.oulu.fi/display/SpaceWiki/Ionospheric+convection.

When the IMF is southward, the convection electric field is pointing from dawn to dusk and generates the twin cell convection pattern as shown in Figure 1.12 (left). The plasma is flowing from dayside to nightside over the polar region and returning from nightside to dayside at the lower latitude. The anti-sunward convection maps mainly to the magnetospheric tail lobes and the returning sunward flow in the auroral zone maps mainly to the plasma sheet and ring current regions [Cowley, 2000].

When the IMF is northward, the convection electric field is pointing from dusk to dawn and a four-cell convection pattern emerges. The two highest latitude convection cells have opposite rotation sense relative to the two convection cells under southward IMF. It is therefore called the reverse convection under northward IMF. The reverse convection pattern is shown in Figure 1.12 (upper right). The reverse convection cells at the high latitude are said to map to the reconnection at high latitude magnetopause [Crooker, 1992] while the two convection

cells at lower latitude are formed due to the viscous interaction. In both southward and northward IMF situations, the convection cells are twisted when there is a B_Y component.

1.3.3 Field-aligned Current

Ionospheric convection is subject to collisions between the plasma particles in the flow and the neutral particles in the atmosphere. The finite conductance implies that the convection electric field is accompanied by electric currents in the same direction of the electric field, which is known as the Pedersen current. As the altitude decreases, ion-neutral collision frequency increases to largely higher than the ion gyrofrequency so that ion drifts in the direction of $\vec{E} \times \vec{B}$ is negligible. Due to the difference in ion and electron mobility, electrons can drift at all ionospheric heights and therefore a net current in the direction transverse to the magnetic field and electric field also exists, which is known as the Hall current.

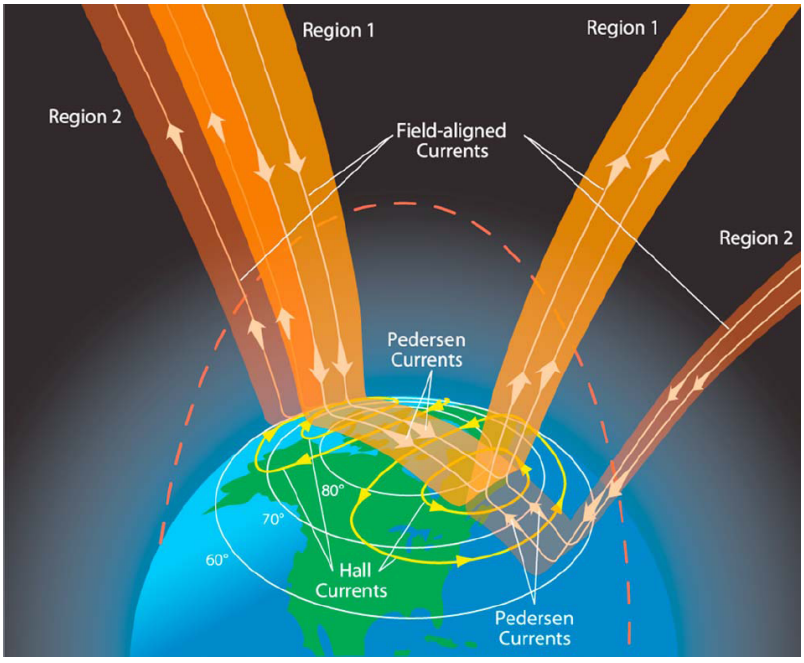

Figure 1.13: Ionospheric currents and magnetospheric field aligned currents. Source: Wikipedia page for Birkeland current.

As can seen in Figure 1.13, while the Hall currents can close in the ionosphere along the plasma streamlines ($\vec{E} \times \vec{B}$ drift path), the Pedersen currents flowing along the electric field direction cannot close within the ionosphere. Instead, the Pedersen currents are closed via currents that flow into and out of the ionosphere along the magnetic field line. These field aligned currents (FACs) can be detected by spacecraft via their magnetic signature and have been found to be a persistent feature between the magnetosphere-ionosphere.

Two major patterns have been recognized and known as Region 1 and Region 2, respectively. Region 1 FACs flow into the ionosphere from the dawn side and out from the dusk side, closing the Pedersen currents from dawn to dusk over the polar cap and those poleward currents across the auroral zone. Region 2 FACs have opposite direction and are at relatively lower latitudes than the Region 1 FACs. Region 2 FACs close the auroral zone currents. When the IMF is northward, there is a third current system caused by high latitude reconnection. They are at higher latitudes than the Region 1 FACs and known as Region 0 FACs. The FACs represent an important electrodynamic connections between the magnetosphere and ionosphere.

1.4 Computational Models

1.4.1 PIC Models

Particle-in-cell (PIC) models are widely used to investigate plasma dynamics on particle kinetic scale, such as kinetic instabilities, and magnetic reconnection. The PIC model solves the acceleration and movement equations of a large number of particles, and the Maxwell's equations for electromagnetic fields. The particles are tracked in the Lagrangian frame in continuous phase space, whereas the moments of their distribution such as charge densities

and current densities are evaluated in the Eulerian frame.

The typical method in a PIC model is using finite difference algorithm to update the differential equations of particle motion and Maxwell's equations. Depending on the scope of specific problems, PIC models can solve different sets of equations. For example, an electrostatic PIC model only deals with electrostatic variations and assumes static magnetically field. The electric field is computed from the electrostatic potential, which can be solved with the Poisson's equation and updated charge density distribution. An electromagnetic PIC model is able to resolve the magnetic perturbations.

PIC models can be one-dimensional (1D), two-dimensional (2D), or three-dimensional (3D). The choice of dimension depends on the characteristics of the physics to be investigated. A higher dimension PIC model is usually much more complicated and computationally more expensive than a lower dimension PIC model. More technical details about the PIC method can be found in Birdsall and Langdon [2004].

1.4.2 MHD Models

MHD models solve the MHD equation sets and are suitable for the study of fluid scale physics, such as MHD waves and instabilities, and global scale dynamics. Given the same computation capacity, MHD models can usually allow more sophisticated numerical algorithms than a PIC model considering the number of particles used in a PIC model. Indeed, advanced numerical algorithms have been developed to achieve much higher orders of accuracy than that in an explicit PIC model [e.g. **?**].

MHD models have been used for the simulation of planetary magnetospheres for decades, in which MHD equations are solved in a dipole geomagnetic field with an ionospheric conductance and FAC model providing inner boundary conditions [e.g. Wu et al., 1981]. Well-known

global MHD magnetosphere models include the Lyon-Fedder-Mobarry (LFM) [Lyon et al., 2004b], Block-Adaptive-Tree-Solarwind-Roe-Upwind-Scheme (BATS-R-US) [Powell et al., 1999], Open Geospace General Circulation Model (OpenGGCM) [Raeder et al., 1998], and Piecewise Parabolic Method with a Lagrangian Remap (PPMLR)-MHD [Hu et al., 2007] etc.

1.4.3 Integrated Framework

Various attempts have been made to combine the individual models for specific regions in the geospace environment to create an integrated modeling framework. This is on the one hand demanded by the fact that the different geospace regions are a highly coupled system and the forcing and feedback between geospatial regions are critical drivers of many important space weather effects. On the other hand, a single model can only describe certain components in the plasma environment (e.g., magnetosphere MHD, ring current particles, etc).

Integrated frameworks are combinations of different models in which specific information of plasma and/or electromagnetic field is exchanged between different models. For example in a magnetosphere-ring current model, the magnetic field obtained with a global MHD magnetosphere model is passed to the ring current to drive the transport of charged particles in that ring current model. After the ring current model reaches a new state, the plasma density and pressure at the inner magnetosphere covered by the ring current domain are passed back to the MHD model. Well-known integrated model frameworks include the Coupled Magnetosphere-Ionosphere-Thermosphere (CMIT) model [Wiltberger et al., 2004] and the Space Weather Modeling Framework (SWMF) [Tóth et al., 2005], etc.

1.5 Motivation

Solar wind-magnetosphere-ionosphere coupling has significant influences on the geospace environment and human life and facilities. The coupling processes determine how much energy and mass from the solar wind can be injected into the magnetosphere-ionosphere. How the gained energy and material is deposited in the geospace system affects various space weather phenomena. As human society is becoming increasingly dependent on the environment and assets in the space, it is getting more and more important to investigate the sources of space weather effects and develop forecasting capabilities.

While numerous space- and ground-based facilities have provided plenty of in-situ and remote measurements of the geospace environments, computational models have been an indispensable approach to achieve a comprehensive understanding of the complex physics and connections in the space plasma environments. Based on different assumptions of the plasma systems in each geospace region, computational models that focus on plasma dynamics on various spatial scales have been found very necessary.

Specifically, particle models that treat the plasma as a large number of charged particles have been used to the investigate the processes on the kinetic scale in a local regime. MHD models have been used to deal with the plasma properties on the fluid scale. Global models in which the geomagnetic field and atmosphere are represented have been successful in capturing many global structures and behaviors during solar wind-magnetosphere-ionosphere coupling events. Ongoing efforts are made to incorporate those models based on distinct physical foundations.

In this dissertation, three different models have been used to explore important aspects during SW-M-I coupling. These studies involve forefront issue related to the energy conversion and plasma dynamics in the coupled SW-M-I environments. The studies have highlighted

the role of flow inhomogeneity in wave emission at magnetotail dipolarization front and the role of solar wind density in the global ionospheric electrostatic potential response to very strong driving conditions, and illustrate the global structure and dynamic evolution of the sub-auroral ionospheric convection. These studies demonstrate the necessity of the respective plasma models. It is also emphasized that the coupling of different geospace models is critical for developing a comprehensive understanding of the highly coupled and dynamic geospace environment.

Chapter 2 introduces how the different computational models work. In Chapter 3, the energy conversion at the magnetotail is investigated with a particle-in-cell (PIC) model. In Chapter 4, the global electrodynamics is investigated with a global MHD model. In Chapter 5, an ionospheric phenomenon that involves both MHD, non-MHD, and wave-particle interactions is explored with an integrated model framework. The descriptions of each computational model and the detailed background of each problem are included in the respective chapters. The directions for future computational modeling are discussed in Chapter 5.

1.6 Attribution

Chapters 2, 3, and 4 are published/submitted studies that result from collaborations with my colleagues and collaborators. A brief description of their contributions is included here.

Wayne A. Scales, PhD (Electrical and Computer Engineering (ECE) Department, Virginia Tech) is a Professor of Electromagnetics at Virginia Tech. He was a co-author for Chapters 2, 3, and 4, and is the principle investigator for the NASA grants supporting these studies. Dr. Scales has supervised the entire dissertation study. He has provided guidance on choosing the topics and designing the research plans, instructed the development and tests of the models and interpretations of the simulation results with applicable plasma theories, and

contributed to the outline, composing, and polishing of the manuscripts.

Gurudas Ganguli, PhD (Plasma Physics Division, Naval Research Laboratory) is a Senior Scientist at Naval Research Lab. He was a co-author for Chapter 2. Dr. Ganguli has helped with designing the configuration and parameters of the particle model and applying the EIH theory to explain the simulation results, and contributed editorial comments.

Xiangrong Fu, PhD (New Mexico Consortium) is a Research Scientist at New Mexico Consortium. He was a co-author for Chapter 2. Dr. Fu has helped with the development of the particle model by providing comparison tests with his independent model. He has also contributed to the interpretation of the simulation results and editorial comments.

Chris Crabtree, PhD (Plasma Physics Division, Naval Research Laboratory) is a Research Physicist at Naval Research Lab. He was a co-author for Chapter 2. Dr. Crabtree has helped with interpreting the model configuration and simulation results, and contributed editorial comments.

Erik Tejero, PhD (Plasma Physics Division, Naval Research Laboratory) is a Research Physicist at Naval Research Lab. He was a co-author for Chapter 2. Dr. Tejero has helped with interpreting the EIH theory, and contributed editorial comments.

Yuxi Chen, PhD (Climate and Space Sciences and Engineering Department, University of Michigan) is a Research Fellow at University of Michigan. He was a co-author for Chapter 2. Dr. Chen has helped with interpreting the initial equilibrium and developing the code, and contributed editorial comments.

Alex C. Fletcher, PhD (Plasma Physics Division, Naval Research Laboratory) is a Post-doctoral Fellow at Naval Research Lab. He was a co-author for Chapter 2. Dr. Fletcher has helped with interpreting the wave properties.

Binzheng Zhang, PhD (High Altitude Observatory (HAO), National Center for Atmospheric Research (NCAR)) is a Project Scientist at the National Center for Atmospheric Research. He was a co-author for Chapters 3 and 4. Dr. Zhang has helped with using the LFM model for Chapter 3 and interpreting the simulation results for Chapters 3 and 4, and contributed editorial comments.

Michael Wiltberger, PhD (HAO, NCAR) is a Research Scientist at NCAR. He was a co-author for Chapters 3 and hosted my visit of HAO during which the Chapter 3 study was partly supported. Dr. Wiltberger has helped with interpreting the simulation results and contributed editorial comments.

C. Robert Clauer, PhD (ECE Department, Virginia Tech) is a Professor of Space Science at Virginia Tech. He was a co-author for Chapters 3. Dr. Clauer has helped with interpreting the observational event and contributed editorial comments.

Zhonghua Xu, PhD (ECE Department, Virginia Tech) is a Research Scientist at Virginia Tech. He was a co-author for Chapters 3. Dr. Xu has helped with interpreting the observational event and contributed editorial comments.

Wenbin Wang, PhD (HAO, NCAR) is a Project Scientist at NCAR. He was a co-author for Chapters 4 and hosted my visit of HAO during which the Chapter 4 study was partly supported. Dr. Wang has helped with testing and using the LTR model, interpreting the simulation results, and contributed editorial comments.

Kevin Pham, PhD (HAO, NCAR) is a Postdoctoral Fellow at NCAR. He was a co-author for Chapters 4. Dr. Pham has helped with testing and using the LTR model, interpreting the simulation results, and contributed editorial comments.

Jing Liu, PhD (HAO, NCAR) is a Project Scientist at NCAR. He was a co-author for Chapters 4. Dr. Liu has helped with testing and using the LTR model especially the TIEGCM

component, interpreting the simulation results, and contributed editorial comments.

Viacheslav Merkin, PhD (Applied Physics Laboratory, Johns Hopkins University) is a Space Physicist at the Johns Hopkins University. He was a co-author for Chapters 4. Dr. Merkin has helped with testing and using the LTR model especially the LFM component, interpreting the simulation results, and contributed editorial comments.

Xueling Shi, PhD candidate (ECE Department, Virginia Tech) is a PhD student at Virginia Tech. She was a co-author for Chapters 4. Ms. Shi has helped with plotting the figures, interpreting the data/model comparison, and contributed editorial comments.

Bharat Kunduri, PhD (ECE Department, Virginia Tech) is a Postdoctoral Fellow at Virginia Tech. He was a co-author for Chapters 4. Dr. Kunduri has helped with understanding of the SAPS phenomenon and accessing observational data for comparison with the simulation results.

Maimaitirebike Maimaiti, PhD candidate (ECE Department, Virginia Tech) is a PhD student at Virginia Tech. He was a co-author for Chapters 4. Mr. Maimaiti has helped with understanding of the SAPS phenomenon, and contributed editorial comments.

Chapter 2

Particle-in-cell Modeling of Magnetotail Dipolarization Front

Dong Lin[1], Wayne A. Scales[1], Gurudas Ganguli[2], Xiangrong Fu[3], Chris Crabtree[2], Erik Tejero[2], Yuxi Chen[4], and Alex Fletcher[2] (2019), A New Perspective for Dipolarization Front Dynamics: Effects of Velocity Inhomogeneity, *manuscript submitted to Journal of Geophysical Research: Space Physics*.

[1] Bradley Department of Electrical and Computer Engineering, Virginia Tech, Blacksburg, Virginia, USA

[2] Naval Research Lab, Washington DC, USA

[3] New Mexico Consortium, Los Alamos, NM, USA

[4] Center for Space Environment Modeling, University of Michigan, Ann Arbor, MI, USA

Abstract The stability of a quasi-static near-Earth dipolarization front (DF) is investigated with a two-dimensional electromagnetic particle-in-cell (EMPIC) model. Strongly localized ambipolar electric fields self-consistently generates a highly sheared dawnward $\vec{E}\times\vec{B}$ electron drift on the kinetic scale in the DF. EMPIC simulations based on the observed DF thickness and gradients of plasma/magnetic field parameters reveal that the DF is susceptible to the kinetic electron-ion hybrid (EIH) instability driven by the strong velocity inhomogeneity. The excited waves show a broadband spectrum in the lower hybrid (LH) frequency range,

which has been often observed at DFs. The wavelength is comparable to the shear scale length and the growth rate is also in the LH frequency range, which are consistent with the EIH theory. As a result of the LH wave emissions, The velocity shear is relaxed and the DF is broadened. When the plasma beta increases, the wave mode shifts to longer wavelengths with reduced growth rates and enhanced magnetic fluctuations although the wave power is mostly in the electrostatic regime. This study highlights the role of velocity inhomogeneity in the dynamics of DF which has been long neglected. The EIH instability is suggested to be an important mechanism for the wave emissions and stability at the DF.

2.1 Introduction: Magnetotail Dipolarization Front

Dipolarization fronts (DFs) are Earthward propagating boundary layer structures that are frequently observed in the Earth's magnetotail. The most prominent feature of DFs is a sharp increase of magnetic field northward component over a scale length comparable to or less than the ion thermal gyroradius [Runov et al., 2009, 2011]. DFs are generally believed to be generated by magnetotail reconnection. When the hot and tenuous reconnection jet encounters the denser and colder ambient magnetotail plasma, the kinetic scale boundary layer is formed [e.g., Lu et al., 2015, Sitnov et al., 2009]. The inhomogeneities of plasma and magnetic field parameters at DFs are expected to excite a number of wave modes. Waves with a broad frequency range are observed to coincide with the DF, with frequencies extending from below the lower hybrid (LH) frequency to above the electron cyclotron frequency [e.g., Zhou et al., 2009].

The strong Earthward density gradient at DFs has been shown to drive a hierarchy of instabilities on different scales. Runov et al. [2011] revealed that the plasma density typically decreases by $\sim 50\%$ at the tailward side of DF. Lapenta and Bettarini [2011] found with 3D

magnetohydrodynamic (MHD) simulations that the density gradient at the DFs can lead to an interchange instability, the scale of which is selected by the kinking flux ropes upstream. Pritchett and Coroniti [2010] found with 3D electromagnetic particle-in-cell (EMPIC) simulations that the dipolarized plasma sheet configuration is unstable to a ballooning/interchange type mode, which has a wavelength on the order of the ion gyroradius. This mode can be interpreted as the low-frequency extension of the lower hybrid drift instability (LHDI). The evolution of LHDI at DF has also been investigated by Divin et al. [2015a,b]. It was found that the density gradient driven LHDI generates wave modes on the electron gyroradius scale with frequencies in the LH range [Krall and Liewer, 1971].

Anisotropic velocity distributions are another energy source of unstable modes at magnetotail DFs. Fu et al. [2012a] examined the pitch angle distribution of suprathermal electrons in the flux pileup regions (FPRs) located behind the DFs. They found perpendicular ($T_{\perp,e}/T_{\parallel,e} > 1$) and parallel ($T_{\perp,e}/T_{\parallel,e} < 1$) distributions inside the growing and decaying FPRs, respectively. These distributions are suggested to result from betatron acceleration due to the magnetic field compression and Fermi acceleration due to the shrinkage of a flux tube [Fu et al., 2011, Huang et al., 2015, Lu et al., 2016a], and could drive the temperature anisotropy whistler instability and oblique electron firehose instability, respectively [Zhang et al., 2018].

While the density gradient and anisotropy driven instabilities have been investigated in a number of studies, the effects of flow inhomogeneity within the DF have been long neglected. The strong gradient of magnetic field B_Z at DFs implies the existence of a current density in the dusk direction, which has been verified by satellite observations [e.g. Fu et al., 2012b]. The current density was shown to be mainly carried by the dawnward drifting electron flow, which consists of both diamagnetic drift due to electron pressure gradient, and the $\vec{E}\times\vec{B}$ drift due to the Earthward electric field. Note here the ions are effectively unmagnetized in the DF thus can not undergo the drift motion entirely [Ganguli et al., 2018]. The transverse electric

field is essentially an Earthward ambipolar electric field due to the global compression effects that accelerate the DFs toward the Earth, which is localized in the DF. Further quantitative analysis reveal that the $\vec{E} \times \vec{B}$ drift is dominant over the diamagnetic drift, and ion flow is relatively negligible [Fletcher et al., 2019, Fu et al., 2012b]. Considering the kinetic scale thickness, the electron flows within the DFs are shown to have a substantial velocity shear, the electromagnetic effects of which on the DF stability, however, have not been well explored before [Fletcher et al., 2019, Ganguli et al., 2018].

Velocity shear driven instabilities are ubiquitous in space plasma environments on different scales. Depending on the shear scale length L_E relative to the ion gyroradius ρ_i, the consequent wave modes have different wave frequencies and wavelengths that are commensurate with the velocity shear [Ganguli et al., 1994a,b]. The classical Kelvin-Helmholtz instability (KHI) is in the fluid regime $L_E \gg \rho_i$, which can be observed on e.g., the Earth's magnetopause [Hasegawa et al., 2004]. The wave frequency is much less than the ion gyro frequency Ω_{ci}, and the wavelength is much longer than ρ_i [Lin et al., 2014]. Kinetic theories have been developed to characterize the unstable wave modes when L_E is comparable to or smaller than ρ_i. Specifically, the electron-ion hybrid (EIH) instability is driven by the transverse velocity shear with intermediate scale length ($\rho_e < L_E < \rho_i$), when ions are effectively unmagnetized and electrons have shear corrected velocity distributions [e.g., Ganguli et al., 1988a,b, Romero et al., 1992]. The kinetic EIH modes have been verified in a number of space and laboratory experiments and numerical simulations [e.g., Amatucci et al., 1996, DuBois et al., 2014, Liu et al., 2014, 2017, Romero and Ganguli, 1993, Scales et al., 1994a,b], and are suggested to be important mechanisms for the generation of broadband electrostatic fluctuations. However, previous EIH studies have been mostly focused on the electrostatic emissions and assumed uniform magnetic field for simplicity [e.g., Romero and Ganguli, 1993, Romero et al., 1992]. EIH modes in a more realistic configuration of a DF with magnetic

gradient and their nonlinear electromagnetic properties have not been well understood.

Recently, Ganguli et al. [2018] showed with high-resolution Magnetospheric Multi-Scale (MMS) measurements that the ambipolar potential across the DF results in strongly sheared electron flows with sub-ion scale. Liu et al. [2018a] reported MMS observation of an electron jet inside a DF that has a shear frequency larger than the lower hybrid frequency. Fletcher et al. [2019] investigated two DF events observed by the MMS satellite and developed a rigorous kinetic equilibrium. It still remains unclear how the highly sheared tangential flow may contribute to the distinctive broadband emissions at DFs. In this study, we evaluate the role of the velocity shear at DFs by investigating the excitation of the electromagnetic EIH instability [Ganguli et al., 2014] at a kinetic scale boundary layer with sharp gradients of magnetic and plasma parameters. Electromagnetic particle-in-cell simulations are conducted to explore the DF stability and consequent spectral characteristics.

2.2 Model Configuration

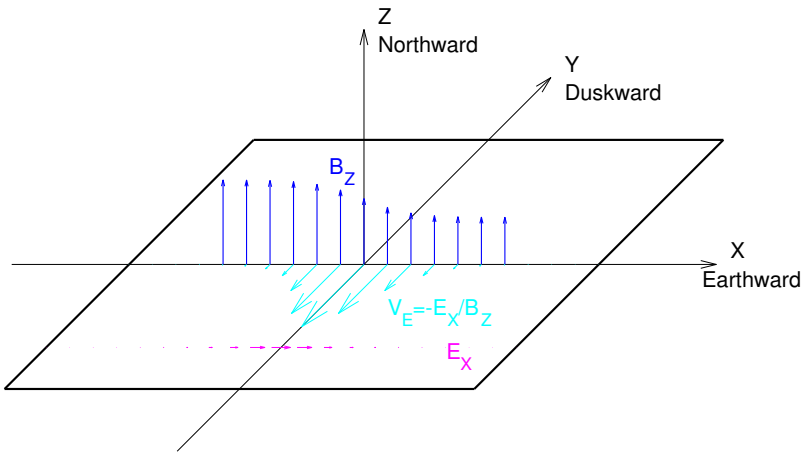

Figure 2.1: Transverse sheared electron flow in the equatorial plane of a DF. The blue arrows show the northward magnetic field B_Z with a tailward gradient. The magenta arrows show the Earthward ambipolar electric field. The cyan arrows show the dawnward drift velocity of electrons.

Figure 2.1 shows the configuration of transverse sheared flows in a magnetotail DF structure. The magnetic field at the DF is characterized by enhanced northward component B_Z with a tailward gradient. An Earthward ambipolar electric field E_X is localized within the front due to the compression of magnetotail reconnection outflow, which drives $\vec{E} \times \vec{B}$ drift flow toward dawn. The gradient scale length of the DF is chosen to be intermediate between the ion and electron gyroradius so that ions are effectively unmagnetized within the DF while electrons are magnetized. The dawnward $\vec{E} \times \vec{B}$ drift and diamagnetic drift of electrons result in a net current density toward the duskside.

In this study, we adopt a simplified two-dimensional force-balanced model by assuming the ambipolar electric field is localized near the DF and the density profile has a smooth transition of hyperbolic tangent form. The magnetic field profile can be then determined from Ampere's Law. Here we note that this simplified model may be derived as an expansion of the fully kinetic model [Fletcher et al., 2019, Ganguli et al., 2018].

$$E_X(x) = E_m \mathrm{sech}^2 \tfrac{x}{L_E} \tag{2.1}$$

$$N(x) = N_0[1 + \tfrac{\Delta N}{2}(\tanh \tfrac{x}{L_E} - 1)] \tag{2.2}$$

$$\nabla \times \vec{B} = \mu_0 N_e q_e (\vec{V}_{dim} + \vec{V}_{\vec{E}\times\vec{B}}) \tag{2.3}$$

$$B_Z(x) = B_0 \sqrt{1 + \beta_0 (1 - \tfrac{N(x)}{N_0}) + \tfrac{N_0}{\Delta N} \tfrac{e E_m L_E}{B_0^2/2\mu_0} [1 - (\tfrac{N(x)}{N_0})^2]} \tag{2.4}$$

Figure 2.2 shows the initial profiles of the plasma parameters and electromagnetic field components in the DF model. The X axis is pointing toward the Earth. The values are derived from the observed event in Ganguli et al. [2018] but have been adapted to accommodate the simulation capacity. Figure 2.2(a) and (e) show the plasma density $N(x)$ and magnetic field B_Z, which both use the values on the Earthward side as units (N_0 and B_0). The plasma density has an Earthward gradient and drops by $\Delta N = 25\%$ tailward of the DF. B_Z in-

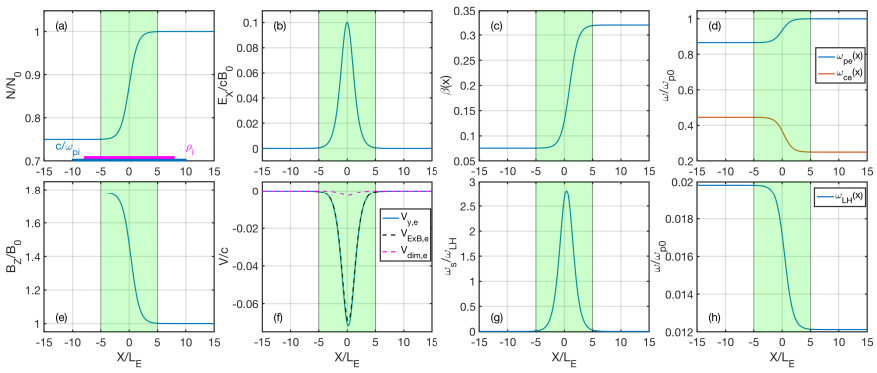

Figure 2.2: Initial profiles of (a) plasma density, (b) electric field E_X, (c) plasma β, (d) electron plasma frequency ω_{pe} (blue) and electron cyclotron frequency ω_{ce} (orange), (e) magnetic field B_Z, (f) electron total drift velocity (blue), $\vec{E} \times \vec{B}$ drift (black dash), and diamagnetic drift (magenta), (g) ratio between shear frequency ω_s and the lower hybrid frequency ω_{LH}, (h) lower hybrid frequency ω_{LH}. The green shaded regions show the DF thickness represented by the transitions of electromagnetic/plasma parameters.

creases to about 1.8 B_0 in the tailward direction as a result of force balance. Note in the observation, the tailward B_Z is about 1.9 B_0 (from $\sim$ 7 nT to $\sim$ 13 nT). This can be seen as the magnetic field generated by the $\vec{E} \times \vec{B}$ drifting electrons and ions not drifting to the small scale electric field. Figure 2.2 (b) and (f) show the ambipolar electric field $E_X(x)$ and the electron dawnward drift velocities. The E_X has a peak value of $E_m = 0.1cB_0$, where c is the light speed. The electron velocity is dominated by the $\vec{E} \times \vec{B}$ drift ($\vec{V}_{\vec{E}\times\vec{B}}$), with peak magnitude $0.069c$, compared to a peak magnitude of 0.003 c for the diamagnetic drift ($\vec{V}_{dim}$). Figure 2.2 (c) shows the electron plasma $\beta_e = \frac{NkT_0}{B_Z^2/2\mu_0}$ varies from 0.08 in the tailward to $\beta_0 = 0.32$ in the Earthward regions. Note $\beta_e = 0.6$ in the observation of Ganguli et al. [2018]. Here the ion and electron temperatures are assumed to be uniform for simplicity. Figure 2.2 (g) shows the ratio between the shear frequency ω_s and the lower hybrid frequency ω_{LH}. The shear frequency is defined as $\omega_s = V_{y,e}/L_E$ and describes the inhomogeneity of the electron flow. Here the ratio ω_s/ω_{LH} peaks at 3, which is within the unstable range. The electron plasma frequency $\omega_{pe} = \sqrt{\frac{Ne^2}{\epsilon_0 m_e}}$ and electron cyclotron frequency $\omega_{ce} = \frac{eB_Z}{m_e}$ are shown in Figure 2.2 (d) in blue and orange, respectively. The lower hybrid frequency

$\omega_{LH} = \frac{\omega_{pi}}{\sqrt{1+(\frac{\omega_{pe}}{\omega_{ce}})^2}}$ is shown in Figure 2.2 (h). The three frequencies are shown in units of the electron plasma frequency $\omega_{p0} = \sqrt{\frac{N_0 e^2}{\epsilon_0 m_e}}$ Earthward of the DF.

In this study, we use an electron thermal speed of $V_{the} = 0.1c$ and ion/electron temperature ratio of 4: $T_e = T_i/4 = T_0$. The ratio between electron plasma frequency and gyro frequency on the Earthward side is $\omega_{pe}/\omega_{ce} = 4$. A reduced mass ratio between ion and electron $m_i/m_e = 400$ is assumed. The ion and electron gyroradius on the Earthward side are $\rho_i = 16c/\omega_{pe}$ and $\rho_e = 0.4c/\omega_{pe}$, respectively. Here we choose the initial value of $L_E = 1.5c/\omega_{pe} = \rho_i/10.67 = 3.75\rho_e$ in the simulation so that ions can be effectively unmagnetized and electrons magnetized. The green shaded boxes in Figure 2.2 show the transition regions of the electromagnetic and plasma parameter profiles, which provide a rough estimation of the DF thickness as was used in observational analysis [e.g. Runov et al., 2011, Schmid et al., 2011]. Note that the initial DF thickness is $\sim 10\ c/\omega_{pe}$ considering the hyperbolic function form, and that the observed DF thickness is related to the saturated status of the instability. The DF thickness in this simulation is basically comparable to the ion scale length and consistent with observations [e.g. Fu et al., 2012b, Ganguli et al., 2018, Liu et al., 2018a]. The Alfvén speed based on B_0 and N_0 is $V_{A0} = 0.25c$.

An EMPIC model has been developed which is two-dimensional in the configuration space with three velocity components (2D3V). Both ions and electrons are fully kinetic, and the full set of Maxwell's equations are solved. In order to make use of the periodic boundary conditions, the simulation domain is doubled in the X direction and made symmetric about $x = L_X/2$. The system length is $L_X = 100c/\omega_{pe}$ and $L_Y = 50c/\omega_{pe}$ with $N_X \times N_Y = 1024 \times 512$ grid cells. The mean number of macro-particles per cell per species is 200. The time step is $0.01\omega_{p0}^{-1}$. Since the LH time scale is the natural time scale in the system, we use ω_{LH0}^{-1} as the unit where ω_{LH0} is the LH frequency Earthward of the DF.

2.3 Simulation Results

2.3.1 EIH Wave Spectrum

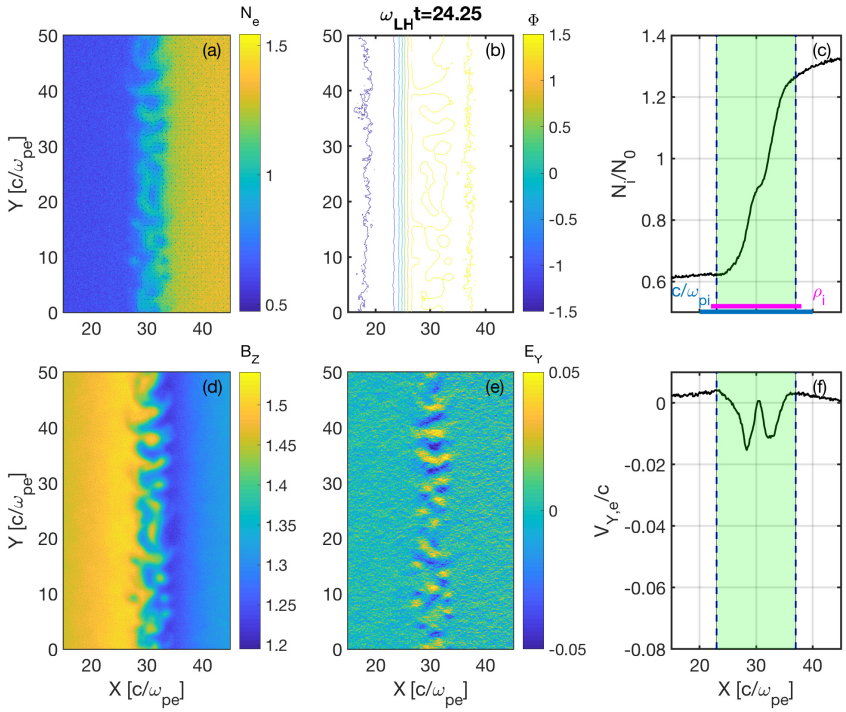

Figure 2.3: Plasma and electromagnetic field variables at t=24.25 ω_{LH0}^{-1}: (a) electron number density N_e, (b) electrostatic potential Φ, (c) cross section of ion density N_i, (d) B_Z, (e) E_Y, and (f) cross section of electron flow $V_{y,e}$.

Figure 2.3 shows the plasma density, electron velocity, and electromagnetic fields at t=24.25 ω_{LH0}^{-1} when the instability has evolved into the nonlinear stage. Figure 2.3 (a) shows rolled-up vortex structuring in the electron number density (N_e), which is characteristic of the EIH instability [Romero and Ganguli, 1993]. Figure 2.3 (b), (d), and (e) show coherent structures in the electrostatic potential Φ, B_Z, and E_Y. A rough estimation of the dominant wavelength is $4.2c/\omega pe$, which is comparable to the shear scale length. Figure 2.3 (c) and (f) show that the ion number density (N_i) still maintains a strong gradient while the electron

sheared flow ($V_{y,e}$) has been mostly depleted. The saturated DF layer is broadened to ~ 14 $c/\omega_{pe} = 0.7$ $c/\omega_{pi} = 0.9$ ρ_i, which is consistent with observations. Note the flow channel has a displacement along X due to the net magnetic gradient force as the ambipolar electric field is depleted by the instability.

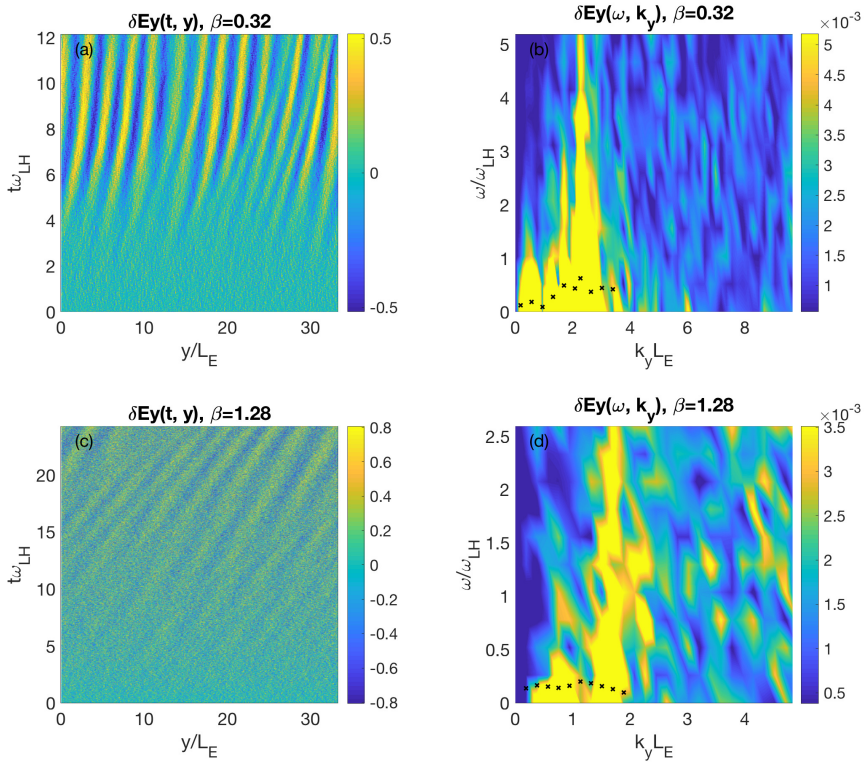

Figure 2.4: Wave mode characterization. (a-b) Time history of E_Y perturbation sampled along the flow direction in the DF, and the dispersion relation of the sampled E_Y. The black crosses indicate the growth rates of each k_y mode. (c-d) sampled E_Y perturbation time history and its dispersion relation for another test of $\beta = 1.28$ in the same format with (a-b).

In order to further characterize the wave modes, we sample the transverse electric field perturbation of E_Y along the flow channel in the DF. The time history of the one-dimensional sampling is shown in Figure 2.4 (a). It can be seen that periodic wave structures start to show up at $\sim 3\omega_{LH}^{-1}$. The wave fronts represented by the alternating strips indicate that

the wave mode is propagating along the positive Y axis toward dusk. The phase velocity estimated from the slope of the wave front is $\sim 0.004c$, which is comparable to the ion thermal velocity.

A two-dimensional Fourier analysis is applied to the space-time sampling of electric field perturbations shown in Figure 2.4 (a). The consequent dispersion relation is shown in Figure 2.4 (b). It can be seen that the dominant wave number is around $k_y L_E = 2$ and the frequency is broadband from 0 to $5\omega_{LH}$. At each sampled time, a spatial Fourier analysis is conducted to get the spectrum power of different wave numbers. The time history of the spectrum power for one k_y mode is linearly fitted to estimate the growth rate of that mode. The growth rates of a few wave modes around the dominant mode are indicated by the black crosses shown in Figure 2.4 (b). It can be seen that the fastest growth rate is also on the order of the lower hybrid frequency. The dispersion relation shown in Figure 2.4 (a-b) is consistent with the EIH theory that the fastest growing mode has a wavelength comparable to the shear scale length, the real frequency is broadband in the lower hybrid range, and the fastest growing mode has a growth rate comparable to the lower hybrid frequency [Romero et al., 1992].

2.3.2 EIH Dependence on Plasma β

We also explored the wave properties dependence on the plasma β. Another simulation was conducted in which the plasma thermal velocity is increased by a factor of two so that the plasma β in the Earthward direction is 1.28. It should be noted that the density gradient, driving electric field, and shear scale length are kept the same. The maximum B_Z at the tailward direction is slightly increased from $1.78B_0$ to $1.85B_0$. The wave structure and dispersion properties in the DF are shown in Figure 2.4 (c-d) in the same format with

Figure 2.4 (a-b). The wave pattern becomes visible after $\sim 10\ \omega_{LH}^{-1}$ (Figure 2.4 c). The dispersion relation in Figure 2.4 (d) indicates that the lower hybrid spectrum shrinks to a lower frequency band. The fastest growing wave number shifts to smaller values around $k_y L_E \sim 1$. The growth rate is reduced as the plasma β is higher. This is consistent with the theory [Ganguli et al., 2014] and observations of DF which indicate that the wave power is concentrated in the electrostatic regime.

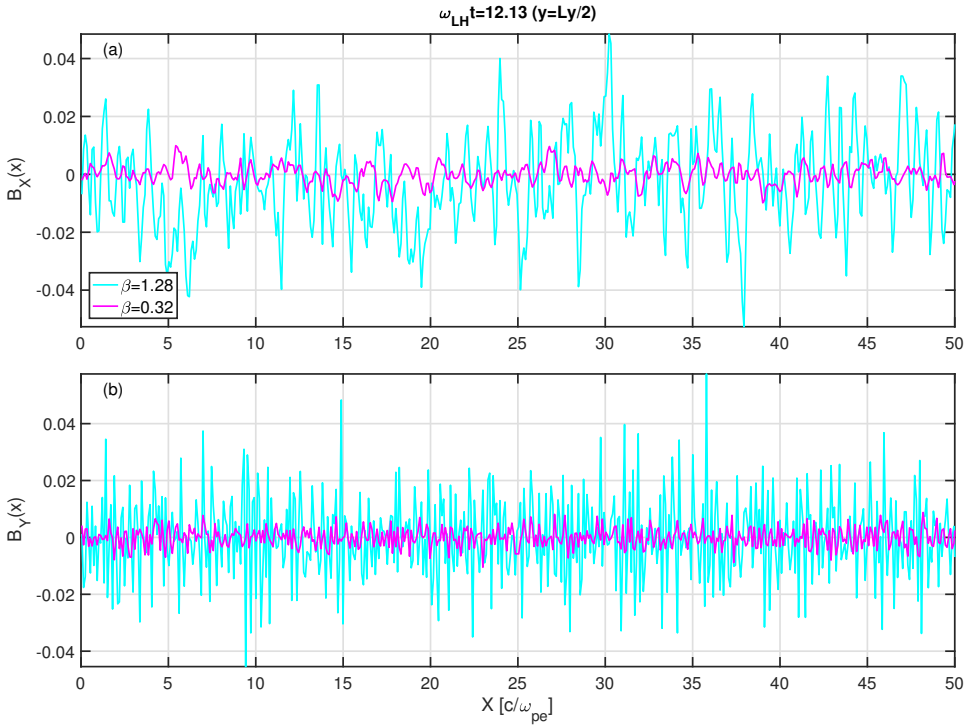

Figure 2.5: Comparison of electromagnetic perturbations between low and high β. The magnetic field components (a) B_X and (b) B_Y sampled along the X direction at $Y = L_Y/2$ are shown for two runs: $\beta = 0.32$ (magenta) and $\beta = 1.28$ (cyan).

The effects of plasma β are further evaluated by plotting the electromagnetic perturbations from the two simulations with low and high plasma β. Figure 2.5 shows the B_X and B_Y sampled at $t = 12.13\omega_{LH}^{-1}$ and $y = L_Y/2$ along the X direction. The results from the high β simulation are shown in cyan and from the low β in magenta. The magnetic perturbations in the high β simulation have a much larger amplitude than those from the low β simulation.

Considering that the background magnetic field is only different by 4% and that the high β case has a much lower growth rate, the direct comparison of magnetic perturbations here implies that the fluctuations driven by the transverse velocity shear at the DF are more electromagnetic with a higher β.

2.4 Discussion and Conclusion

In this study, we investigated velocity shear effects in a magnetotail dipolarization front with a two-dimensional electromagnetic PIC model. A simplified configuration was adopted in which the DF is treated as a boundary layer with an Earthward plasma density gradient, a tailward magnetic field B_Z gradient, and an Earthward ambipolar electric field E_X. The velocity shear mainly results from the inhomogeneous electric field which represents the global compression effects. The particle distribution deviated from Maxwellian, which provides the free energy for the EIH wave emission.

It should be pointed out that the EIH mechanism is different from the LHDI. Firstly, the energy source of EIH instability is the velocity shear while the LHDI is driven by density gradients. The EIH does not require a density gradient (Figure 2.3c) but depletes the velocity shear and relaxes the DF (Figure 2.3f) [Romero et al., 1992]. This may explain why DF electron jets are not commonly reported although a statistical survey is needed to evaluate the occurrence. Secondly, the saturated EIH state is featured by vortex structure (Figure 2.3a), distinct from the "finger" structures of LHDI [Divin et al., 2015a, Pritchett and Coroniti, 2010]. On the other hand, uniform $\vec{E} \times \vec{B}$ drift velocity is typically assumed for the study of the LHDI [e.g., Daughton, 2003]. This may be problematic for DF studies since when the scale size of the density gradient becomes comparable to an ion gyroradius (as typically found in DFs) the assumption of uniform drift does not hold [Ganguli et al.,

2018].

The DF thickness in the simulations presented in this study is representative of the ion scale length as has been found in observations [e.g., Fu et al., 2012b, Ganguli et al., 2018, Liu et al., 2018a, Runov et al., 2009, 2011, Schmid et al., 2011]. Note that the DF thickness in observations are usually estimated with the timing method. This method derives the propagation velocity of the DF based on two or more satellites that are close enough to each other, and estimates the duration of DF passing with the local minimum and maximum of the magnetic field profile. The DF thickness is then estimated as the product of the propagation velocity and duration time. In this simulation study, the model is set in the frame of the DF thus there are no propagation effects. The magnetic profile is simplified with a hyperbolic tangent like function, thus there are no local maximum or minimum. Instead, the DF thickness is estimated with the distance between the asymptotic points of the profile. It should be clarified that the shear scale length L_E used in this initialization is 1.5 c/ω_{pe}, which is equivalent to 0.075 c/ω_{pi}. However, the DF thickness based on the method typically used in observations is about 10 c/ω_{pe}, as shown by the green shaded boxes in Figure 2.2. This thickness is equivalent to 0.5 c/ω_{pi} or 0.6 ρ_i, as shown by the blue and magenta bars in Figure 2.2, respectively. It should be pointed out that the DF thickness is broadened as a result of the wave emission driven by the EIH instability. As shown in Figure 2.3 (c), the DF thickness has increased to $\sim$ 14 c/ω_{pe} by 24.25 ω_{LH0}^{-1}, which is equivalent to 0.7 c/ω_{pi} or 0.9 ρ_i. Here c/ω_{pi} and ρ_i are both based on the initial values Earthward of the DF. Considering that the Earthward density increased slightly by 24.25 ω_{LH0}^{-1}, the actual ion inertial length is smaller than the value at initialization and closer to the DF thickness.

The simulation was run for $24.25\omega_{LH}^{-1}$ or equivalently $1.25\Omega_{ci}^{-1}$, when the saturated states still hold. In another run that is not shown here, the initial shear scale length is doubled ($\mathrm{L_E} = 3.0\mathrm{c}/\omega_{\mathrm{pe}}$). The electron flow channel width is broadened to $1.9\rho_i$ or equivalently

$1.5c/\omega_{pi}$. Although the shear frequency is lower than that in the simulation presented here, the EIH instability still develops very well. We present the results for $L_E = 1.5c/\omega_{pe}$ because the physics is similar while the computation is simpler considering that the system length needs to be commensurate with the shear scale length. It is also noteworthy that the flow channel in the saturated stage is shifted in the direction transverse to the flow, which is caused by the force balance. As the electron flow is depleted, the magnetic gradient force compresses the DF, which results in the Earthward displacement of the initial DF.

Uniform electron and ion temperatures are used in this simulation study although the temperatures typically have a gradient across the DF in satellite observations and self-consistently formed DFs [e.g. Lu et al., 2016b, Runov et al., 2009, 2011]. In fact, the temperature in the MMS observation of DF reported by Ganguli et al. [2018] is negligible. This event is used in our simulation because its equilibrium physics is thoroughly analyzed thus provides a firm basis to study the nonlinear evolution. On the other hand, the temperature gradient in DF is usually found to be in the opposite direction to the density gradient, which reduces the pressure gradient and hence the diamagnetic drift but not the ambipolar electric field driven $\vec{E} \times \vec{B}$ drift. This will further enhance the EIH waves and retards the lower hybrid drift or other pressure gradient driven waves.

The higher plasma β in the study of EIH dependence on β is achieved by increasing the temperature of electrons and ions while keeping the other parameters such as the shear scale length L_E the same. The challenge of using a larger β in the simulation is that the shear scale length and the system length have to increase accordingly with the electron/ion gyro radius while the electron gyroradius has to be resolved to achieve the $\vec{E} \times \vec{B}$ drift motion. Considering that DF thickness is usually comparable to the ion gyroradius, a larger plasma β may imply a thicker DF boundary layer thus a lower shear frequency. Here we control the variables such as L_E to highlight that with increasing β the wavelengths of the EIH

waves become longer and they become increasingly electromagnetic. This is important since although the power in DF emission is mostly in the electrostatic regime there is also some power in the electromagnetic regime. The velocity shear generated EIH waves display this character. This has important physics implications since it implies that most of the energy goes into particle energization in the DF frame as the electrostatic power dissipates rather than be transported away from the DF as Poynting flux by the electromagnetic waves.

When DFs are propagating toward the Earth, there is a convection electric field along the dusk direction. However, in this study, the EIH instability is investigated in the reference frame moving with the DF thus there is no convection electric field in the dawn-dusk direction. The ambipolar electric field along the X direction is not affected by the Earthward motion. The ratio between the ion gyroradius and the shear scale length used in the simulation is necessarily larger than that observed at the DF. It is chosen here to make use of the initial equilibrium derived in Romero and Ganguli [1993] that can be readily implemented, and guarantees that ions are effectively unmagnetized and the electrons magnetized.

The DF configuration adopted in this simulation is simplified however it retains the critical aspects of the velocity shear driven wave emissions at the DF. A three-dimensional PIC model starting from magnetotail current sheet configuration may provide a global view of the DF that is self-consistently generated from the magnetotail reconnection with Earthward propagation effects. However, the EIH mechanism discussed in this study is essentially on the kinetic scale and a locally dissipative process. It requires resolving the electron-ion charge separation scale and time scale much below the ion gyro period. A local electromagnetic PIC model is sufficient for such a purpose. Achieving such resolution in a global PIC model is still not practical.

This study provides the first electromagnetic kinetic simulation of the local dissipation in DF due to velocity inhomogeneities. It is highlighted that the velocity shear substantially con-

tributes to the wave emissions at the magnetotail dipolarization fronts. The EIH mechanism is suggested to be applicable for the generation of broadband lower hybrid waves at DFs. The transition of the EIH instability to more electromagnetic fluctuations with increasing plasma β implies that waves with more electromagnetic properties could propagate away from the DF and may affect other magnetospheric particle populations, e.g. the inner magnetosphere particles. The shear driven wave modes have implications for the energy dissipation and particle dynamics at the DF. Recent theoretical advances show that the EIH driven waves are formally electromagnetic especially when the wave vector has a finite parallel component [Ganguli et al., 2014]. In order to fully characterize the electrostatic and electromagnetic effects of the shear driven emissions at the DF, it is necessary to extend the current 2D model to 3D and global model and consider a broader range of plasma parameters in the future. Whistler mode waves are also suggested to be excited by the velocity shear when there is a finite parallel component of wave vector [Ganguli et al., 2014]. Since the magnetic field enhancement at DFs is often preceded by a decrease [e.g., Liu et al., 2013, Lu et al., 2016b, Shi et al., 2014], it is also necessary to consider how the DF-dip could affect the particle distribution and velocity shear at the DF.

2.5 Acknowledgement

This study was funded by NASA MAG16_2-0050. The authors acknowledge Advanced Research Computing (ARC) at Virginia Tech and the Space Computer Center (SpaceCC) of the Electrical and Computer Engineering Department for providing computational resources and technical support that have contributed to the results reported within this paper. Simulation data, simulation codes, and analysis routines are being preserved on the SpaceCC server and will be made available upon written request to the lead author (ldong7@vt.edu).

Chapter 3

Global MHD Modeling of Cross Polar Cap Potential

Dong Lin[1,2], Binzheng Zhang[2,3], Wayne A. Scales[1], Michael Wiltberger[2], C. Robert Clauer[1], and Zhonghua Xu[1] (2017), The Role of solar wind density in cross polar cap potential saturation under northward interplanetary magnetic field, *Geophys. Res. Lett. 44* (23), 11,729-11,734, doi:10.1002/2017GL075275.

[1] Bradley Department of Electrical and Computer Engineering, Virginia Polytechnic Institute and State University, Blacksburg, Virginia, USA

[2] High Altitude Observatory, National Center for Atmospheric Research, Boulder, Colorado, USA

[3] Department of Earth Sciences, the University of Hong Kong, Pokfulam, Hong Kong

Abstract

The role of solar wind density in the cross polar cap potential (CPCP) response under northward interplanetary magnetic field (IMF) is investigated with observation-based global simulations. A rare event was reported by Clauer et al. [2016] during which the ionospheric electric field E_{ISP} does not saturate under extreme interplanetary electric field (IEF) of ~15 mV/m. While commonly utilized coupling functions based on IEF fail to provide an unambiguous explanation for the linear response, the LFM-MIX model is used to explore

the mechanisms in this study. The model first reproduces the observed linear features of the E_{ISP}. The simulated CPCP also responds linearly to IEF variations. A controlled simulation is designed with solar wind density artificially reduced to 10% of the observed value while all other parameters such as the IEF are kept the same. The controlled simulation shows saturation of the E_{ISP} as well as the CPCP. Further analysis shows the difference in the magnetosheath plasma β, implying the distinct dominant forces between the two simulations. The Lopez magnetosheath force balance theory is used to explain the CPCP responses under different solar wind densities. This comparison study highlights the role of solar wind density in determining the magnetosphere-ionosphere response to extreme interplanetary drivings.

3.1 Introduction: Cross Polar Cap Potential

Ionospheric cross polar cap potential (CPCP) is generated as the the solar wind drives ionospheric convection. The CPCP is a critical indicator of the coupling efficiency of solar wind momentum and energy into the magnetosphere-ionosphere system. The CPCP is generally believed to be dependent on the interplanetary electric field (IEF) which determines the reconnection on the dayside magnetopause. Previous studies have shown that the CPCP responds to the IEF linearly at low and moderate values, and becomes saturated at large values for both southward and northward interplanetary magnetic field (IMF) [e.g., Reiff et al., 1981, Shepherd et al., 2002, Sundberg et al., 2009, Wilder et al., 2008]. For southward IMF conditions, the CPCP saturates at around 50 to 100 kV when the IEF is above 3 mV/m, i.e. 20 kV/R_E, where R_E is Earth radii [Shepherd et al., 2002]. For northward IMF conditions, the CPCP also saturates when the IEF reaches 3-5 mV/m, with a saturation level of about 20 kV [Wilder et al., 2008].

Solar wind coupling functions have been widely used to describe the interaction between

the solar wind (SW) and the magnetosphere-ionosphere (M-I) system [e.g., Gonzalez, 1990, Kan and Lee, 1979, Newell et al., 2007, Wilder et al., 2008]. These functions generally consider that the coupling processes almost exclusively depend on the solar wind velocity and IMF, and use the IEF as the basis through incorporating the effects of IMF clock angle and sometimes together with the CPCP saturation effect [e.g., Kan and Lee, 1979, Wilder et al., 2008]. Although studies have shown that non-electrodynamic aspects of the solar wind driving such as the dynamic pressure may also play a role in the SW-M-I coupling [e.g., Lopez et al., 2004, Palmroth et al., 2004, Pulkkinen et al., 2007, Siscoe et al., 2002], the upstream solar wind number density has received less attention in the electrodynamic coupling in the SW-M-I system, especially under northward IMF.

Recently Clauer et al. [2016] (hereinafter referred to as Clauer16) reported a rare event showing the failure of predicting CPCP saturation using SW coupling functions based on IEF only, that is, the CPCP did not saturate under large northward IMF conditions as expected. In the Clauer16 event, an interplanetary shock impacts the Earth at around 16:00 UT on 12 September 2014, after which there is an extended period of large northward IMF (up to 30 nT) and solar wind speed of 600 km/s. In this unsaturated event, the driving IEF surges up to 15 mV/m, which is an extreme value much beyond where CPCP usually exhibits saturation. The E_{ISP}, which is measured by the northward facing Resolute Incoherent Scatter Radar (RISR-N) near the local noon at 84° magnetic latitude, shows linearly correlated variation with the solar wind electric field without any saturation as expected.

The coupling functions that uniquely depend on the IEF can not account for the observed response of the E_{ISP} in the Clauer16 event. The absence of saturation behavior motivates us to explore the role of solar wind parameters other than IEF in the coupling between the SW and the M-I system. In the Clauer16 event, due to the impact of an interplanetary shock, the solar wind number density during the unsaturated period is between 20-30 cm^{-3}

which is much higher than the common value between 1-5 cm^{-3}. Therefore, the question can be asked whether the upstream solar wind number density regulates the response of the ionospheric electric field during this unexpected event. In this study, we use controlled event simulations from a global SW-M-I model to investigate the role of solar wind number density on the response of E_{ISP} and CPCP under extreme IEF values with northward IMF driving conditions.

3.2 Model and Observation Comparison

The LFM-MIX model has been extensively used in the study of SW-M-I interactions [e.g. Wang et al., 2004, Wiltberger et al., 2004]. The Lyon-Fedder-Mobarry (LFM) global MHD model solves ideal MHD equations for the three-dimensional solar wind-magnetosphere interactions with electrostatic coupling between the magnetosphere and ionosphere [Lyon et al., 2004a]. The Magnetosphere-Ionosphere Coupler/Solver (MIX) module treats the ionosphere as a two-dimensional spherical shell, on which the equation of current continuity combined with a height-integrated Ohm's law for the ionosphere is solved [Merkin and Lyon, 2010a]. The precipitation model for ionospheric conductance is illustrated in Zhang et al. [2015]. In this study, the LFM model is run with the standard double-resolution, i.e. $53 \times 48 \times 64$ cells in the radial, meridional, and azimuthal directions, respectively. The MIX ionospheric solution is computed on a 2 degree $\times$ 2 degree magnetic latitude and longitude grid.

The solar wind and IMF conditions for the Clauer16 event is shown in Figure 3.1, which has 1 minute resolution and is extracted from NASA/GSFC's OMNI data set through CDAWeb. After the arrival of the interplanetary shock at the Earth around 16:00 UT on 12 September 2014, there is an extended interval of strong driving of the magnetosphere-ionosphere by the solar wind. The IMF magnitude increases to 30 nT and is mostly northward dominant while

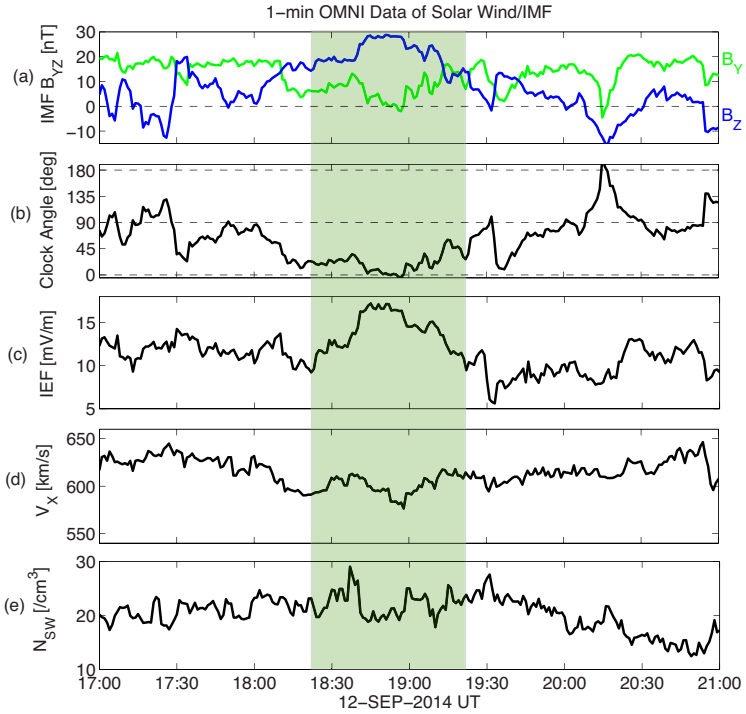

Figure 3.1: 1-min resolution OMNI data for solar wind and IMF conditions from 17:00 to 21:00 UT on 12 September 2014. From top to bottom are (a) IMF Y (green) and Z (blue) components in the GSM coordinate, (b) clock angle, (c) IEF, (d) X component of solar wind velocity, and (e) solar wind number density. The light green shaded interval is from 18:20 to 19:20 UT, during which IEF has a substantial variation and CPCP is investigated in the following section.

the IEF approaches 15 mV/m. The solar wind velocity is relatively steady at around 600 km/s and has variations less than 10% during this interval. The solar wind number density is above 20/cm^3, which is very high and rarely associated with such strong IMF given the very large solar wind velocity at the same time. In order to investigate the role of solar wind number density, a second simulation was conducted with solar wind density (N_{SW}) reduced to 10%, i.e. about 2/cm^3 while all other parameters are kept the same. In the following discussions, the event simulation driven by the real solar wind density is referred to as the "Real N_{SW} run", and the controlled simulation driven by low solar wind density is referred to as the "0.1 N_{SW} run".

Figure 3.2(a) shows the relationship between the IEF and the simulated time series of the E_{ISP} during the Clauer16 event. The IEF is shown with the black curve and referring to the left vertical axis, which is directly extracted from a fixed location in the model, namely at +30 R_E at the Z-axis above the geomagnetic north pole. The E_{ISP} is evaluated at the same location as the RISR-N observation, i.e. at 84° magnetic latitude, rotating with the Earth and passing the local noon at 19:00 UT. This location is near the throat of the reverse convection cell as indicated by the magenta dots in Figure 3.4 (a) and (b). The horizontal E_{ISP} is derived from the gradient of the electrostatic ionospheric potential at a two-minute cadence. The E_{ISP} time series refer to the right vertical axis. The yellow curve is derived from the Real N_{SW} run and the blue curve from the 0.1 N_{SW} run. The shaded interval marks when the IEF has substantial increase and the IMF is dominantly northward, as shown in Figure 3.1.

In order to make more straightforward comparisons, the E_{ISP} has been shifted by 18 minutes to align with the time series of the simulated IEF from both simulations. This time shift is due to the response of the SW-M-I system to changes in IEF at X=0, and is estimated with visual inspection of the entire interval. It is evident that in the Real N_{SW} run (yellow curve), the E_{ISP} responds approximately linearly to variations in the time series of the IEF. Specifically, the IEF increases from ∼6 mV/m to ∼15 mV/m then decreases to ∼10 mV/m from 18:20 to 19:20 UT, as shown by the shaded interval. The event simulation reproduces the electric field observations in Figure 3.2(b) as reported by Clauer16. The observed E_{ISP} (yellow curve) follows the solar wind electric field (black curve) and reaches a maximum of 150 mV/m when the IEF increases to the peak value. Therefore the simulated E_{ISP} is in agreement with the RISR-N measurements without noticeable saturation driven by the peak IEF of around 15 mV/m.

The corresponding E_{ISP} derived from the 0.1 N_{SW} run is shown with the blue curve in

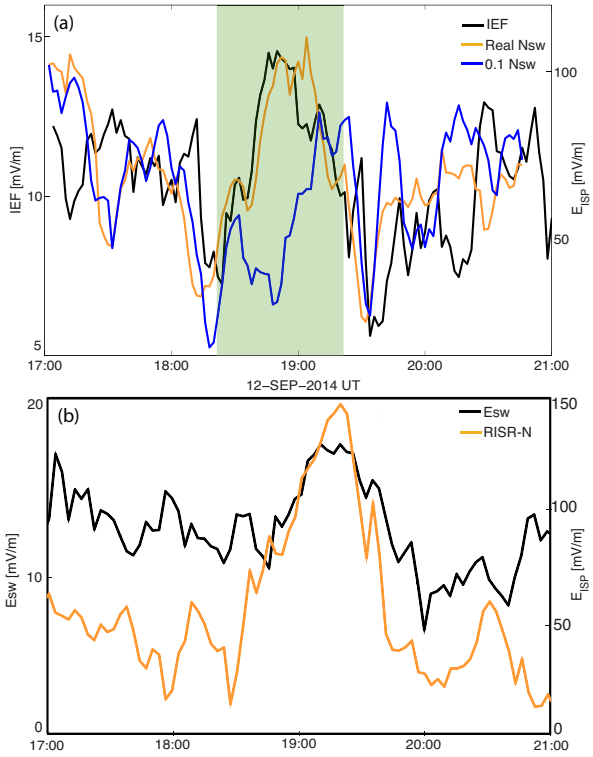

Figure 3.2: Comparison of electric fields on 12 September 2014: (a) IEF in the YZ plane (black), simulated E_{ISP} in the Real N_{SW} run (yellow) and 0.1 N_{SW} run (blue). The E_{ISP}s are shifted by 18 minutes to align best with the IEF by visual inspection. (b) Observed IEF (black) and radar measured E_{ISP} (yellow) in Clauer16. In both panels the IEF refers to the vertical axis on the left and the E_{ISP} refers to the right. The shaded interval corresponds to that in Figure 3.1 from 18:20 to 19:20 UT.

Figure 3.2(a). When the solar wind density is artificially reduced by 90%, the simulated E_{ISP} at the RISR-N location does not respond linearly with the increase of IEF and appears to saturate between 18:20 UT and 19:20 UT when the driving IEF is greater than 10 mV/m.

The E_{ISP} is dependent on the pattern of the ionospheric electrostatic potential as well as the local conductivities. Although the sampled location for electric field response analysis is favorable to represent the CPCP response as discussed in Clauer et al. [2016], it is necessary to examine the behavior of CPCP directly. The distinct responses in the simulated E_{ISP} are also evident in the simulated CPCP and field-aligned current (FAC) during the Clauer16 event.

The simulated CPCP is calculated as the difference between the maximum and minimum ionospheric potential. The simulated FAC is calculated as the total current density that flows into the ionosphere, which is mainly NBZ currents under very large northward IMF. The time series of simulated CPCP, FAC, and the IEF are illustrated in Figure 3.3 for the interval from 18:20 to 19:20 UT. Figure 3.3(a) shows the responses of CPCP and total FAC in the two simulations driven by Real N_{SW} and 0.1 N_{SW}, respectively. The CPCP and FAC for the Real N_{SW} run are shown with the yellow curves in Figure 3.3(a) and (b), which exhibit consistent variations with the IEF as shown in Figure 3.3(c). The CPCP and FAC for the 0.1 N_{SW} run stays around a much stabler level as denoted by the blue curves in Figure 3.3(a) and (b).

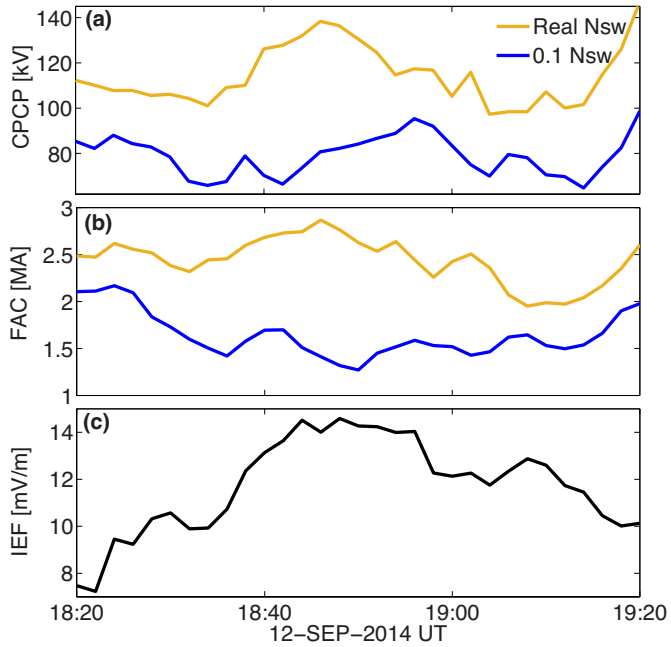

Figure 3.3: Simulated CPCP, FAC, and IEF from 18:20 to 19:20 UT, i.e. the shaded interval in Figure 3.1 and 3.2. (a) CPCP in the Real N_{SW} run (yellow) and 0.1 N_{SW} run (blue). (b) Total FAC with a similar format. (c) measured IEF in the YZ plane. The CPCP and FAC series are shifted backward by 18 minutes to align with the IEF.

The comparison between the two simulations illustrates the importance of solar wind density

in determining the response of the coupled magnetosphere-ionosphere system driven by the IEF. Figure 3.4 shows the comparisons of simulated magnetospheric-ionospheric status at 19:00 UT between the simulations with Real N_{SW} (left column) and 0.1 N_{SW} (right column). Figure 3.4 (a-b) show the ionospheric FAC density (filled color) and the electrostatic potential (contour curves). The FAC density refers to the common color bar. The potential contours are shown at multiples of 10 kV. The total FAC flowing into the ionosphere is 2.7 MA and 1.5 MA, and the total CPCP is 131.8 kV and 73.4 kV in the Real N_{SW} run and 0.1 N_{SW} run, respectively. The minimum and maximum FAC density and potential are annotated at the left and right bottom of the respective panels. The magenta dots denote the location of the RISR-N radar at 19:00 UT, which is roughly at local noon and 84° magnetic latitude. Figure 3.4 (c-d) show two snapshots of the configuration of the equatorial magnetosphere at 19:00 UT from the two simulations, with the color bar denoting the instantaneous plasma β defined as P_{fluid}/P_{mag}, where P_{fluid} is the thermal pressure and P_{mag} is the magnetic pressure. The plasma β is shown on a common color scale of base-10 logarithm between -5.0 and 1.5 in order to make direct comparisons. The white curves represent the boundaries between the open and closed magnetic field lines, which is an indication of the magnetopause boundary (most valid in the dayside). In Figure 3.4(c) for the Real N_{SW} run, the subsolar magnetopause is located around 8 R_E and the subsolar bow shock is around 10 R_E, resulting in a magnetosheath with 2 R_E width in the subsolar direction. In Figure 3.4(d) for the 0.1 N_{SW} run, the subsolar magnetopause is around 10 R_E, and the nose of the bow shock is at nearly 20 R_E, resulting in a more expanded magnetosphere and a much thicker magnetosheath compared to the Real N_{SW} run. The solid and dashed black contours correspond to $\log_{10}\beta$ of 0.0 and -1.0, i.e. β of 1.0 and 0.1, respectively.

The width of the magnetosheath plays an important role in regulating the dayside magnetic reconnection between the IMF and the geomagnetic fields [Zhang et al., 2017a]. The

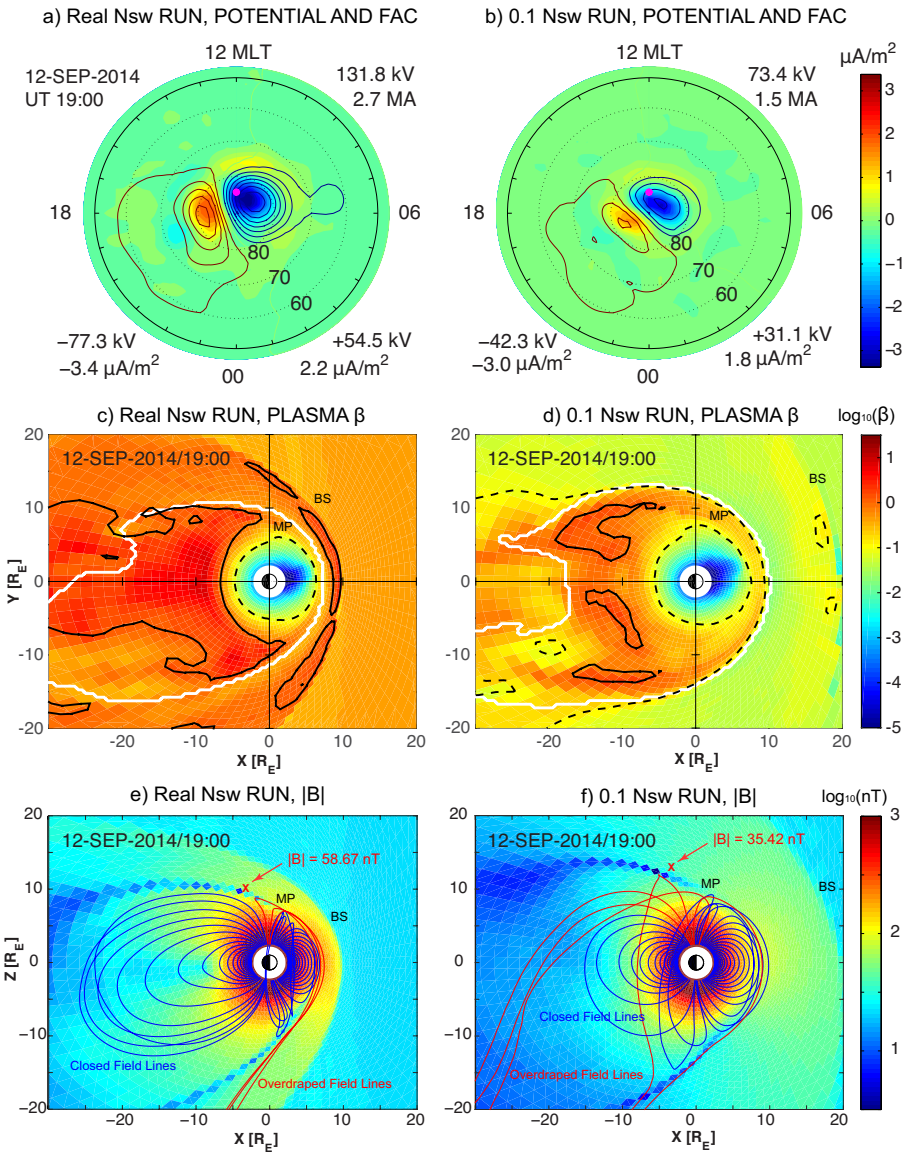

Figure 3.4: Comparison of magnetospheric-ionospheric status at 19:00 UT for the simulation with Real N_{SW} (left column) and 0.1 N_{SW} (right column). (a-b) Ionospheric FAC density (color coding) and electrostatic potential (contours). (c-d) Plasma β (log_{10} color scale) in the equatorial plane. (e-f) Magnetic field magnitude in the magnetosphere noon-midnight meridian plane. See text for details.

difference in the simulated width of the magnetosheath between the two controlled simulations is a consequence of the difference in the upstream solar wind density. As is shown in the Real N_{SW} run, the combination of high solar wind number density and large magni-

tude of IMF leads to a magnetosheath plasma β that is greater than unity. According to the magnetosheath Force-balance theory of Lopez et al. [2010], the dominant force in the magnetosheath is the pressure gradient force (∇P) rather than the Lorentz force ($\vec{J} \times \vec{B}$), when the magnetosheath β is greater than 1, regardless of the intensity of the IEF. In this case, as IMF B_Z increases, solar wind magnetic flux is continuously transported to the magnetopause by the magnetosheath flow without significant diversion away from the magnetopause boundary. The result is a linear increase of reconnection rate and ionospheric CPCP. In the controlled simulation driven by 0.1 N_{SW}, the combination of nominal solar wind number density and large magnitude of IMF leads to a much lower magnetosheath plasma β below 0.1, suggesting that in the 0.1 N_{SW} run the magnetosheath force is dominated by the $\vec{J} \times \vec{B}$ force, which increases with the magnitude of the IMF. As IMF B_Z increases, more solar wind magnetic flux is diverted in the magnetosheath before it reaches the magnetopause boundary. Therefore the response of the ionospheric CPCP and electric fields are nonlinear with evident saturation.

Figure 3.4 (e-f) show the magnitudes of the simulated magnetic field in the noon-midnight meridian plane, together with the topology of the magnetic field lines with at least one footprint connecting to the northern hemisphere, from the Real N_{SW} run and the 0.1 N_{SW} run respectively. The magnetic field near the subsolar magnetopause is much stronger in the Real N_{SW} run than in the 0.1 N_{SW} run. The different field strengths result from pressure equilibrium under different solar wind densities despite the same upstream IMF. In both simulations, the orientations of magnetic field lines in the magnetosphere and magnetosheath near the subsolar point are northward, suggesting little magnetic reconnection at the subsolar point as expected from northward IMF driving. The blue curves are closed magnetic field lines, and the red are overdraped field lines connecting to IMF in the southern hemisphere, which are consequences of high-latitude reconnection under northward IMF [e.g., Crooker,

1992]. In the 0.1 N_{SW} run, the strength of the simulated magnetic field near the overdraped field lines (as indicated by the red cross in Figure 3.4 (e)) is about 35.42 nT, which is much lower than that of 58.67 nT in the Real N_{SW} run. Since the magnetic reconnection rate is regulated by the strength of the magnetic field near the reconnection zone, to zeroth order, the reconnection rate at high-latitude magnetopause is expected to be about 40% lower in the 0.1 N_{SW} run, which is approximately consistent with the corresponding CPCP reduction. Note that due to the complexity in the upstream driving conditions and the dynamic response in the SW-M interaction, high-latitude reconnection may also happen outside the noon-midnight meridian cut plane, thus a more thorough analysis is necessary in the future to quantify the differences in the topology of the magnetic field and the rate of the reconnection that account for the exact CPCP reduction. However, the response of the field strength in the magnetosheath shown in Figure 3.4 (e-f) does suggest that the response of the coupled SW-M-I system to very large northward IMF with different solar wind densities is well rendered in this study.

3.3 Summary

In this study, the LFM-MIX global magnetosphere-ionosphere model was used to simulate the cross polar cap potential response to an interval of extreme solar wind conditions. The simulated ionospheric electric field consistently reproduces the observations. Both the CPCP and the ionospheric electric field exhibit a linear response to the very large solar wind electric field for this event, which reaches 15 mV/m. A controlled simulation shows that the CPCP saturates when the solar wind density in the event is artificially reduced by one order of magnitude. The magnetosheath plasma β is higher than unity with real solar wind conditions, but much lower than unity in the controlled simulation with 0.1 N_{SW}. The mag-

netosheath force balance model of [Lopez et al., 2010] is found to be applicable under the extreme driving conditions of the Clauer16 event. The event-based simulations highlight the role of solar wind density in SW-M-I coupling and provide implications for constructing more robust solar wind-magnetosphere-ionosphere coupling functions.

3.4 Acknowledgement

The research was supported by the Advanced Study Program of the National Center for Atmospheric Research (NCAR). Work at Virginia Tech was supported by NASA MAG16_2-0050. Computing resources were provided by the CISL at NCAR. NCAR is sponsored by the National Science Foundation (NSF). We acknowledge use of NASA/GSFC's Space Physics Data Facility's CDAWeb service, and OMNI data. Dong Lin is thankful to Dr. William Lotko for his assistance in fulfilling this paper. Michael Wiltberger was serving at the NSF during the production of this paper. Any opinion, findings, or conclusions or recommendations expressed in this material are those of the authors and do not necessarily reflect the views of the NSF. Simulation data, simulation codes, and analysis routines are being preserved on the NCAR High Performance Storage System and will be made available upon written request to the lead author (ldong7@vt.edu).

Chapter 4

Coupled LTR Modeling of Subauroral Polarization Streams

Dong Lin[1,2], Wenbin Wang[2], Wayne A. Scales[1], Kevin Pham[2], Jing Liu[2], Binzheng Zhang[2], Viacheslav Merkin[3], Xueling Shi[1], Bharat Kunduri[1], and Maimaitirebike Maimaiti[1] (2019), SAPS in the 2013 March 17 Storm Event: Initial Results from the Coupled Magnetosphere-Ionosphere-Thermosphere Model, *manuscript submitted to Journal of Geophysical Research: Space Physics*.

[1] The Bradley Department of Electrical and Computer Engineering, Virginia Tech

[2] High Altitude Observatory, National Center for Atmospheric Research

[3] The Applied Physics Laboratory, John Hopkins University

Abstract

Subauroral polarization stream (SAPS) are latitudinally narrow flow channels of large westward plasma drifts in the subauroral ionosphere. In this study, the global structure and dynamic evolution of SAPS are investigated by using the Coupled Magnetosphere-Ionosphere-Thermosphere (CMIT) model with Ring Current extension, namely the LFM-TIEGCM-RCM (LTR) model, to simulate the 2013 St. Patrick's Day storm event. This is the first time that the global distribution and temporal evolution of SAPS are investigated using first-principle models. The model shows a strong westward ion drift channel formed equa-

torward of the auroral electron precipitation boundary on the duskside, which is identified as the SAPS structure. The simulated ion drift velocity and auroral electron precipitation sampled along the trajectory of the DMSP F18 satellite are in good agreement with the satellite measurements. SAPS initiate in the pre-dusk sector when the interplanetary magnetic field (IMF) turns southward. SAPS latitude generally decreases with magnetic local time (MLT) from dusk to midnight. The SAPS channel shows wedge, inverse wedge, and crescent morphologies during the storm, and becomes discontinuous when the IMF is weakly southward. The SAPS mean latitude has a correlation coefficient of 0.77 with the Dst index. The mean latitude moves equatorward and the flow channel broadens in the storm main phase. The simulation results illustrate both the global distribution and highly dynamic behavior of SAPS that are not readily apparent from the observation data.

4.1 Introduction: Subauroral Polarization Streams

Ionospheric subauroral convection is frequently characterized by enhanced westward flows driven by strong poleward electric field during geomagnetically active times [Foster and Burke, 2002]. The flow channel spans the duskside to post-midnight and has a latitudinal width of a few degrees. The peak magnitude of the drift velocity ranges from a few hundred m/s to a few km/s. Historically, the localized ($1^\circ - 2^\circ$ latitudinal width) and intense ($> 1km/s$) flow channels near midnight have been termed as polarization jets or subauroral ion drifts (SAID) [Galperin et al., 1974, Spiro et al., 1979]. Broader regions of westward plasma drift equatorward of auroral electron precipitation have also been reported [e.g., Foster and Vo, 2002, Yeh et al., 1991]. Foster and Burke [2002] suggested an inclusive name for these subauroral flows: subauroral polarization streams (SAPS).

The average characteristics of SAPS have been described in statistical studies. Foster and Vo

[2002] surveyed 22 years of data from the Millstone Hill incoherent scatter radar and found that SAPS are persistent from dusk to the early morning sector for all Kp greater than 4 conditions. It was also found that the peak velocity is on average $>$ 900 m/s premidnight and 400 m/s in the predawn sector. The latitudinal width is generally 3° to 5°. Another statistical study based on the Super Dual Auroral Radar Network (SuperDARN) radars shows that SAPS can be observed 15% of the time during relatively quiet conditions ($-10nT < Dst < 10nT$), and 87% of the time during moderately disturbed conditions ($-75nT < Dst < -50nT$) [Kunduri et al., 2017]. During quiet times, SAPS are found to be localized to the midnight sector and centered above 60° magnetic latitude. During moderately disturbed conditions, SAPS are found to be centered at 20 MLT and below 60° magnetic latitude. The SAPS velocities are found to increase nearly linearly with MLT during low and moderate geomagnetic activities. SAPS have also been studied with satellite data such as the Defense Meteorological Satellite Program (DMSP). He et al. [2017] analyzed the different evolution patterns of SAPS during intense storms and quiet time substorms with DMSP data. They found that SAPS usually occur 0-3 hours after the beginning of the storm main phase and 0-2 hours after the substorm expansion onsets. While the statistical studies can provide the average picture of SAPS under different external driving conditions, it has been a challenge so far to fully describe the global structure of SAPS and how they evolve in a dynamic manner during particular events.

SAPS have been found intimately connected to the multi-way coupling among the solar wind, magnetosphere, and ionosphere-thermosphere. The generation and evolution of SAPS are closely related to the southward IMF [He et al., 2017, **?**]. Observations have shown that SAPS/SAID are coincident with the Region 2 Field-Aligned Current (FAC) flowing into the ionosphere and ion precipitation [e.g., Anderson et al., 2001, He et al., 2014, 2016, Yuan et al., 2016, 2017]. When mapping along the magnetic field line to the magnetospheric equatorial

plane, SAPS peak locations have been shown to correspond to the inner edge of the ion plasma sheet and are close to the peak of the ring current [Huang and Foster, 2007]. SAPS flow variations are often connected to earthward plasma sheet flow bursts and the plasma pressure distribution in the ring current [e.g., Clausen et al., 2012, Ebihara et al., 2009, Gallardo-Lacourt et al., 2017, Lyons et al., 2015]. The development of SAPS is suggested to be associated with the injection of plasma sheet ions/electrons, which establishes the polarization electric fields [e.g., Califf et al., 2016, Garner et al., 2004, Lejosne et al., 2018, Makarevich and Dyson, 2008, Mishin et al., 2017, Yuan et al., 2017]. It is also demonstrated that the SAPS electric field can erode the outer plasmasphere, which also correlates with the generation of storm enhanced density (SED) and plumes of elevated ionospheric total electron content (TEC) on the dayside [e.g., Foster and Rideout, 2005, Foster et al., 2002, 2007, 2014]. SAPS channels are found to be located in a region of low TEC values, which implies low ionospheric conductivity [e.g., Clausen et al., 2012, He et al., 2018, Shinbori et al., 2018]. Due to the complex multi-way coupling between the magnetosphere and ionosphere-thermosphere, it is necessary to evaluate the magnetosphere and ionosphere-thermosphere as a coupled system in order to have a comprehensive understanding of SAPS.

Empirical models have been widely used to explore the effects and driving mechanisms of SAPS. Goldstein et al. [2005] developed a magnetospheric model of SAPS parameterized by the Kp index, which was limited in that it could only capture the gross spatial and temporal characteristics of SAPS. Zheng et al. [2008] adopted an empirical ring current model to simulate SAPS and found that the ionospheric conductance trough is critical to the generation of large magnitude SAPS. Wang et al. [2012] incorporated an empirical SAPS model into the Thermosphere Ionosphere Electrodynamics General Circulation Model (TIEGCM) and investigated SAPS effects on the global ionosphere and thermosphere during a moderately geomagnetically active period. They found that SAPS can cause an increase in global

thermospheric temperature and changes in thermospheric composition. Although the empirically driven models can help us understand specific aspects of SAPS, they are inadequate to describe the dynamic evolution of SAPS under different geophysical conditions.

In recent years, global geospace models and coupled frameworks have been used to explore the generation of SAPS. Yu et al. [2015] used the Block-Adaptive Tree Solar-wind Roe Upwind Scheme (BATS-R-US) global magnetohydrodynamic (MHD) model coupled with the inner magnetospheric ring current model RAM-SCB to simulate the 17 March 2013 storm event. The SAPS velocities were underestimated and its location was more equatorward than that in actual observations. Raeder et al. [2016] used the Open Geospace General Circulation Model (OpenGGCM), Coupled Thermosphere Ionosphere Model (CTIM), and Rice Convection Model (RCM) to model the same event. The more consistent locations and velocity with observations were attributed to the inclusion of a self-consistent ionosphere/thermosphere model. Wiltberger et al. [2017] made use of the Lyon-Fedder-Mobarry (LFM) global MHD model coupled with RCM ring current model to simulate the same event. They found that the fast westward plasma flow in the subauroral region is mainly driven by the closure of Region 2 FAC, which results from the buildup of large inner magnetosphere pressure gradient and partial ring current during storm time. The inclusion of anomalous electron heating effects in the ionospheric conductance model could sometimes yield SAPS drift velocities that were more consistent with the observations. Therefore, it is further suggested that the inclusion of an ionosphere-thermosphere model with feedback effects from ionospheric plasma chemical processes and thermospheric neutral dynamics is needed to establish a system-level understanding of SAPS.

Due to the intimately coupled nature of the magnetosphere, ionosphere, and thermosphere, it is critical to self-consistently simulate the dynamical processes from solar wind-magnetosphere interaction to the upper atmosphere when modeling the generation and evolution of SAPS.

In this paper, we report the initial results from the CMIT model with ring current extension, namely the LFM-TIEGCM-RCM (LTR) model framework. This integrated model provides a first-principle representation of the solar wind, magnetosphere, ring current, ionosphere, and thermosphere coupling. SAPS generation, global structure and dynamic evolution, which typically can not be obtained from observations and statistical studies, are explored by simulating the 17 March 2013 great storm. This paper is organized as follows: Section 2 introduces the LTR model, and gives an overview of the solar wind driving conditions and system-level geospace responses during the storm event. Section 3 presents the analysis of the simulation results, including the identification of SAPS within the simulation results, comparison with the observational data, and a quantitative characterization of SAPS global structure and dynamic evolution. Section 4 discusses the implications of the model outputs and summarizes the findings of this simulation study.

4.2 Simulation Setup

4.2.1 LFM-TIEGCM-RCM

The LTR model is used in this study to investigate the geomagnetic storm that occurred on 17 March 2013. The integrated framework couples the LFM global MHD magnetosphere model [Lyon et al., 2004b], the TIEGCM global ionosphere/thermosphere model [Richmond et al., 1992, Roble et al., 1988], and the Rice Convection Model of the ring current [Toffoletto et al., 2003], via the Magnetosphere-Ionosphere Coupler/Solver (MIX) module [Merkin and Lyon, 2010b]. Historically, the LFM and TIEGCM were first coupled to establish the Coupled Magnetosphere Ionosphere Thermosphere (CMIT) model [Wang et al., 2004, Wiltberger et al., 2004]. The LFM and RCM were then coupled into the magnetosphere-ionosphere-ring

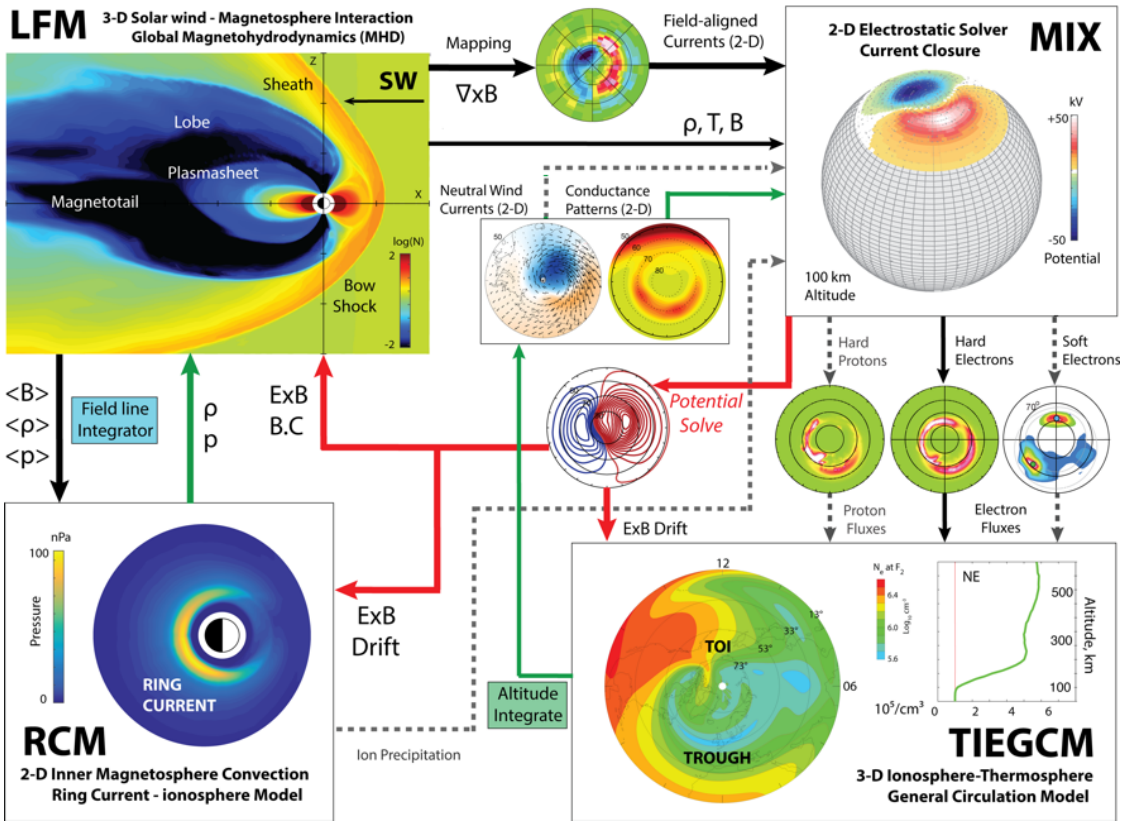

Figure 4.1: Flow chart of the coupled LFM-TIEGCM-RCM model.

current model [Pembroke et al., 2012]. The LFM-TIEGCM-RCM model has been recently developed to incorporate the RCM into the CMIT.

Figure 4.1 shows the flow chart of the coupling processes between the LFM, TIEGCM, and RCM. The LFM model solves ideal MHD equations for the interactions between the solar wind and the magnetosphere. Magnetic field and plasma information in the inner magnetosphere is passed from LFM to RCM for the calculation of the ring current distribution in RCM. The plasma density and pressure are then passed from RCM to LFM. Field-aligned currents are calculated at the inner boundary of LFM and mapped down to the MIX module together with the auroral precipitation which is determined from the plasma density and temperature [Fedder et al., 1995, Wiltberger et al., 2009]. The MIX coupler solves the ionospheric potential, and passes the auroral precipitation and electrostatic potential to

TIEGCM. The ionospheric and thermospheric circulation and electrodynamics are solved in TIEGCM, which returns the updated ionospheric conductance to MIX. More details about the coupling processes can be found in Lyon et al. [2004b], Merkin and Lyon [2010b], Pembroke et al. [2012], Wang et al. [2004], Wiltberger et al. [2004, 2017]. It should be pointed out that the coupled model incorporates three-way coupling among the magnetosphere, ring current, and ionosphere-thermosphere, which makes it feasible to investigate geospace from the solar wind to the altitude of the thermosphere with real-time and self-consistent downward driving and upward feedback. The connections represented with dashed lines are not yet implemented in this study, but will be implemented in the future.

In this study, the LFM model utilizes the quad resolution, that is, $106 \times 96 \times 128$ cells in the radial, meridional, and azimuthal directions, respectively. The MIX coupler is computed on a $1^\circ \times 1^\circ$ magnetic latitude and longitude grid. The TIEGCM utilizes a longitudinal and latitudinal resolution of 1.25°. The RCM utilizes 200 cells in latitude, 100 cells in longitude, 90 energy channels, and a dipole tilt. For the strong solar wind driving conditions considered here, we found it necessary to reduce the intervals of data exchange to 5 s between LFM and MIX, 10 s between LFM and RCM, and 10 s between TIEGCM and MIX in order to avoid numerical instability.

4.2.2 Solar wind conditions and systematic geospace responses

The 2013 St. Patrick's Day storm is a famous event that has been surveyed with different models and observational data [e.g., Raeder et al., 2016, Wiltberger et al., 2017, Yu et al., 2015, Zhang et al., 2017b]. The solar wind and IMF conditions for 17 March 2013 are shown in Figure 4.2 (a-d). The data were obtained from the OMNI database and used to drive the LTR model. A coronal mass ejection (CME) arrived at the Earth at 05:55 UT and triggered

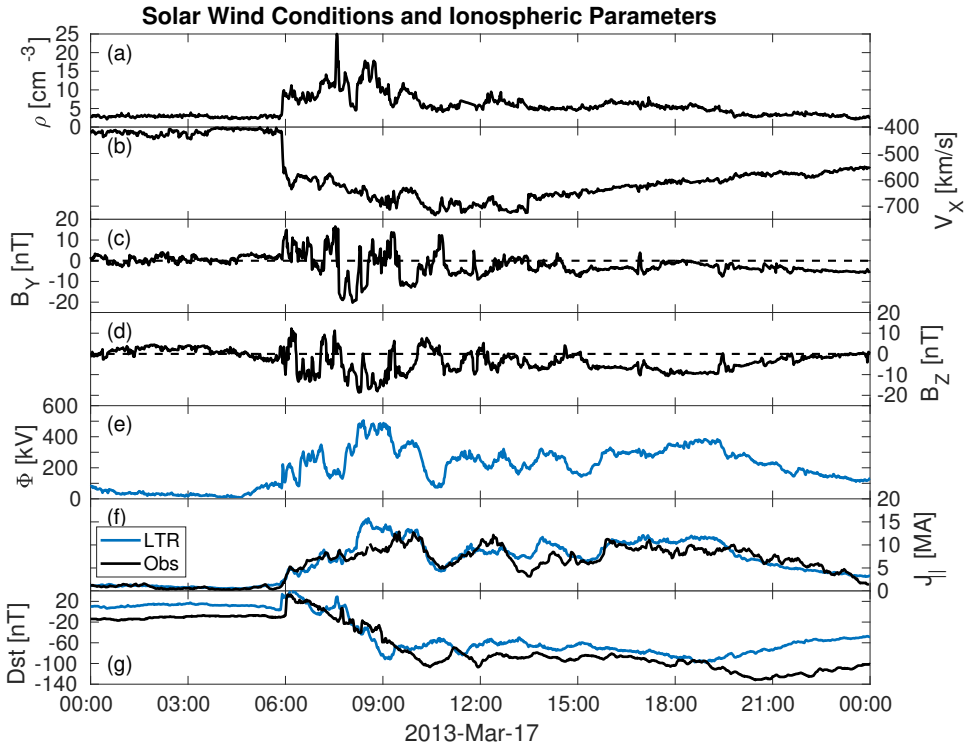

Figure 4.2: Solar wind conditions from the OMNI database and ionospheric parameters from LTR simulation results and observations for 17 Mar 2013. (a) Solar wind density. (b) Solar wind velocity V_X. (c-d) IMF B_Y and B_Z in GSM. (e) Simulation results of cross polar cap potential. (f) Total field-aligned current that flows into the ionosphere obtained from the model output (blue) and AMPERE data (black). (g) Dst index obtained from model output (blue) and CDAWeb database (black).

a great geomagnetic storm over the rest of the day. The solar wind density increased to above 10 cm^{-3}, solar wind speed reached -700 km/s, and IMF B_Z reached -20 nT after the CME arrived. The Dst index decreased to below -100 nT in the next 4 to 5 hours and maintained a low level for the rest of that day. The strongly disturbed IMF and solar wind conditions returned to pre-disturbed conditions by the end of the day.

Figure 4.2 (e-g) shows the overall geospace response by presenting the time series of the cross polar cap potential (CPCP) and the measured/simulated total FAC in the northern hemisphere, and the simulated Dst index. The CPCP is calculated as the difference between the max and min of the ionospheric potential (Figure 4.2e). The total FAC is integrated over

the FAC density that flows into the ionosphere (Figure 4.2f). The AMPERE measurements of integrated downward FAC in the northern hemisphere are shown with the black curve for comparison. The simulated Dst index is determined from the magnetospheric field-aligned currents and the ionospheric horizontal currents by calculating the ground magnetic field perturbations with the Biot-Savart method. The observed Dst index is shown in black and obtained from the CDAWeb OMNI database. The comparison of Dst and total FAC with observational data demonstrates that the LTR model could yield systematically consistent results of the geospace response to the solar wind driving conditions during the 2013 St Patrick's Day Storm although there are still some discrepancies implying the possibility of missing physics.

4.3 SAPS Simulation Results

4.3.1 SAPS identification and comparison with DMSP observations

Figure 4.3 shows the SAPS identified in the simulation results and comparison with those observed by the DMSP F18 satellite during three 10-minute intervals: 10:12 - 10:22 UT, 11:53 - 12:03 UT, and 15:17 - 15:27 UT. The DMSP F18 measurements are shown in black. Figure 4.3 (a-c) shows electron precipitation energy flux (EnFlux). The simulated precipitation energy fluxes are shown in blue, which are sampled from the MIX outputs along the trajectory of the DMSP satellite. Note the DMSP satellite was flying poleward during the three intervals shown here. The electron precipitation energy flux profiles are shown to represent the auroral region. The equatorward boundary of auroral electron precipitation is indicated by the vertical dashed lines, which is determined where the electron precipitation energy flux drops

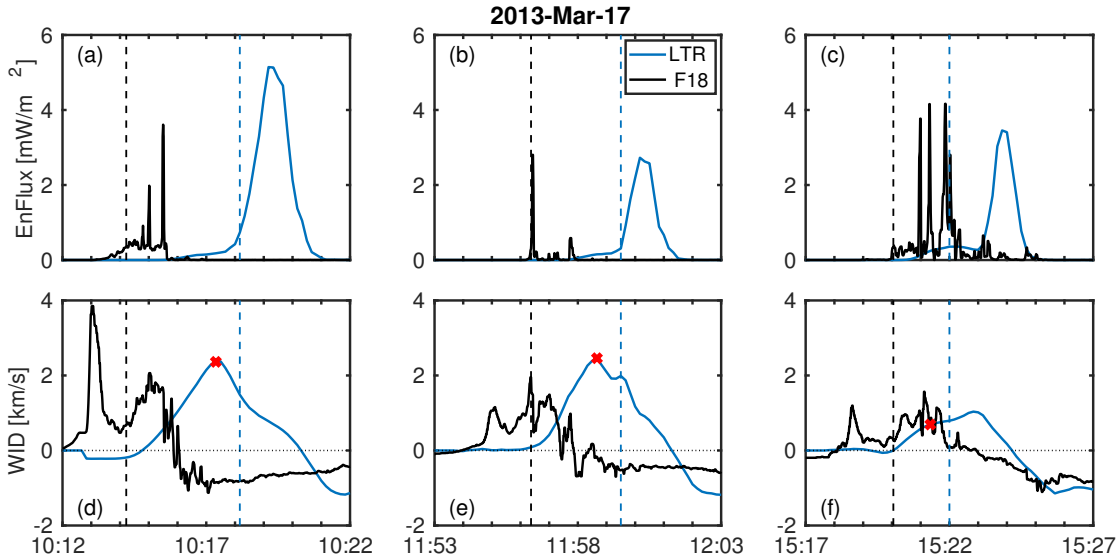

Figure 4.3: Comparison of DMSP F18 measurements and the LTR simulation results of electron precipitation energy flux and westward ion drifts (WID) during three DMSP F18 crossings of the auroral zone: (left) 10:12 - 10:22 UT, (center) 11:53 - 12:03 UT, (right) 15:17 - 15:27 UT. (a-c) Precipitating electron energy flux (EnFlux) measured by the DMSP F18 (black) and sampled from the LTR simulation results (blue). (d-f) WID from DMSP measurements (black) and LTR simulations (blue). The simulated electron energy flux and WID shown here are sampled from the MIX outputs along the trajectories of the DMSP F18 satellite during the crossings. The vertical dashed lines correspond to where the EnFlux drops to 0.1 of the peak value during each interval, which are used to indicate the equatorward boundary of auroral electron precipitation. The red crosses in (d-f) indicate the peaks of subauroral WID.

to 0.1 of the peak value. Figure 4.3 (d-f) shows the westward ion drift (WID) velocity from the DMSP measurements and simulation results. It can be seen from the black curves that before the F18 satellite entered the auroral zone, additional westward ion flow channels were detected in the subauroral area. The ion drift velocities sampled in the simulation results are plotted in blue, which also show a substantial flow channel at somewhat lower latitudes than the equatorward boundary of auroral electron precipitation. These subauroral westward convections are interpreted as the definitive feature of SAPS [Foster and Burke, 2002, Koustov et al., 2008]. It should be pointed out that while the simulation results do not always show an unambiguous secondary peak of WID, the drift velocity profiles do level off

before dropping, which imply the existence of a separate subauroral convection flow channel. The peaks of SAPS flow channels in the simulation results are indicated by the red crosses in Figure 4.3 (d-f). It is also noteworthy that the auroral region and SAPS channels are detected at somewhat later times in the simulation results compared to those in the DMSP F18 data, which imply that the auroral boundary is at a higher latitude in the model.

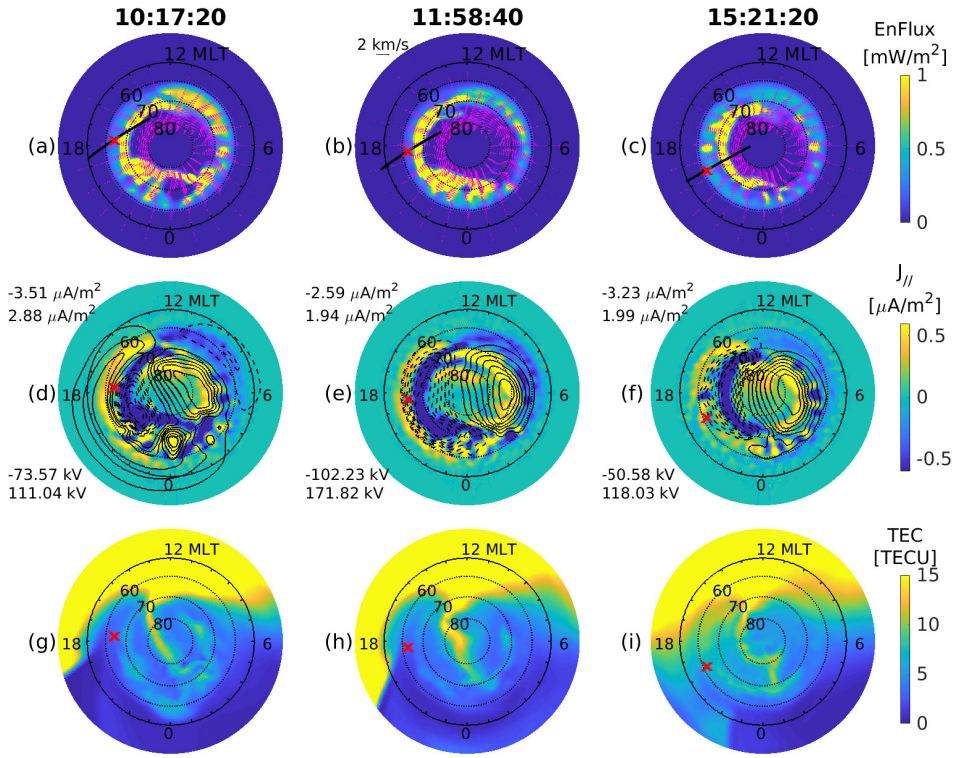

Figure 4.4: Simulation results of the ionospheric states at three UTs when SAPS peak velocity are identified by the virtual DMSP F18 satellite. (a-c) MIX outputs of electron precipitation energy flux (EnFlux) into the ionosphere and zonal ion drift velocities (black arrows). The zonal drifts are sampled at 24 MLT hours from magnetic latitude of 40° to 80° in every 1°. The thick black curves show the trajectories of the virtual DMSP F18 during the 10 min intervals shown in Figure 4.3. The red crosses indicate the positions of the virtual satellite at the times shown here, which also correspond to the red crosses in Figure 4.3. (d-f) MIX outputs of FAC density ($J_{//}$, background color) and electrostatic potential (ϕ, black contours) in the northern hemisphere ionosphere. Positive FAC flows into the ionosphere. Positive potential is shown with the solid lines and negative with the dashed. The numbers on the left are the min and max of $J_{//}$ (top) and ϕ (bottom). (g-i) TIEGCM outputs of ionospheric TEC.

In order to further illustrate the SAPS structure, we show the ionospheric states at the times when SAPS peak velocities are detected by the virtual DMSP F18 satellite analyzed in Figure 4.3. Figure 4.4 shows the simulation results at 10:17:20 UT, 11:58:40 UT, and 15:21:20 UT in the left, center, and right column, respectively, which correspond to the times indicated by the red crosses in Figure 4.3 (d-f). Figure 4.4 (a-c) show the MIX outputs of electron precipitation energy flux (EnFlux) into the ionosphere using the same color bar. The bright color represents the auroral region, which spans equatorward to about 65° magnetic latitude on the duskside at 10:17:20 UT and 11:58:40 UT, and extends poleward to about 70° at 15:21:20 UT. The plasma zonal drift velocity in the ionosphere is presented with the magenta arrows. The drift velocity is calculated from $\vec{E} \times \vec{B}$, where $\vec{E}$ is derived from MIX outputs of the ionospheric electrostatic potential and $\vec{B}$ is assumed to be a dipole geomagnetic field. The convection velocities are evaluated at 24 magnetic local time (MLT) hours and every 1° from 40° to 80° magnetic latitude. The scale length is shown on the top left of the middle panel for 2 km/s. The velocity vectors show the westward drift channel around 60° magnetic latitude on the duskside, which is below the equatorward boundary of the electron auroral precipitation. The DMSP trajectories during the three intervals in Figure 4.3 are shown with the thick black curves. The red crosses on the trajectories indicate the positions of the virtual satellite at the current time, namely when the SAPS peak velocity is identified. The two-dimensional plots of auroral electron precipitation and ionospheric convection provide a straightforward view of the subauroral flow channel, which spans from the duskside to midnight. The magnetic latitude of the SAPS flow channel is from 65° to $< 60°$, which is higher than that found in the observational data [Foster and Vo, 2002]. This displacement likely results from the poleward shifted distribution of the upward Region 1 FAC in LFM simulations [Zhang et al., 2011].

Figure 4.4 (d-f) show the MIX outputs of ionospheric FAC density $J_{//}$ and electrostatic

potential ϕ in the northern hemisphere. The FAC density is indicated by the same color bar where positive stands for downward current flowing into the ionosphere. The electrostatic potential is shown with black contour lines, where solid lines stand for positive potential and dashed for negative. The FAC density range is shown in the top left and the potential range is shown in the bottom left of each panel. The locations where SAPS peak is detected by the virtual satellite are shown by the red crosses. It can be seen that the electron auroral precipitation is collocated with the upward FAC on the duskside which is associated with Region 1 currents, while SAPS are collocated with the downward FAC, which is associated with Region 2 currents on the duskside.

Figure 4.4 (g-i) show the TIEGCM outputs of ionospheric TEC in the northern hemisphere. Note the color bar is intentionally saturated to highlight the TEC variation on the duskside where SAPS peak velocities are identified. The TEC at the SAPS peak location is lower compared to that at higher or lower latitudes. The trough-like structure appears to be consistent with the enhanced poleward electric field that drives the SAPS. The TEC plots also show a poleward extension in the dayside high latitude, which is identified as the tongue of ionization (TOI). The collocation between the SAPS and Region 2 FAC as well as the low ionospheric TEC is in agreement with the statistical study based on DMSP data [He et al., 2018], and supports the mechanism that SAPS are generated as Region 2 FAC flows into the low conductance ionospheric region. The ionospheric conductance although not shown here, does show that the conductance is relatively lower at the location where SAPS were identified.

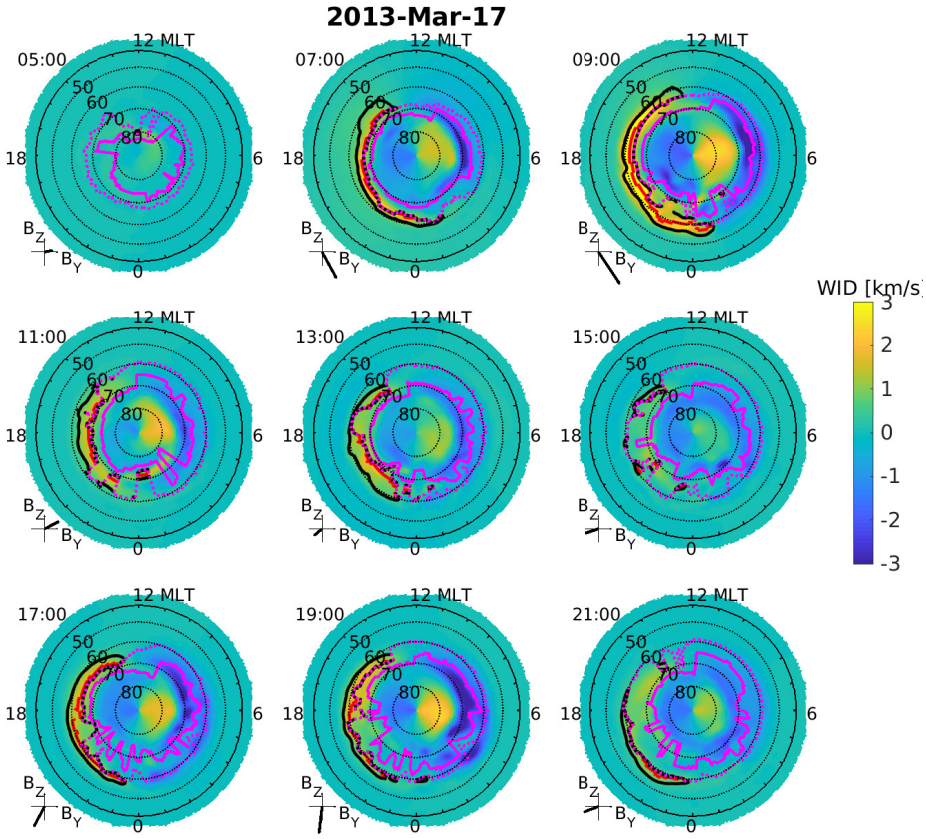

Figure 4.5: Distribution of ionospheric zonal drift velocity at nine UTs from 05:00 UT to 21:00 UT. Westward is positive. Auroral precipitation peaks at each MLT are indicated by the solid magenta lines. Equatorward boundaries of the electron precipitation oval are indicated by the dotted magenta lines. SAPS channels are indicated by the thick black lines. SAPS peaks are shown with the red lines.

4.3.2 SAPS global structure

Having shown that the coupled LTR model can crudely reproduce the definitive observational features and drivers of SAPS, we can characterize the global structure of SAPS with the simulation results. Figure 4.5 shows the global distribution of ion zonal drift velocity in the ionosphere from 05:00 UT to 21:00 UT at every two hours. Here the ion drift velocity is derived from the MIX outputs with the same method used for Figure 4.4 (a-c). The positive velocity is westward. The SAPS region is quantitatively determined by comparing

the electron auroral precipitation and ionospheric convection. We begin by identifying the equatorward boundary of the electron aurora oval with the MIX outputs of electron precipitation energy flux. At each MLT, the latitudinal peak of electron precipitation energy flux is first found. The electron precipitation peaks of all MLTs are shown by the solid magenta curves. The electron auroral equatorward boundary at each MLT is then determined as the latitude at which the electron precipitation energy flux drops to 0.1 of the precipitation peak of that MLT. The electron auroral equatorward boundary is shown with the dotted magenta curve. SAPS are identified at each MLT if there is a substantial westward ion drift, namely greater than 500 m/s [Foster and Vo, 2002], found below the latitude of the electron auroral equatorward boundary. The SAPS are marked with two thick black curves which delimit the full width half maximum of the SAPS convection channel in the subauroral region. Within the SAPS channel, the latitude Λ at which the latitudinal peak velocity V_S is identified is shown with the red curve. The IMF B_Y and B_Z in GSM are shown at the bottom left of each panel in Figure 4.5. The B_Y and B_Z axes range from -5 nT to 5 nT. The IMF is obtained from the OMNI database with 20 min shift in time, which is roughly the time needed to establish the ionospheric convection [Clauer and Friis-Christensen, 1988].

At 05:00 UT before the storm started, the IMF was weakly northward and there is hardly any SAPS detected. The IMF turned strongly southward about one hour after the storm onset at 07:00 UT. A SAPS channel appeared in the duskside subauroral region which spans from early afternoon to post-midnight. The simulation shows that the latitude of the SAPS decreases with MLT. The latitudinal width of the SAPS also decreases with MLT, forming the so-called wedge-shape structure. This spatial distribution of SAPS is consistent with the statistically average features [Foster and Vo, 2002] and the recently reported observation of SAPS in the main phase [He et al., 2018]. By 09:00 UT when the IMF B_Z was even stronger southward, the SAPS had broadened both longitudinally and latitudinally with an

overall equatorward expansion. The magnitude of SAPS velocity is also enhanced compared to 07:00 UT. In the next few hours until 15:00 UT, the IMF was not as strongly southward and the SAPS channel shrunk to a narrower MLT ranging from pre-dusk to pre-midnight. The SAPS channel also became longitudinally discontinuous when the driving condition is weaker. From 17:00 UT to 19:00 UT, another period of southward IMF was impacting the magnetosphere and SAPS channel expanded, and the SAPS channel expands to below 60° magnetic latitude and approached postnoon. The solar wind and IMF conditions returned to typical values of quiet time by 21:00 UT, when SAPS were weak and mostly localized between dusk and midnight.

4.3.3 SAPS dynamic evolution

With the SAPS global structures quantitatively characterized at different times as shown in Figure 4.5, we now further explore the dynamic evolution of SAPS by examining the dependence of SAPS parameters on the IMF B_Z and storm activity level. SAPS are treated as a two-dimensional structure varying with MLT and magnetic latitude. We use the latitudinal peak of SAPS velocity at each MLT (V_S) to characterize the magnitude of SAPS. V_S at all MLT during the entire day is plotted in Figure 4.6 (a). Note that the V_S distribution shows that SAPS are mostly detected from postnoon to post-midnight. Almost no SAPS are identified between 02:00 UT to 05:00 UT when IMF B_Z was northward with small magnitudes. The mean value of V_S over all MLTs is shown in Figure 4.6 (b). The largest V_S occurred between $\sim$ 07 : 30 and 10:00 UT when IMF B_Z was southward with large magnitudes. SAPS location is characterized with the latitude Λ at which V_S is detected. The temporal variations of the MLT distribution of Λ and its longitudinal mean $\overline{\Lambda}$ are shown in 4.6 (c-d). The latitudinal size of SAPS $\delta\Lambda$ is characterized with the full width half maximum of the latitudinal profile of SAPS velocity at each MLT. The $\delta\Lambda$ and $\overline{\delta\Lambda}$ are shown

in 4.6 (e-f). The Dst index and IMF B_Z are shown in Figure 4.6(e-f), respectively.

SAPS signatures are detected after the beginning of the day, although the SAPS magnitude from 00:00 UT to 02:00 UT was only a few hundred m/s. The SAPS were confined to a few MLT hours near dusk at $\sim 70°$ magnetic latitude. The SAPS latitudinal width is only $1° - 2°$. These SAPS signatures are attributed to the southward IMF during the last UT hour of March 16 2013. They then gradually shrink to high latitude and disappear over the period of northward IMF until 05:00 UT.

SAPS are detected again when the IMF turned southward even before the storm onset at 05:55 UT. The peak magnitude increases to more than 3 km/s by 09:00 UT during the main phase of the storm (Figure 4.6 (a)). It can be seen from Figure 4.6 (b) that SAPS initiate at $\sim$ 15 MLT before the storm onset with limited longitudinal coverage. But the strongest SAPS magnitude occurred a bit later than 18 MLT after the storm onset. There is a brief interruption of SAPS growth around 07:30 UT, which is attributed to the northward turning of IMF. SAPS magnitude is drastically strengthened at all duskside MLTs from 07:30 UT to 10:30 UT. The mean latitude in Figure 4.6 (c) shows that SAPS are overall expanding equatorward in the main phase. Figure 4.6 (d) indicates that near the storm onset, SAPS latitude is decreasing with MLT from over 70° to $\sim 60°$. The mean latitudinal width in Figure 4.6 (e) shows that the SAPS channel is broadening during the main phase. Specifically, the latitudinal width is larger near noon and becomes narrower toward midnight, forming the so-called wedge shape, as shown in Figure 4.6 (f) from 06:30 UT to 07:10 UT.

In the recovery phase, the SAPS magnitude starts to gradually decrease after 09:00 UT. However, the mean latitude of SAPS stays around 60° magnetic latitude and the mean width maintains 4° to 6° for about 10 hours instead of recovering to pre-storm values instantly. A rebound of the SAPS magnitude is seen from 09:30 UT to 10:00 UT, which is correlated with the southward turning of IMF following the brief northward period after 09:00 UT. It

is interesting to note that an inverse wedge-shape is formed from 08:40 UT to 09:20 UT and from 09:40 UT to 10:20 UT, when the SAPS channel is wider near midnight and narrower in the postnoon sector. The inverse wedge-shape appears to be associated with the weakening of southward IMF. The SAPS magnitude resumes decreasing after 10:00 UT when the IMF becomes northward again. The dip around 15:00 UT in SAPS magnitude and width and poleward motion is also accompanied by the weakening of the southward IMF.

From 15:30 UT to 19:30 UT, the IMF is continuously southward. The overall magnitude of SAPS is below 2 km/s. The SAPS channel is widest near the dusk and is narrower toward the midnight and postnoon, forming a crescent shape distribution, as shown in Figure 4.5 bottom row. The SAPS magnitude and width decreases continuously after 19:00 UT when the Dst is also recovering with both the decreasing IMF B_Z magnitude and solar wind velocity. Besides the variations on the scale of hours, it is also visible that the SAPS magnitude and structure profiles show more fluctuating behaviors compared to that of IMF B_Z, which implies that the SAPS are very dynamic structures associated with the magnetosphere-ionosphere-thermosphere coupling.

4.4 Discussion and Future Work

In this study, the Coupled Magnetosphere-Ionosphere-Thermosphere model with Ring Current extension is used to investigate the SAPS global structure and dynamic evolution during the 2013 March 17 storm event. SAPS not only involve processes in different geospace domains, including the magnetosphere, ring current, ionosphere, and thermosphere, but also require distinct characterizations of plasma, including MHD description and kinetic treatments of the ions and electrons. The LFM-TIEGCM-RCM represents a state-of-the-art integrated geospace model that can self-consistently model the magnetosphere, ring current, ionosphere

and thermosphere, and the dynamic coupling between these regimes. The simulated total ionospheric FAC and Dst index are found to be very close to available observational data, indicating reasonably consistent system-level responses in the modeling results. The finite discrepancy between the simulation results and the measured data imply the possibility of missing physics which should be improved in the future. The analysis of subauroral convection further shows good agreement with the DMSP F18 measurements, demonstrating that the coupled LTR model is able to capture the fundamental structure and generation physics of SAPS.

The SAPS magnitude and spatial coverage are quantitatively characterized and their dependence on IMF B_Z are analyzed. We found a persistent flow channel in the subauroral region which is identified as SAPS. By comparing with the ionospheric FAC density and TEC map, it is found that the SAPS channel is collocated with the Region 2 FAC on the duskside and a trough-like structure in the TEC map. This correlation supports the driving mechanism proposed in Anderson et al. [1993] in which a fraction of the downward Region 2 FAC flows into the low ionospheric conductance region at subauroral latitudes. A strong poleward electric field is thus required to maintain the current continuity which drives the enhanced westward ion drift. This scenario is also supported by recent multi-satellite analysis of SAPS [He et al., 2018].

It should be pointed out that the SAPS found in the model is at a higher latitude compared to that observed by the DMSP satellite. This displacement is likely a result of ring current effects. Wiltberger et al. [2017] has shown that the dipole magnetic field used in LFM-RCM is relatively underinflated compared to the TS07d empirical magnetic field model [Tsyganenko and Sitnov, 2007]. As a result, the inner magnetosphere pressure peak is more outward thus yields a more poleward Region 2 FAC. The ionospheric outflow has also been found to play an important role in generating a more realistic magnetic field topology [Brambles et al.,

2013].Therefore, incorporating an ionospheric outflow model, such as the Ionosphere/Polar Wind Model (IPWM), into the LTR model for ionospheric outflow effects may produce a more reasonable distribution of inner magnetospheric pressure and more consistent SAPS locations with observations [Varney et al., 2015].

The SAPS channel is less separated from the auroral convection compared with that observed by the DMSP satellite. This may be because the auroral precipitation model in the framework lacks the diffuse aurora, which is the dominant provider of precipitation energy flux [Newell et al., 2009]. Efforts are ongoing to include the diffuse precipitation and ion precipitation into the model.

The global structure of SAPS can be quantitatively determined with the model results. The SAPS wedge-shaped flow channel is observed in the beginning of the main phase (Figure 4.5, top middle panel). An inverse wedge shape is also seen when the southward IMF is weakening (Figure 4.5, top right panel). The SAPS flow channel shows crescent distribution in the late recovery phase. The westward drift flow sometimes becomes discontinuous in the recovery phase. The large variations with longitude, latitude, and in magnitude suggest that SAPS are very dynamic structures and are strongly responsive to the southward IMF. The rapid evolution of SAPS may be attributed to the auroral streamers which can enhance the ring current pressure [Gallardo-Lacourt et al., 2017]. The correlation coefficient between the SAPS parameters and IMF B_Z and the Dst index are shown in Table 1. Here B_Z is shifted by 20 min for correlation analysis considering the time delay of propagation effects from solar wind to the ionosphere. While the SAPS structure has been shown to be qualitatively consistent with southward IMF, the quantitative correlation coefficients are generally below 0.8, which could be due to the rapid oscillations of SAPS structure parameters. The connections between SAPS evolution and southward IMF in this event simulation are consistent with the statistical results of He et al. [2017]. It is inferred that the enhancement of ring

Table 4.1: Correlation coefficients between SAPS parameters and IMF B_Z and Dst index.

	$\overline{V_S}$	$\overline{\Lambda}$	$\overline{\delta\Lambda}$
Dst	-0.34	0.77	-0.55
B_Z	-0.57	0.54	-0.47

current during southward IMF contributes to the strengthening of Region 2 FAC that flows into the subauroral region and facilitates the growth of SAPS.

In this study, SAPS during the 2013 St. Patrick's Day storm are investigated with the coupled magnetosphere-ring current-ionosphere-thermosphere model. The key features of SAPS and their driving processes are captured by the model and show good consistency with observational data. SAPS are collocated with the Region 2 FAC on the duskside and TEC trough in the ionosphere. The Region 2 FAC flowing into the low conductance region in the subauroral latitude results in the strong poleward electric field that drives the enhanced SAPS flow. The global structure and evolution of SAPS are quantitatively characterized using the modeling results. SAPS evolution involves latitudinal and longitudinal structure, and drift velocity variations. SAPS structure is found to be very dynamic and sensitive to IMF B_Z such that the SAPS magnitude, location and latitudinal width are correlated with the strength of the southward IMF. It is suggested that SAPS evolution is closely related to storm activity. This is the first time that the high resolution LFM, TIEGCM, and RCM models have been coupled together to examine storm-time behavior which is necessary to explore the mesoscale processes like SAPS. To better understand the coupling mechanism of SAPS, we will in the future work look at the SAPS influences on the ionosphere-thermosphere and how the subauroral dynamics feedback to the inner magnetosphere. Improved models of the ring current and auroral precipitation are required.

4.5 Acknowledgement

This work is funded by NASA MAG16_2-0050 and the Visitor Program of High Altitude Observatory of National Center for Atmospheric Research. This work is also supported by NASA grants 80NSSC17K0013, NNX17AI42G, NNX15AB83G and NNX14AE06G. The National Center for Atmospheric Research is sponsored by the National Science Foundation. We acknowledge use of NASA/GSFC's Space Physics Data Facility's CDAWeb service, and OMNI data. We acknowledge high-performance computing support from Cheyenne (doi:10.5065/D6RX99HX) provided by NCAR's Computational and Information Systems Laboratory, sponsored by the National Science Foundation. Dong Lin would like to thank Dr. Michael Wiltberger for his help with testing the coupled model, and thank Dr. William Lotko for his help with revising the manuscript. Simulation data, simulation codes, and analysis routines are being preserved on the NCAR High Performance Storage System and will be made available upon written request to the lead author (ldong7@vt.edu).

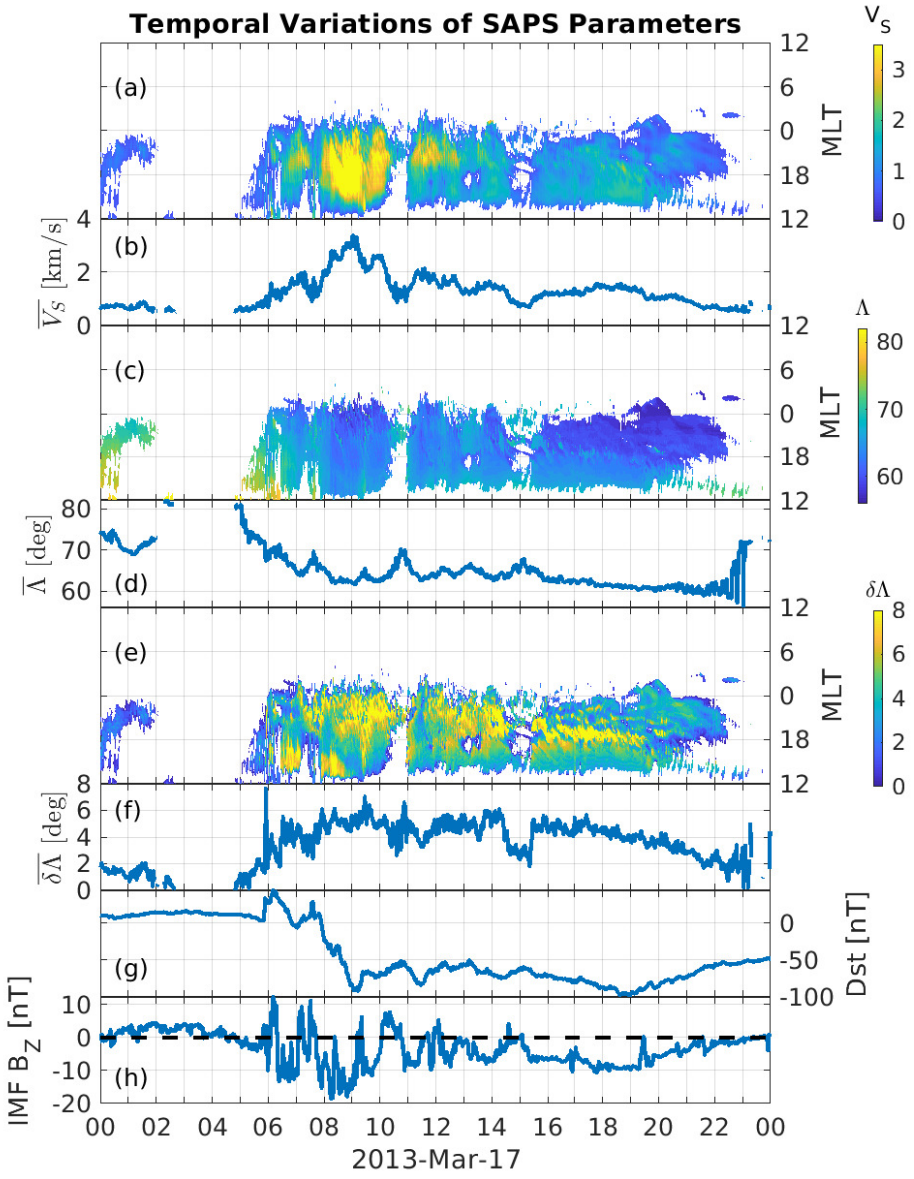

Figure 4.6: Temporal variations of SAPS (a) latitudinal peak drift velocity V_S at all MLT; (b) longitudinal mean of V_S; (c) the latitude Λ at which V_S is detected; (d) longitudinal mean of Λ. (e) latitudinal width $\delta\Lambda$ at all MLT; (f) longitudinal mean of $\delta\Lambda$; (g) Dst index; (h) IMF B_Z in GSM.

Chapter 5

Conclusion and Future Work

5.1 Multiscale Computational Study

In this dissertation, solar wind-magnetosphere-ionosphere coupling has been investigated with three different computational models. Three important aspects of SW-M-I coupling have been examined corresponding to three representative spatial/temporal scales in space plasma physics.

5.1.1 PIC Model and Kinetic Scale Dynamics

The kinetic scale physics during the solar wind-magnetosphere interaction was investigated with a particle-in-cell (PIC) model (Chapter 2). The PIC modeling focused on the energy conversion and wave emission at the magnetotail dipolarization front (DF) due to strong velocity inhomogeneity. The generation of the DF is due to the global compression effects of the magnetotail reconnection, where a significant amount of electromagnetic energy is converted into kinetic and thermal energy of the magnetotail plasma. The consequent energetic particles and plasma waves can further propagate into the inner magnetosphere and change the energy budget in near Earth space.

The PIC simulations reveal that velocity shear driven electron-ion-hybrid (EIH) instability can effectively relax the sharp DF boundary layer. The wave excitation is an important

intermediate process of energy conversion after the energy unloading in the magnetotail reconnection. The EIH mechanism is suggested to account for the lower hybrid waves that are often observed at the magnetotail DF and can also explain why sharp velocity shears are not very often detected at the DFs. The velocity inhomogeneity driven instability is an alternative mechanism of energy dissipation and wave generation in addition to those driven by the pressure gradient and anisotropies in the velocity distribution function.

The excitation of the EIH instability requires the scale length of the DF layer to be smaller than the ion gyroradius, the time scale to be on the electron/ion gyro period (lower hybrid time), and an ambipolar electric field due to the separation of electrons and ions. These kinetic scale features could not be resolved in a magnetohydrodynamic (MHD) model. A PIC model is therefore indispensable in order to understand the microscopic dynamics of DFs on the ion/electron scale.

5.1.2 LFM Model and MHD Scale Dynamics

The MHD scale physics during the magnetosphere-ionosphere interaction was investigated with the LFM global magnetohydrodynamic (MHD) model (Chapter 3). The MHD modeling focuses on the electrodynamic response of the ionosphere to solar wind driving. The ionospheric electric field is mapped down from that in the solar wind and drives the convection of the ionospheric plasma in the polar cap. The cross polar cap potential (CPCP) measures the difference between the maximum and minimum of the electrostatic potential associated with the ionospheric convection, thus representing the efficiency of the coupling between the solar wind and the magnetosphere. The ionospheric convection on the other hand is imposed on the atmosphere at a lower altitude, therefore affecting the atmospheric dynamics which is more closely related to human activity on the ground.

With the LFM global MHD model, it was demonstrated that the solar wind density plays an important role in the CPCP response to the solar wind electric field. When the driving condition is very strong, the CPCP remains linear with the solar wind electric field if the solar wind density is high enough. The transition between linear and nonlinear responses can be explained by the competition between the plasma pressure and the magnetic pressure, as stated in Lopez's magnetosheath force balance theory.

The MHD model is thus a useful tool for the study of the CPCP response to the driving electric field in the solar wind, which is essentially a global MHD scale process. On the other hand, it is prohibitively expensive to run a global PIC model to study this problem. The global model makes it feasible to directly evaluate the variation of the CPCP, which could only be inferred from a limited number of measurements in observational analysis. The global model also makes it possible to do controlled experiments to explore the influence of specific variables.

5.1.3 LTR Integrated Framework and Geospace System Scale Dynamics

The system scale dynamics in the coupled solar wind-magnetosphere-ionosphere was investigated with the LFM-TIEGCM-RCM (LTR) integrated framework of geospace models (Chapter 4). The coupled model was used to explore the subauroral polarization streams (SAPS), which is the enhanced subauroral convection driven by a strong poleward electric field in the sub-auroral ionosphere. SAPS have been shown to be associated with the injection of energetic particles in the inner magnetosphere, trough in the ionospheric total electron content (TEC), and thermospheric heating and zonal wind enhancement.

The LTR model framework has incorporated the solar wind-magnetosphere model, ring cur-

rent model, and ionosphere-thermosphere model. The coupled model was driven by the realistic solar wind/IMF conditions during the March 17 2013 storm. The simulation results enable analysis of the global structures and dynamic evolution of the SAPS and their correlation with the IMF conditions and Dst index.

SAPS is a manifestation of both MHD and non-MHD processes in the solar wind-magnetosphere-ionosphere system. The solar wind-magnetosphere coupling can be resolved with the global MHD model but the ring current has significant influence on the inner magnetosphere pressure and the Region 2 field-aligned currents, which requires solving the transport equations of energetic particles. The ionosphere-thermosphere contains both charged particles and neutral components. Its responses to the solar wind driving field and precipitation from the magnetosphere determine the generation and evolution of the SAPS. While individual models or empirical models can show some detailed properties of SAPS, the first-principle representation and global/dynamic evolution of SAPS need to be investigated with the integrated model framework.

5.1.4 Summary of Contributions

To summarize, it has been found in this study that (1) the velocity inhomogeneity at the magnetotail dipolarization front could drive wave emission and affect the energy conversion there, which has influences on the kinetic scale dynamics during the SW-M-I coupling; (2) the solar wind density could affect the ionospheric cross polar cap potential especially when the solar wind electric field is very large, which alters the MHD scale response of the ionosphere to the solar wind-magnetosphere forcing; (3) the subauroral polarization streams are process that involve both MHD and non-MHD dynamics in different geospace regions, which represent the complicated connections and interactions during with SW-M-I coupling.

Basically, different geospatial regions are characterized by distinct plasma properties that require fundamentally different descriptions. Within the same geospatial region, physics occurring on contrasting spatial and temporal scales could both affect the conversion of energy and transport of plasma. In order to fully understand the roles of global and local space plasma processes and develop forecasting capabilities for space weather effects, different models and integrated framework of their combinations are critical.

5.2 Future Geospace Modeling

Advances in numerical techniques have greatly improved the accuracy and robustness of individual models but cannot remove the intrinsic limitations of each model. In order to accommodate various physical models in the same study, attempts have been made to couple the different models.

5.2.1 Cross Scale Coupling

For the kinetic scale dynamics investigated in this dissertation, a somewhat simplified initial equilibrium was adopted for the PIC model. The DF was treated as a boundary layer with one-dimensional force balance which is derived from the observations of satellites crossing the DF. The magnetic profile did not contain a dip ahead of the DF for simplicity, which, however, has been found not rare in DF observations. While it is still technically impossible to get a self-consistently generated DF in the context of the global magnetosphere via fully kinetic particle models, a global MHD model may provide alternative means to specify more realistic initialization and boundary conditions for the DF.

Indeed, there have been both one-way and two-way coupled MHD and PIC models to explore

the particle dynamics in the context of solar wind-magnetosphere coupling. For example, Ashour-Abdalla et al. [2015] made use of a one-way coupled MHD-PIC model to study multiscale processes in the magnetotail reconnection. They used the global MHD model of the University of California, Los Angeles to provide realistic initial and boundary conditions for the PIC model, which is a two-dimensional version of the iPIC3D implicit PIC code. The PIC model then models the reconnection and evolution of the DF with self-consistent kinetic physics. It was found that multiple DFs are caused by the unsteady reconnection where the plasma acceleration is greater than that occurring near the X point.

Two-way coupled MHD-PIC models have also been realized recently. Chen et al. [2017] report global three-dimensional simulations using a two-way coupled MHD with embedded PIC models. The BATS-R-US model and the iPIC3D are coupled through the Space Weather Modeling Framework (SWMF). The PIC simulation domain covers the dayside reconnection region where the particle kinetics are important. It is noteworthy that despite the small time step in a PIC model, it can be comparable or even larger than the time step required by the Courant condition in an MHD model, which is because of the very high Alfvén speed near the magnetic pole. This study shows crater flux transfer event at the early stage of a flux rope formation, which represents kinetic phenomena found from the global simulation.

Kinetic scale dynamics could also provide important alterations for the processes occurring on a macroscopic scale. For example, in the MHD and LTR modeling in this dissertation, the ionospheric conductance is empirically determined with the extreme ultraviolet (EUV) solar radiation and the magnetospheric precipitation [Fedder et al., 1995, Wiltberger et al., 2009]. However, it has also been shown that the small-scale electrojet turbulence (ET) driven by the Farley-Buneman instability in the ionosphere could create conductivities that change the ionospheric current closure, Joule heating, and the convection pattern [e.g. Dimant and Oppenheim, 2011a,b].

Efforts have been made to incorporate the effects of kinetic instabilities into the ionospheric conductance model. Wiltberger et al. [2017] implemented the ET effects correction of ionospheric conductance when the ionospheric electric field exceeds a threshold value. They compared the LFM-RCM simulation results with and without the ET implementation and found that inclusion of the ET effects could yield more consistent total FAC and Dst index with observational data. It is further suggested that using an ionosphere-thermosphere model in which the ET effects can develop self-consistently would enable investigation of its global influence.

5.2.2 Cross Region Coupling

The LTR model framework adopted in this dissertation study is state-of-the-art in that it couples the solar wind-magnetosphere, ring current, and ionosphere-thermosphere into one model for the first time, which are characterized by different physical models, respectively. However, it can still be further improved considering the missing components in geospace environments.

The radiation belt has significant space weather effects because of the influences the energetic particles have on in-orbit satellites and the atmosphere. Modeling of the radiation belts has been challenging, and traditionally has been based on empirical parameters or test particle approaches. Empirical radiation belt models make use of the observation databases of magnetospheric plasma waves for the diffusion coefficients, which are generally assumed to be critically important for the dynamics of the energetic particles in the radiation belts. Well-known empirical radiation belt models include the Versatile Electron Radiation Belt (VERB) [Subbotin and Shprits, 2009], and the Dynamic Radiation Environment Assimilation Model (DREAM) [Reeves et al., 2012, Tu et al., 2013].

Test particle radiation belt models track the motion of seed charged particles in the electromagnetic field obtained from a global MHD model. They can be used to investigate where the energetic particles are energized, lost and transported. The more promising aspect of test particle radiation belt models compared to empirical models is that they are based on the global MHD model. The test particle radiation belt model is able to provide more dynamic characterization of the radiation belt and should be ready to be incorporated into the geospace models that have been coupled with global MHD models. Well-known test particle radiation belt models include the Conservative Hamiltonian Integrator for Magnetospheric Particles (CHIMP) model [Sorathia et al., 2018].

The atmosphere is more closely related to human activities on the ground but is subject to forcing and precipitation of the magnetosphere-ionosphere coupling dynamics. The National Center for Atmospheric Research (NCAR) Whole Atmosphere Community Climate Model with thermosphere and ionosphere extension (WACCM-X) is a whole atmosphere model that spans the altitude range from the ground to the ionosphere. Its most recent advances have incorporated the atmosphere-ionosphere interaction, including interactive chemistry, middle/low latitude electrodynamo, and empirical high latitude magnetospheric forcing, etc. [Liu et al., 2018b]. By replacing the empirical magnetospheric forcing at high latitudes with that directly obtained from a magnetospheric model, it is expected to yield a first-principle whole geospace model, which can represent the space weather effects from the solar wind through the magnetosphere and ionosphere and down to the atmosphere. The fully coupled whole geospace model will be beneficial to explore e.g., the dependence of the atmospheric dynamics and compositions on the solar wind-magnetosphere-ionosphere coupling, and energetic magnetospheric precipitation effects in the middle atmosphere and their feedback to the magnetosphere-ionosphere dynamics.

Bibliography

Wo E Amatucci, DN Walker, G Ganguli, JA Antoniades, DBJH Duncan, JH Bowles, V Gavrishchaka, and ME Koepke. Plasma response to strongly sheared flow. *Phys. Rev. Lett.*, 77(10):1978–1981, 1996. doi: 10.1103/PhysRevLett.77.1978.

PC Anderson, WB Hanson, RA Heelis, JD Craven, DN Baker, and LA Frank. A proposed production model of rapid subauroral ion drifts and their relationship to substorm evolution. *Journal of Geophysical Research: Space Physics*, 98(A4):6069–6078, 1993. doi: 10.1029/92JA01975.

PC Anderson, DL Carpenter, K Tsuruda, T Mukai, and FJ Rich. Multisatellite observations of rapid subauroral ion drifts (said). *Journal of Geophysical Research: Space Physics*, 106 (A12):29585–29599, 2001. doi: 10.1029/2001JA000128.

Maha Ashour-Abdalla, Giovanni Lapenta, Raymond J Walker, Mostafa El-Alaoui, and Haoming Liang. Multiscale study of electron energization during unsteady reconnection events. *Journal of Geophysical Research: Space Physics*, 120(6):4784–4799, 2015. doi: 10.1002/2014JA020316.

Charles K Birdsall and A Bruce Langdon. *Plasma physics via computer simulation*. CRC press, 2004.

OJ Brambles, W Lotko, B Zhang, J Ouellette, J Lyon, and Michael Wiltberger. The effects of ionospheric outflow on icme and sir driven sawtooth events. *Journal of Geophysical Research: Space Physics*, 118(10):6026–6041, 2013. doi: 10.1002/jgra.50522.

S Califf, X Li, RA Wolf, H Zhao, AN Jaynes, FD Wilder, DM Malaspina, and R Redmon.

Large-amplitude electric fields in the inner magnetosphere: Van allen probes observations of subauroral polarization streams. *Journal of Geophysical Research: Space Physics*, 121 (6):5294–5306, 2016. doi: 10.1002/2015JA022252.

Francis F Chen. *Introduction to plasma physics and controlled fusion*, volume 1. Springer, 1984. doi: 10.1007/978-3-319-22309-4.

Yuxi Chen, Gábor Tóth, Paul Cassak, Xianzhe Jia, Tamas I Gombosi, James A Slavin, Stefano Markidis, Ivy Bo Peng, Vania K Jordanova, and Michael G Henderson. Global three-dimensional simulation of earth's dayside reconnection using a two-way coupled magnetohydrodynamics with embedded particle-in-cell model: Initial results. *Journal of Geophysical Research: Space Physics*, 122(10):10–318, 2017. doi: 10.1002/2017JA024186.

C Robert Clauer and Eigil Friis-Christensen. High-latitude dayside electric fields and currents during strong northward interplanetary magnetic field: Observations and model simulation. *Journal of Geophysical Research: Space Physics*, 93(A4):2749–2757, 1988. doi: 10.1029/JA093iA04p02749.

C Robert Clauer, Zhonghua Xu, M Maimaiti, J Michael Ruohoneimi, Wayne Scales, Michael D Hartinger, Michael J Nicolls, Stephen Kaeppler, Frederick D Wilder, and Ramon E Lopez. Investigation of a rare event where the polar ionospheric reverse convection potential does not saturate during a period of extreme northward imf solar wind driving. *Journal of Geophysical Research: Space Physics*, 121(6):5422–5435, 2016. doi: 10.1002/2016JA022557.

LBN Clausen, JBH Baker, JM Ruohoniemi, RA Greenwald, EG Thomas, SG Shepherd, ER Talaat, WA Bristow, Y Zheng, AJ Coster, et al. Large-scale observations of a subauroral polarization stream by midlatitude superdarn radars: Instantaneous longitudinal

velocity variations. *Journal of Geophysical Research: Space Physics*, 117(A5), 2012. doi: 10.1029/2011JA017232.

SWH Cowley. Magnetosphere-ionosphere interactions: A tutorial review. *Magnetospheric Current Systems, Geophys. Monogr. Ser*, 118:91–106, 2000.

NU Crooker. Reverse convection. *Journal of Geophysical Research: Space Physics*, 97(A12): 19363–19372, 1992. doi: 10.1029/92JA01532.

Ioannis A Daglis, Richard M Thorne, Wolfgang Baumjohann, and Stefano Orsini. The terrestrial ring current: Origin, formation, and decay. *Reviews of Geophysics*, 37(4): 407–438, 1999. doi: 10.1029/1999RG900009.

William Daughton. Electromagnetic properties of the lower-hybrid drift instability in a thin current sheet. *Phys. Plasmas*, 10(8):3103–3119, 2003. doi: 10.1063/1.1594724.

YS Dimant and MM Oppenheim. Magnetosphere-ionosphere coupling through e region turbulence: 1. energy budget. *Journal of Geophysical Research: Space Physics*, 116(A9), 2011a. doi: 10.1029/2011JA016648.

YS Dimant and MM Oppenheim. Magnetosphere-ionosphere coupling through e region turbulence: 2. anomalous conductivities and frictional heating. *Journal of Geophysical Research: Space Physics*, 116(A9), 2011b. doi: 10.1029/2011JA016649.

A Divin, Yu V Khotyaintsev, Andris Vaivads, Mats André, Stefano Markidis, and Giovanni Lapenta. Evolution of the lower hybrid drift instability at reconnection jet front. *J. Geophys. Res.: Space Physics*, 120(4):2675–2690, 2015a. doi: 10.1002/2014JA020503.

Andrey Divin, Yu V Khotyaintsev, Andris Vaivads, and Mats André. Lower hybrid drift instability at a dipolarization front. *J. Geophys. Res.: Space Physics*, 120(2):1124–1132, 2015b. doi: 10.1002/2014JA020528.

Ami M DuBois, Edward Thomas, William E Amatucci, and Gurudas Ganguli. Experimental characterization of broadband electrostatic noise due to plasma compression. *J. Geophys. Res.: Space Physics*, 119(7):5624–5637, 2014. doi: 10.1002/2014JA020198.

James W Dungey. Interplanetary magnetic field and the auroral zones. *Physical Review Letters*, 6(2):47, 1961. doi: 10.1103/PhysRevLett.6.47.

Y Ebihara, N Nishitani, T Kikuchi, T Ogawa, K Hosokawa, M-C Fok, and MF Thomsen. Dynamical property of storm time subauroral rapid flows as a manifestation of complex structures of the plasma pressure in the inner magnetosphere. *Journal of Geophysical Research: Space Physics*, 114(A1), 2009. doi: 10.1029/2008JA013614.

Joel A Fedder, Steve P Slinker, John G Lyon, and RD Elphinstone. Global numerical simulation of the growth phase and the expansion onset for a substorm observed by viking. *Journal of Geophysical Research: Space Physics*, 100(A10):19083–19093, 1995. doi: 10.1029/95JA01524.

Alex C Fletcher, Chris Crabtree, Gurudas Ganguli, David Malaspina, Erik Tejero, and Xiangning Chu. Kinetic equilibrium and stability analysis of dipolarization fronts. *Journal of Geophysical Research: Space Physics*, 2019. doi: 10.1029/2018JA026433.

JC Foster and WJ Burke. Saps: A new categorization for sub-auroral electric fields. *Eos, Transactions American Geophysical Union*, 83(36):393–394, 2002. doi: 10.1029/2002EO000289.

JC Foster and W Rideout. Midlatitude tec enhancements during the october 2003 superstorm. *Geophysical research letters*, 32(12), 2005. doi: 10.1029/2004GL021719.

JC Foster and HB Vo. Average characteristics and activity dependence of the subauroral

polarization stream. *Journal of Geophysical Research: Space Physics*, 107(A12):SIA–16, 2002. doi: 10.1029/2002JA009409.

JC Foster, PJ Erickson, AJ Coster, J Goldstein, and FJ Rich. Ionospheric signatures of plasmaspheric tails. *Geophysical Research Letters*, 29(13):1–1, 2002. doi: 10.1029/2002GL015067.

JC Foster, W Rideout, B Sandel, WT Forrester, and FJ Rich. On the relationship of saps to storm-enhanced density. *Journal of Atmospheric and Solar-Terrestrial Physics*, 69(3): 303–313, 2007. doi: 10.1016/j.jastp.2006.07.021.

JC Foster, PJ Erickson, AJ Coster, S Thaller, J Tao, JR Wygant, and JW Bonnell. Storm time observations of plasmasphere erosion flux in the magnetosphere and ionosphere. *Geophysical Research Letters*, 41(3):762–768, 2014. doi: 10.1002/2013GL059124.

HS Fu, YV Khotyaintsev, A Vaivads, M André, VA Sergeev, SY Huang, EA Kronberg, and PW Daly. Pitch angle distribution of suprathermal electrons behind dipolarization fronts: A statistical overview. *J. Geophys. Res.: Space Physics*, 117(A12), 2012a. doi: 10.1029/2012JA018141.

Huishan S Fu, Yuri V Khotyaintsev, Mats André, and Andris Vaivads. Fermi and betatron acceleration of suprathermal electrons behind dipolarization fronts. *Geophys. Res. Lett.*, 38(16), 2011. doi: 10.1029/2011GL048528.

Huishan S Fu, Yuri V Khotyaintsev, Andris Vaivads, Mats André, and SY Huang. Electric structure of dipolarization front at sub-proton scale. *Geophys. Res. Lett.*, 39(6), 2012b. doi: 10.1029/2012GL051274.

Bea Gallardo-Lacourt, Y Nishimura, LR Lyons, EV Mishin, JM Ruohoniemi, EF Donovan, V Angelopoulos, and N Nishitani. Influence of auroral streamers on rapid evolution of

ionospheric saps flows. *Journal of Geophysical Research: Space Physics*, 122(12), 2017. doi: 10.1002/2017JA024198.

Yu I Galperin, Vladimir Nikolaevich Ponomarev, and AG Zosimova. Plasma convection in polar ionosphere. Technical report, Institut Kosmicheskikh Issledovanii, Moscow, 1974.

G Ganguli, YC Lee, and PJ Palmadesso. Electron–ion hybrid mode due to transverse velocity shear. *Phys. Fluids*, 31(10):2753–2756, 1988a. doi: 10.1063/1.866982.

G Ganguli, YC Lee, and PJ Palmadesso. Kinetic theory for electrostatic waves due to transverse velocity shears. *Phys. Fluids*, 31(4):823–838, 1988b. doi: 10.1063/1.866818.

G Ganguli, MJ Keskinen, H Romero, R Heelis, T Moore, and C Pollock. Coupling of microprocesses and macroprocesses due to velocity shear: An application to the low-altitude ionosphere. *J. Geophys. Res.: Space Physics*, 99(A5):8873–8889, 1994a. doi: 10.1029/93JA03181.

G Ganguli, H Romero, and J Fedder. Interaction between global mhd and kinetic processes in the magnetotail. *Washington DC American Geophysical Union Geophysical Monograph Series*, 84:135–148, 1994b. doi: 10.1029/GM084p0135.

G Ganguli, E Tejero, C Crabtree, W Amatucci, and L Rudakov. Generation of electromagnetic waves in the very low frequency band by velocity gradient. *Phys. Plasmas*, 21(1): 012107, 2014. doi: 10.1063/1.4862032.

Gurudas Ganguli, Chris Crabtree, Alex C Fletcher, Erik Tejero, David Malaspina, and Ian Cohen. Kinetic equilibrium of dipolarization fronts. *Sci. Rep-UK*, 8(1):17186, 2018. doi: 10.1038/s41598-018-35349-9.

TW Garner, RA Wolf, RW Spiro, WJ Burke, Bela G Fejer, S Sazykin, JL Roeder, and MR Hairston. Magnetospheric electric fields and plasma sheet injection to low l-shells

during the 4–5 june 1991 magnetic storm: Comparison between the rice convection model and observations. *Journal of Geophysical Research: Space Physics*, 109(A2), 2004. doi: 10.1029/2003JA010208.

J Goldstein, JL Burch, and BR Sandel. Magnetospheric model of subauroral polarization stream. *Journal of Geophysical Research: Space Physics*, 110(A9), 2005. doi: 10.1029/2005JA011135.

WD Gonzalez. A unified view of solar wind-magnetosphere coupling functions. *Planetary and Space Science*, 38(5):627–632, 1990. doi: 10.1016/0032-0633(90)90068-2.

H Hasegawa, M Fujimoto, T-D Phan, H Reme, A Balogh, MW Dunlop, C Hashimoto, and R TanDokoro. Transport of solar wind into earth's magnetosphere through rolled-up kelvin–helmholtz vortices. *Nature*, 430(7001):755, 2004.

Fei He, Xiao-Xin Zhang, and Bo Chen. Solar cycle, seasonal, and diurnal variations of subauroral ion drifts: Statistical results. *Journal of Geophysical Research: Space Physics*, 119(6):5076–5086, 2014. doi: 10.1002/2014JA019807.

Fei He, Xiao-Xin Zhang, Wenbin Wang, and Bo Chen. Double-peak subauroral ion drifts (dsaids). *Geophysical Research Letters*, 43(11):5554–5562, 2016. doi: 10.1002/2016GL069133.

Fei He, Xiao-Xin Zhang, Wenbin Wang, and Weixing Wan. Different evolution patterns of subauroral polarization streams (saps) during intense storms and quiet time substorms. *Geophysical Research Letters*, 44(21), 2017. doi: 10.1002/2017GL075449.

Fei He, Xiao-Xin Zhang, Wenbin Wang, Libo Liu, Zhi-Peng Ren, Xinan Yue, Lianhuan Hu, Weixing Wan, and Hui Wang. Large-scale structure of subauroral polarization streams

during the main phase of a severe geomagnetic storm. *Journal of Geophysical Research: Space Physics*, 123(4):2964–2973, 2018. doi: 10.1002/2018JA025234.

YQ Hu, XC Guo, and Chi Wang. On the ionospheric and reconnection potentials of the earth: Results from global mhd simulations. *Journal of Geophysical Research: Space Physics*, 112(A7), 2007. doi: 10.1029/2006JA012145.

Can Huang, Mingyu Wu, Quanming Lu, Rongsheng Wang, and Shui Wang. Electron acceleration in the dipolarization front driven by magnetic reconnection. *Journal of Geophysical Research: Space Physics*, 120(3):1759–1765, 2015. doi: 10.1002/2014JA020918.

Chao-Song Huang and John C Foster. Correlation of the subauroral polarization streams (saps) with the dst index during severe magnetic storms. *Journal of Geophysical Research: Space Physics*, 112(A11), 2007. doi: 10.1029/2007JA012584.

JR Kan and LC Lee. Energy coupling function and solar wind-magnetosphere dynamo. *Geophysical Research Letters*, 6(7):577–580, 1979. doi: 10.1029/GL006i007p00577.

Michael C Kelley. *The Earth's ionosphere: plasma physics and electrodynamics*, volume 96. Academic press, 2009.

Alexandre Koustov, Nozomu Nishitani, Y Ebihara, T Kikuchi, MR Hairston, and D Andre. Subauroral polarization streams: Observations with the hokkaido and king salmon superdarn radars and modeling. 26(11):3317–3327, 2008. doi: 10.5194/angeo-26-3317-2008.

Nicholas A Krall and Paulett C Liewer. Low-frequency instabilities in magnetic pulses. *Physical Review A*, 4(5):2094, 1971. doi: 10.1103/PhysRevA.4.2094.

BSR Kunduri, JBH Baker, JM Ruohoniemi, EG Thomas, SG Shepherd, and KT Sterne. Statistical characterization of the large-scale structure of the subauroral polarization

stream. *Journal of Geophysical Research: Space Physics*, 122(6):6035–6048, 2017. doi: 10.1002/2017JA024131.

Giovanni Lapenta and Lapo Bettarini. Self-consistent seeding of the interchange instability in dipolarization fronts. *Geophys. Res. Lett.*, 38(11), 2011. doi: 10.1029/2011GL047742.

Solène Lejosne, BSR Kunduri, FS Mozer, and DL Turner. Energetic electron injections deep into the inner magnetosphere: A result of the subauroral polarization stream (saps) potential drop. *Geophysical Research Letters*, 45(9):3811–3819, 2018. doi: 10.1029/2018GL077969.

Dong Lin, Chi Wang, Wenya Li, Binbin Tang, Xiaocheng Guo, and Zhong Peng. Properties of kelvin-helmholtz waves at the magnetopause under northward interplanetary magnetic field: Statistical study. *J. Geophys. Res.: Space Physics*, 119(9):7485–7494, 2014. doi: 10.1002/2014JA020379.

CM Liu, HS Fu, Andris Vaivads, Yuri V Khotyaintsev, DJ Gershman, K-J Hwang, ZZ Chen, D Cao, Y Xu, J Yang, et al. Electron jet detected by mms at dipolarization front. *Geophysical Research Letters*, 45(2):556–564, 2018a. doi: 10.1002/2017GL076509.

Han-Li Liu, Charles G Bardeen, Benjamin T Foster, Peter Lauritzen, Jing Liu, Gang Lu, Daniel R Marsh, Astrid Maute, Joseph M McInerney, Nicholas M Pedatella, et al. Development and validation of the whole atmosphere community climate model with thermosphere and ionosphere extension (waccm-x 2.0). *Journal of Advances in Modeling Earth Systems*, 10(2):381–402, 2018b. doi: 10.1002/2017MS001232.

J Liu, V Angelopoulos, A Runov, and X-Z Zhou. On the current sheets surrounding dipolarizing flux bundles in the magnetotail: The case for wedgelets. *J. Geophys. Res.: Space Physics*, 118(5):2000–2020, 2013. doi: 10.1002/jgra.50092.

Yu Liu, Jinxiang Cao, Liang Xu, Xiao Zhang, Pi Wang, Jian Wang, Yinchang Du, and Zhe Zheng. Coherent structure generated in the boundary layer of a laboratory-created ionospheric depletion. *Geophys. Res. Lett.*, 41(5):1413–1419, 2014. doi: 10.1002/2014GL059211.

Yu Liu, Jiuhou Lei, Pengcheng Yu, Zhongkai Zhang, Xiao Zhang, and Jinxiang Cao. Laboratory generation of broadband elf waves by inhomogeneous plasma flow. *Geophys. Res. Lett.*, 44(4):1634–1640, 2017. doi: 10.1002/2016GL072232.

RE Lopez, M Wiltberger, S Hernandez, and JG Lyon. Solar wind density control of energy transfer to the magnetosphere. *Geophysical Research Letters*, 31(8), 2004. doi: 10.1029/2003GL018780.

RE Lopez, R Bruntz, EJ Mitchell, M Wiltberger, JG Lyon, and VG Merkin. Role of magnetosheath force balance in regulating the dayside reconnection potential. *Journal of Geophysical Research: Space Physics*, 115(A12), 2010. doi: 10.1029/2009JA014597.

San Lu, Quanming Lu, Yu Lin, Xueyi Wang, Yasong Ge, Rongsheng Wang, Meng Zhou, Huishan Fu, Can Huang, Mingyu Wu, et al. Dipolarization fronts as earthward propagating flux ropes: A three-dimensional global hybrid simulation. *J. Geophys. Res.: Space Physics*, 120(8):6286–6300, 2015. doi: 10.1002/2015JA021213.

San Lu, V Angelopoulos, and Huishan Fu. Suprathermal particle energization in dipolarization fronts: Particle-in-cell simulations. *Journal of Geophysical Research: Space Physics*, 121(10):9483–9500, 2016a. doi: 10.1002/2016JA022815.

San Lu, AV Artemyev, V Angelopoulos, Quanming Lu, and Jiang Liu. On the current density reduction ahead of dipolarization fronts. *J. Geophys. Res.: Space Physics*, 121(5):4269–4278, 2016b. doi: 10.1002/2016JA022754.

JG Lyon, JA Fedder, and CM Mobarry. The lyon–fedder–mobarry (lfm) global mhd magnetospheric simulation code. *Journal of Atmospheric and Solar-Terrestrial Physics*, 66 (15-16):1333–1350, 2004a. doi: 10.1016/j.jastp.2004.03.020.

JG Lyon, JA Fedder, and CM Mobarry. The lyon–fedder–mobarry (lfm) global mhd magnetospheric simulation code. *Journal of Atmospheric and Solar-Terrestrial Physics*, 66 (15-16):1333–1350, 2004b. doi: 10.1016/j.jastp.2004.03.020.

LR Lyons, Y Nishimura, B Gallardo-Lacourt, MJ Nicolls, S Chen, DL Hampton, WA Bristow, JM Ruohoniemi, N Nishitani, EF Donovan, et al. Azimuthal flow bursts in the inner plasma sheet and possible connection with saps and plasma sheet earthward flow bursts. *Journal of Geophysical Research: Space Physics*, 120(6):5009–5021, 2015. doi: 10.1002/2015JA021023.

RA Makarevich and PL Dyson. Dual hf radar study of the subauroral polarization stream. In *Annales Geophysicae*, volume 25, pages 2579–2591, 2008.

VG Merkin and JG Lyon. Effects of the low-latitude ionospheric boundary condition on the global magnetosphere. *Journal of Geophysical Research: Space Physics*, 115(A10), 2010a. doi: 10.1029/2010JA015461.

VG Merkin and JG Lyon. Effects of the low-latitude ionospheric boundary condition on the global magnetosphere. *Journal of Geophysical Research: Space Physics*, 115(A10), 2010b. doi: 10.1029/2010JA015461.

Evgeny Mishin, Yukitoshi Nishimura, and John Foster. Saps/said revisited: A causal relation to the substorm current wedge. *Journal of Geophysical Research: Space Physics*, 122(8): 8516–8535, 2017. doi: 10.1002/2017JA024263.

Space Studies Board National Research Council. *Solar and space physics: A science for a technological society*. National Academies Press, 2013.

PT Newell, T Sotirelis, K Liou, C-I Meng, and FJ Rich. A nearly universal solar wind-magnetosphere coupling function inferred from 10 magnetospheric state variables. *Journal of Geophysical Research: Space Physics*, 112(A1), 2007. doi: 10.1029/2006JA012015.

PT Newell, T Sotirelis, and S Wing. Diffuse, monoenergetic, and broadband aurora: The global precipitation budget. *Journal of Geophysical Research: Space Physics*, 114(A9), 2009. doi: 10.1029/2009JA014326.

M Palmroth, TI Pulkkinen, P Janhunen, DJ McComas, CW Smith, and HEJ Koskinen. Role of solar wind dynamic pressure in driving ionospheric joule heating. *Journal of Geophysical Research: Space Physics*, 109(A11), 2004. doi: 10.1029/2004JA010529.

Asher Pembroke, Frank Toffoletto, Stanislav Sazykin, Michael Wiltberger, John Lyon, Viacheslav Merkin, and Peter Schmitt. Initial results from a dynamic coupled magnetosphere-ionosphere-ring current model. *Journal of Geophysical Research: Space Physics*, 117(A2), 2012. doi: 10.1029/2011JA016979.

Kenneth G Powell, Philip L Roe, Timur J Linde, Tamas I Gombosi, and Darren L De Zeeuw. A solution-adaptive upwind scheme for ideal magnetohydrodynamics. *Journal of Computational Physics*, 154(2):284–309, 1999. doi: 10.1006/jcph.1999.6299.

PL Pritchett and FV Coroniti. A kinetic ballooning/interchange instability in the magnetotail. *J. Geophys. Res.: Space Physics*, 115(A6), 2010. doi: 10.1029/2009JA014752.

TI Pulkkinen, M Palmroth, EI Tanskanen, N Yu Ganushkina, MA Shukhtina, and NP Dmitrieva. Solar wind—magnetosphere coupling: a review of recent results. *Journal*

of Atmospheric and Solar-Terrestrial Physics, 69(3):256–264, 2007. doi: 10.1016/j.jastp.2006.05.029.

J Raeder, J Berchem, and M Ashour-Abdalla. The geospace environment modeling grand challenge: Results from a global geospace circulation model. *Journal of Geophysical Research: Space Physics*, 103(A7):14787–14797, 1998. doi: 10.1029/98JA00014.

Joachim Raeder, William D Cramer, Joseph Jensen, Timothy Fuller-Rowell, Naomi Maruyama, Frank Toffoletto, and Hien Vo. Sub-auroral polarization streams: A complex interaction between the magnetosphere, ionosphere, and thermosphere. In *Journal of Physics: Conference Series*, volume 767, page 012021. IOP Publishing, 2016. doi: 10.1088/1742-6596/767/1/012021.

Geoffrey D Reeves, Y Chen, GS Cunningham, RWH Friedel, Michael G Henderson, VK Jordanova, J Koller, SK Morley, MF Thomsen, and S Zaharia. Dynamic radiation environment assimilation model: Dream. *Space Weather*, 10(3):1–25, 2012. doi: 10.1029/2011SW000729.

Patricia H Reiff, Robert W Spiro, and TW Hill. Dependence of polar cap potential drop on interplanetary parameters. *Journal of Geophysical Research: Space Physics*, 86(A9): 7639–7648, 1981. doi: 10.1029/JA086iA09p07639.

AD Richmond, EC Ridley, and RG Roble. A thermosphere/ionosphere general circulation model with coupled electrodynamics. *Geophysical Research Letters*, 19(6):601–604, 1992. doi: 10.1029/92GL00401.

RG Roble, E Co Ridley, AD Richmond, and RE Dickinson. A coupled thermosphere/ionosphere general circulation model. *Geophysical Research Letters*, 15(12):1325–1328, 1988. doi: 10.1029/GL015i012p01325.

H Romero and G Ganguli. Nonlinear evolution of a strongly sheared cross-field plasma flow. *Phys. Fluids B: Plasma Phys.*, 5(9):3163–3181, 1993. doi: 10.1063/1.860653.

H Romero, G Ganguli, YC Lee, and PJ Palmadesso. Electron–ion hybrid instabilities driven by velocity shear in a magnetized plasma. *Phys. Fluids B: Plasma Phys.*, 4(7):1708–1723, 1992. doi: 10.1063/1.860028.

A Runov, V Angelopoulos, MI Sitnov, VA Sergeev, J Bonnell, JP McFadden, D Larson, K-H Glassmeier, and U Auster. Themis observations of an earthward-propagating dipolarization front. *Geophys. Res. Lett.*, 36(14), 2009. doi: 10.1029/2009GL038980.

A Runov, V Angelopoulos, X-Z Zhou, X-J Zhang, S Li, F Plaschke, and J Bonnell. A themis multicase study of dipolarization fronts in the magnetotail plasma sheet. *J. Geophys. Res.: Space Physics*, 116(A5), 2011. doi: 10.1029/2010JA016316.

WA Scales, PA Bernhardt, G Ganguli, CL Siefring, and P Rodriguez. Small-scale plasma irregularities produced during electron attachment chemical releases. *Geophys. Res. Lett.*, 21(7):605–608, 1994a. doi: 10.1029/94GL00369.

Wayne A Scales, PA Bernhardt, and Gurudas Ganguli. Early time evolution of negative ion clouds and electron density depletions produced during electron attachment chemical release experiments. *J. Geophys. Res.: Space Physics*, 99(A1):373–381, 1994b. doi: 10.1029/93JA02752.

Daniel Schmid, Martin Volwerk, R Nakamura, W Baumjohann, and Martin Heyn. A statistical and event study of magnetotail dipolarization fronts. *Ann. Geophys.*, 29(9):1537–1547, 2011. doi: 10.5194/angeo-29-1537-2011.

SG Shepherd, RA Greenwald, and JM Ruohoniemi. Cross polar cap potentials measured with super dual auroral radar network during quasi-steady solar wind and interplanetary

magnetic field conditions. *Journal of Geophysical Research: Space Physics*, 107(A7), 2002. doi: 10.1029/2001JA000152.

Xueling Shi, Tao Chen, Lingqian Zhang, Suping Duan, Jiang Liu, and Zhaohai He. Ion flux dropout observed near dipolarization front. *Chinese Sci. Bull.*, 59(34):4790–4796, 2014. doi: 10.1007/s11434-014-0616-8.

Atsuki Shinbori, Yuichi Otsuka, Takuya Tsugawa, Michi Nishioka, Atsushi Kumamoto, Fuminori Tsuchiya, Shoya Matsuda, Yoshiya Kasahara, Ayako Matsuoka, J Michael Ruohoniemi, et al. Temporal and spatial variations of storm time midlatitude ionospheric trough based on global gnss-tec and arase satellite observations. *Geophysical Research Letters*, 45(15):7362–7370, 2018. doi: 10.1029/2018GL078723.

GL Siscoe, NU Crooker, and KD Siebert. Transpolar potential saturation: Roles of region 1 current system and solar wind ram pressure. *Journal of Geophysical Research: Space Physics*, 107(A10), 2002. doi: 10.1029/2001JA009176.

MI Sitnov, M Swisdak, and AV Divin. Dipolarization fronts as a signature of transient reconnection in the magnetotail. *J. Geophys. Res.: Space Physics*, 114(A4), 2009. doi: 10.1029/2008JA013980.

Kareem A Sorathia, Aleksandr Y Ukhorskiy, Viacheslav G Merkin, Joseph F Fennell, and Seth G Claudepierre. Modeling the depletion and recovery of the outer radiation belt during a geomagnetic storm: Combined mhd and test particle simulations. *Journal of Geophysical Research: Space Physics*, 123(7):5590–5609, 2018. doi: 10.1029/2018JA025506.

RW Spiro, RA Heelis, and WB Hanson. Rapid subauroral ion drifts observed by atmosphere explorer c. *Geophysical Research Letters*, 6(8):657–660, 1979. doi: 10.1029/GL006i008p00657.

DA Subbotin and YY Shprits. Three-dimensional modeling of the radiation belts using the versatile electron radiation belt (verb) code. *Space Weather*, 7(10), 2009. doi: 10.1029/2008SW000452.

KÅT Sundberg, JA Cumnock, and Lars G Blomberg. Reverse convection potential: A statistical study of the general properties of lobe reconnection and saturation effects during northward imf. *Journal of Geophysical Research: Space Physics*, 114(A6), 2009. doi: 10.1029/2008JA013838.

Frank Toffoletto, Stanislav Sazykin, Robert Spiro, and Richard Wolf. Inner magnetospheric modeling with the rice convection model. *Space Science Reviews*, 107(1-2):175–196, 2003. doi: 10.1023/A:1025532008047.

Gábor Tóth, Igor V Sokolov, Tamas I Gombosi, David R Chesney, C Robert Clauer, Darren L De Zeeuw, Kenneth C Hansen, Kevin J Kane, Ward B Manchester, Robert C Oehmke, et al. Space weather modeling framework: A new tool for the space science community. *Journal of Geophysical Research: Space Physics*, 110(A12), 2005. doi: 10.1029/2005JA011126.

NA Tsyganenko and MI Sitnov. Magnetospheric configurations from a high-resolution data-based magnetic field model. *Journal of Geophysical Research: Space Physics*, 112(A6), 2007. doi: 10.1029/2007JA012260.

Weichao Tu, GS Cunningham, Y Chen, MG Henderson, E Camporeale, and GD Reeves. Modeling radiation belt electron dynamics during gem challenge intervals with the dream3d diffusion model. *Journal of Geophysical Research: Space Physics*, 118(10): 6197–6211, 2013. doi: 10.1002/jgra.50560.

RH Varney, Michael Wiltberger, and W Lotko. Modeling the interaction between convection

and nonthermal ion outflows. *Journal of Geophysical Research: Space Physics*, 120(3): 2353–2362, 2015. doi: 10.1002/2014JA020769.

W Wang, M Wiltberger, AG Burns, SC Solomon, TL Killeen, N Maruyama, and JG Lyon. Initial results from the coupled magnetosphere–ionosphere–thermosphere model: thermosphere–ionosphere responses. *Journal of atmospheric and solar-terrestrial physics*, 66(15-16):1425–1441, 2004. doi: 10.1016/j.jastp.2004.04.008.

Wenbin Wang, Elsayed R Talaat, Alan G Burns, Barbary Emery, Syau-yun Hsieh, Jiuhou Lei, and Jiyao Xu. Thermosphere and ionosphere response to subauroral polarization streams (saps): Model simulations. *Journal of Geophysical Research: Space Physics*, 117 (A7), 2012. doi: 10.1029/2012JA017656.

FD Wilder, CR Clauer, and JBH Baker. Reverse convection potential saturation during northward imf. *Geophysical Research Letters*, 35(12), 2008. doi: 10.1029/2008GL034040.

M Wiltberger, W Wang, AG Burns, SC Solomon, JG Lyon, and CC Goodrich. Initial results from the coupled magnetosphere ionosphere thermosphere model: Magnetospheric and ionospheric responses. *Journal of atmospheric and solar-terrestrial physics*, 66(15-16): 1411–1423, 2004. doi: 10.1016/j.jastp.2004.03.026.

M Wiltberger, V Merkin, B Zhang, F Toffoletto, M Oppenheim, W Wang, JG Lyon, J Liu, Y Dimant, MI Sitnov, et al. Effects of electrojet turbulence on a magnetosphere-ionosphere simulation of a geomagnetic storm. *Journal of Geophysical Research: Space Physics*, 122 (5):5008–5027, 2017. doi: 10.1002/2016JA023700.

Michael Wiltberger, RS Weigel, W Lotko, and JA Fedder. Modeling seasonal variations of auroral particle precipitation in a global-scale magnetosphere-ionosphere simulation. *Journal of Geophysical Research: Space Physics*, 114(A1), 2009. doi: 10.1029/2008JA013108.

CC Wu, RJ Walker, and JM Dawson. A three dimensional mhd model of the earth?s magnetosphere. *Geophysical Research Letters*, 8(5):523–526, 1981. doi: 10.1029/GL008i005p00523.

H-C Yeh, JC Foster, FJ Rich, and W Swider. Storm time electric field penetration observed at mid-latitude. *Journal of Geophysical Research: Space Physics*, 96(A4):5707–5721, 1991. doi: 10.1029/90JA02751.

Yiqun Yu, Vania Jordanova, Shasha Zou, Roderick Heelis, Mike Ruohoniemi, and John Wygant. Modeling subauroral polarization streams during the 17 march 2013 storm. *Journal of Geophysical Research: Space Physics*, 120(3):1738–1750, 2015. doi: 10.1002/2014JA020371.

Zhigang Yuan, Ying Xiong, Zheng Qiao, Haimeng Li, Shiyong Huang, Dedong Wang, Xiaohua Deng, Tero Raita, and Jingfang Wang. A subauroral polarization stream driven by field-aligned currents associated with precipitating energetic ions caused by emic waves: A case study. *Journal of Geophysical Research: Space Physics*, 121(2):1696–1705, 2016. doi: 10.1002/2015JA021804.

Zhigang Yuan, Zheng Qiao, Haimeng Li, Shiyong Huang, Dedong Wang, Xiongdong Yu, and Tao Yu. Subauroral polarization stream on the outer boundary of the ring current during an energetic ion injection event. *Journal of Geophysical Research: Space Physics*, 122(4):4837–4845, 2017. doi: 10.1002/2016JA023570.

B Zhang, W Lotko, MJ Wiltberger, OJ Brambles, and PA Damiano. A statistical study of magnetosphere–ionosphere coupling in the lyon–fedder–mobarry global mhd model. *Journal of Atmospheric and Solar-Terrestrial Physics*, 73(5-6):686–702, 2011. doi: 10.1016/j.jastp.2010.09.027.

B Zhang, W Lotko, O Brambles, Michael Wiltberger, and J Lyon. Electron precipitation models in global magnetosphere simulations. *Journal of Geophysical Research: Space Physics*, 120(2):1035–1056, 2015. doi: 10.1002/2014JA020615.

B Zhang, OJ Brambles, PA Cassak, JE Ouellette, M Wiltberger, W Lotko, and JG Lyon. Transition from global to local control of dayside reconnection from ionospheric-sourced mass loading. *Journal of Geophysical Research: Space Physics*, Accepted, 2017a. doi: 10.1002/2016JA023646.

Shun-Rong Zhang, Philip J Erickson, Yongliang Zhang, Wenbin Wang, Chaosong Huang, Anthea J Coster, John M Holt, John F Foster, Michael Sulzer, and Robert Kerr. Observations of ion-neutral coupling associated with strong electrodynamic disturbances during the 2015 st. patrick's day storm. *Journal of Geophysical Research: Space Physics*, 122(1): 1314–1337, 2017b. doi: 10.1002/2016JA023307.

Xu Zhang, V Angelopoulos, AV Artemyev, and Jiang Liu. Whistler and electron firehose instability control of electron distributions in and around dipolarizing flux bundles. *Geophys. Res. Lett.*, 45(18):9380–9389, 2018. doi: 10.1029/2018GL079613.

Yihua Zheng, Pontus C Brandt, Anthony TY Lui, and Mei-Ching Fok. On ionospheric trough conductance and subauroral polarization streams: Simulation results. *Journal of Geophysical Research: Space Physics*, 113(A4), 2008. doi: 10.1029/2007JA012532.

Meng Zhou, Maha Ashour-Abdalla, Xiaohua Deng, David Schriver, Mostafa El-Alaoui, and Ye Pang. Themis observation of multiple dipolarization fronts and associated wave characteristics in the near-earth magnetotail. *Geophys. Res. Lett.*, 36(20), 2009. doi: 10.1029/2009GL040663.